Dissecting amygdala cell-types in fear and extinction

Inauguraldissertation

zur
Erlangung der Würde eines Doktors der Philosophie
vorgelegt der
Philosophisch-Naturwissenschaftlichen Fakultät
der Universität Basel
von

Kenta M. Hagihara

aus Nanporo, Sorachi, Hokkaido, Japan

Basel, 2023

Genehmigt von der Philosophisch-Naturwissenschaftlichen Fakultät auf Antrag von:

Prof. Dr. Andreas Lüthi
(Fakultätsverantwortlicher und Dissertationsleiter)

Prof. Dr. Thomas D. Mrsic-Flogel
(Korreferent)

Basel, 22. Juni 2021

Prof. Dr. Marcel Mayor
(Dekan)

TABLE OF CONTENTS

1. Abstract

The mammalian brain consists of billions of neurons; Individual neurons serve as building blocks (Cajal 1911, translation Swanson and Swanson 1995). However, studying individual neurons is simply insufficient to understand how the brain works. A promising approach is the cell-type-specific approach, an effort to classify neurons that perform the same function as a single cell type (functional definition, see (Luo et al., 2008)) and to understand their roles in information processing and behavioral outputs. Nevertheless, the limitation of this definition is that we barely know the precise functions or roles of neurons, and even in very well-characterized neurons such as retinal ganglion cells, there would likely be remaining unknown functions. Thus, as an operational definition to drive neuroscience forward, defining cell types using genetic tools that allow us to access specific subsets of neurons was suggested and widely accepted in an almost implicit manner. This consensus is based on an optimistic view that, at some point, the operational genetic definition and the ultimate functional definition would converge.

In this thesis, having this philosophy in mind, I try to match several operationally defined amygdala cell types with their distinct functions/roles in the context of fear and extinction learning. In **Project 1**, I demonstrate that a cell-type in the amygdala complex defined by molecular marker expression exerts essential functions in fear and extinction by composing a unique mutual inhibition circuit motif. In **Project 2**, I find that a cell-type in the basolateral amygdala defined by di-synaptic downstream target show unprecedented functional specificity in fear learning. Finally, in **Project 3**, I aim to characterize functions and roles of cell types in the basolateral amygdala defined by dynamic, neuronal activity-dependent gene expression upon learning.

Collectively, this thesis serves as an important stepping stone to achieving the convergence between definitions of a cell type.

2. Introduction

2.1. Learning and memory – underlying neuronal mechanisms

The phrase "cogito ergo sum" written by the French philosopher René Descartes in 1637, is probably one of the most widely quoted statements in Western philosophy. Nevertheless, based on modern neurobiology since the 20th century, this statement is absolutely wrong for the following two reasons. The first reason is that Descartes envisioned mental activity as entirely independent of physical activity. However, we biologists are convinced that all activities of the mind originate in the brain. Antonio Damasio, in his book "Descartes' Error", argues, and I personally agree with, that it would be more accurate to rephrase it as "I am, therefore I think". Secondly, and more importantly, we are not us simply because we think, but we are us because we remember what we have experienced and have thought in the past. In other words, our self-consciousness and our connections with others are all dependent on our memory – the brain's ability to record and store experiences.

In this sense, learning and memory is one of the most fundamental functions of the brain for our life. It has been developed through evolution to better adapt to the ever-changing world and is widely conserved across phylogeny, including animals with no central nervous system and even monocellular organisms. However, the more complex and larger the system gets, the more sophisticated learning and memory was in general achieved and it supports our highly cognitive functions. Thus, understanding neuronal mechanisms underlying learning and memory eventually leads to better understand human intelligence and serves as one of the ultimate goals of current neuroscience.

2.1.1. Neuronal plasticity at synapses

To achieve learning and memory, the brain has to generate different outputs in response even to exactly the same inputs in a context-, state-, and prior experience-dependent manner. The most prominent underlying mechanism for this dynamic adaptive process would be synaptic plasticity between neurons. Indeed, seminal work carried out by Eric Kandel and colleagues demonstrated that changes in the strength of single synapses directly serve as substrates for short term, as well as long term memory storage (Kandel, 2001). Furthermore, subsequent decades of research have identified several promising plasticity rules such as STDP (spike timing dependent plasticity, (Bi and Poo, 1998)), as well as mechanistic molecular level underpinnings for both pre-synaptic and post-synaptic mechanisms (Citri and Malenka, 2008; Malinow and Malenka, 2002). One hallmark study was performed by Malinow and colleagues in 2005 (Rumpel et al., 2005), where the authors demonstrated that NMDA-dependent AMPA receptor trafficking to the post-synaptic membrane of synapses is the core mechanism for enhanced CS responses after fear conditioning (see **2.2**), and thus, underly fear memory.

2.1.2. From cellular physiology to circuit-level neuroscience

Although above-mentioned work might give an impression of "fear conditioning explained", the actual living brain (at least mammalian brain) is more enigmatic and elusive. Inspired by theoretical frameworks such as Hebb's assembly scheme (Hebb, 1949; Morris, 1999) and Hopfield network (Hopfield, 1982), how neuronal population could store information for subsequent readout has been extensively discussed both theoretically and experimentally. With this concept in mind, the last 2-3 decades have witnessed eye-opening methodological progress in large-scale simultaneous measurement of neuronal activity in vivo ((Jun et al., 2017; Sofroniew et al., 2016) also see **2.4.2**) and resultant description of rich neuronal

population dynamics (Steinmetz et al., 2019; Stringer et al., 2021). One noteworthy finding was provided by Schnitzer and colleagues in 2017 (Grewe et al., 2017), where the authors performed a large-scale calcium imaging from the basolateral amygdala (see **2.3.2**) in animals engaged in fear conditioning and found that enhanced CS responses are not the only plasticity occurring in parallel with fear learning. Instead, they found diverse changes in the activity of individual neurons, including decreased CS responses through learning, and concluded that the underlying mechanism might be implemented rather at the population level; Representation of CS gradually gets closer to that of US.

To deepen the understanding of memory mechanisms, it is thus extremely important to connect different scales. One promising concept would be the circuit-level approach, which essentially connects cellular-/molecular-level mechanisms to neuronal population-level dynamics. All the three projects carried out in this thesis are based on this circuit neuroscience philosophy, focusing on the neuronal population as a target while keeping them tractable via a cell-type-specific approach.

2.2. Classical fear conditioning and extinction as a model for associative learning

To study circuit- and cellular-level mechanisms underlying learning and memory, rodents, in particular laboratory mice serve as a powerful model organism. They are genetically homogenized and highly genetically tractable, allowing to target specific genes or cell types for manipulations and to study its effect on their behavior. One additional essential tool here is the behavioral paradigm to assess learning and memory in those model animals. In this section, I will summarize the auditory fear conditioning and extinction paradigm, which I use for all of my projects.

Fear conditioning is a widely used behavioral paradigm as a model of association learning, mainly for the following reasons: 1) Rodents robustly and rapidly learn the paradigm; 2) Foamed memory lasts long; 3) Behavioral output of memory expression is easy to quantify. Fear conditioning can be largely divided into two main variations. One is contextual fear conditioning, in which animals experience an aversive stimulus (unconditioned stimulus, US) – often a foot shock – in a novel context without explicit sensory cues. Subsequently, when animals revisit the context, animals recall fearful experience and exhibit conditioned fear responses (CR). In rodents, CRs are typically freezing behavior, changes in autonomic nervous system activity, stress hormone release, analgesia, secession of reward-seeking behavior, and facilitation of reflexes, and often the fraction of freezing time (freezing score) is used as a quantitative readout of fear memory strength (Davis, 1992; LeDoux, 2000). As this variation requires animals to recognize different contexts, it identified several brain regions that support spatial recognition, such as the hippocampus (Kim and Fanselow, 1992; Phillips and LeDoux, 1992). The alternative variation is cued fear conditioning, in which animals associate discrete initially neutral sensory cues (conditioned stimuli) – often an auditory stimulus for rodents – with an aversive stimulus. After the conditioning, those initially neutral tones are associated with an aversive property of the US and thus, playing the tone alone can elicit CRs. In the present thesis work, I used this auditory fear conditioning in all the projects.

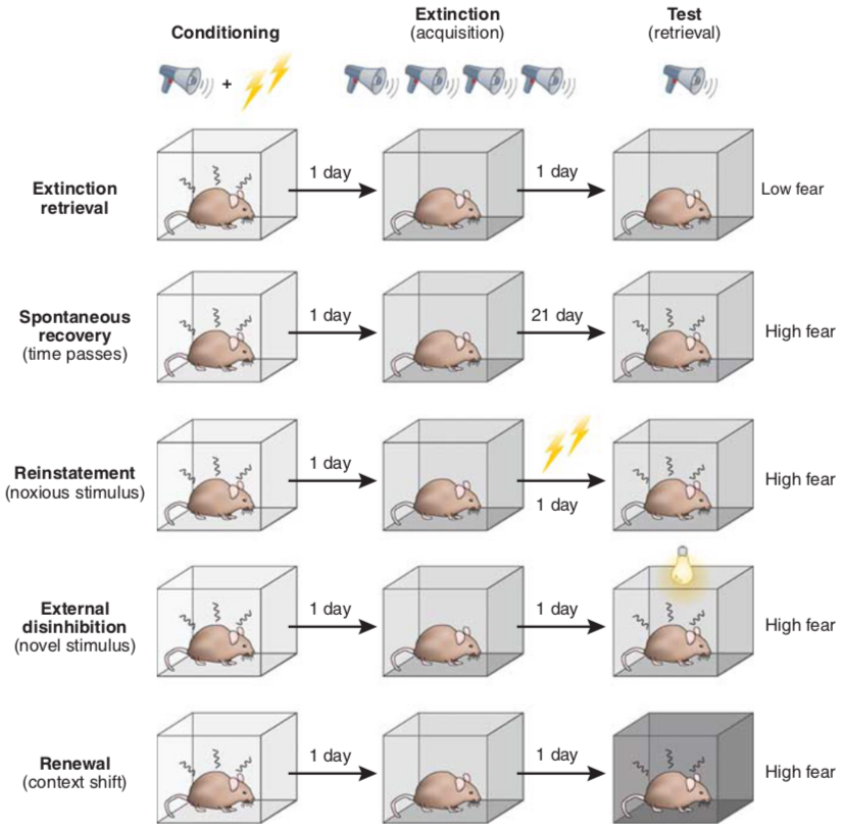

Fig. 1 | **Relapse of original fear memory after extinction.**
After the extinction of a conditioned fear response, extinction, the expression of conditioned fear is reduced. However, a number of phenomena are associated with the return or relapse of fear responses after extinction. These include spontaneous recovery with the passage of time, external disinhibition after the presentation of a novel stimulus, reinstatement after experiencing a noxious event, including the unconditioned stimulus, and renewal after experiencing the conditioned stimulus outside the extinction context. Adopted from (Maren and Holmes, 2016).

After fear conditioning, when the CS is repeatedly presented in the absence of the US, CR gradually decreases, a process known as fear extinction (Pavlov, 1927). A key feature of fear extinction is that it is not simply an erasure of the original fear memory but rather a new learning of CS and non-US association (Myers and Davis, 2007) (but see (Clem and Schiller, 2016) for potential erasure-based mechanisms) that competes with the original fear memory (Bouton, 1993). As a result, extinction is, in general, less durable than conditioning. For example, CRs to an extinguished CS could return with the mere passage of time (spontaneous recovery, **Fig. 1**), an aversive stimulus (reinstatement), a novel stimulus (external inhibition), and a different context (renewal). In addition, when once extinguished animals are submitted to another fear conditioning, they acquire new association more quickly than the first time (ref), again supporting that the original memory is not erased by extinction.

Since fear extinction in the laboratory setting is structurally equivalent to clinical exposure therapy for trauma- and stress-related disorders, including post-traumatic stress disorder (PTSD), understanding the underlying mechanism is not only valuable to understand learning and memory mechanisms in health but also important for developing novel therapeutic interventions (Craske et al., 2017; Maren and Holmes, 2016; Milad and Quirk, 2012; Shalev et al., 2017). Along this direction, a recent study (Baek et al., 2019) shed light on the mechanism of a therapeutic regimen called EMDR (eye-movement desensitization and reprocessing), whose effect was empirically accepted widely yet the mechanism had been somewhat enigmatic (Holmes, 2019).

2.3. Neuronal circuitry underlying fear conditioning and extinction

These days, it has become a widely accepted view that neuronal computations are in general performed in a stand-alone-complex manner, where discrete components behave individually, but they somehow work in concert as a whole. The one underlying fear memory and its extinction is not an exception and thought to be carried by distributed and interconnected brain areas (Herry and Johansen, 2014; Tovote et al., 2015) (**Fig. 2a**). However, classical work identified the amygdala as a central brain structure in fear and extinction, and this still holds true; It serves as a critical central node in the distributed circuits. In this section, I will first summarize how the amygdala initially got attention, then brief subnuclei constituting the amygdala and other a few brain areas known to work in orchestration with the amygdala in fear and extinction.

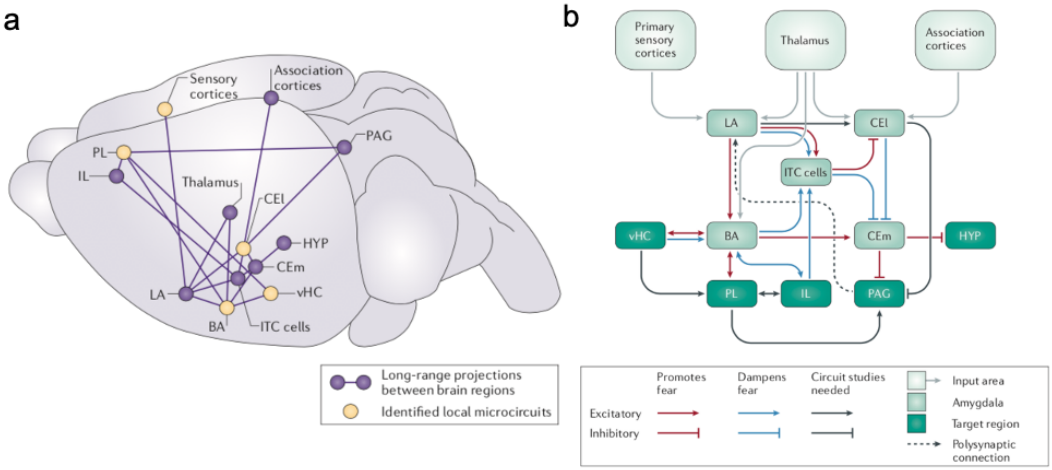

Fig. 2 | **Distributed and interconnected brain areas underlying fear and extinction.**

a. Fear states are mediated by long-range excitatory and inhibitory connections between multiple brain areas. **b.** Several amygdala nuclei receive sensory input from cortical and thalamic centers and are major sites of fear-related neuronal plasticity. In turn, central nuclei of the amygdala project to hypothalamic and brainstem centers to promote fear behavior. Extinction of fear is mediated by different circuit elements within the same structures. Adopted and modified from (Tovote et al., 2015).

2.3.1. The amygdala

The amygdala was discovered as a vital structure for fear emotion by early observations of the effects of brain damage in animals. Brown & Schäfer firstly described profound alterations in emotional reactivity following temporal lobe damage in monkeys (Brown and Schafer, 1888). Klüver & Bucy further characterized that monkeys with temporal lobe resections resulted in a condition termed Klüver-Bucy syndrome, most importantly, including loss of fear (Klüver and Bucy, 1937). Similar effects were replicated in several mammalian species with amygdala damage, including rats, cats, rabbits, dogs, and humans (Goddard, 1964), suggesting that roles of the amygdala in fear processing are well-conserved across mammals. Following those earlier observational studies, researchers further established functions of the amygdala in fear by using learning and memory tasks, including fear conditioning (**2.2**). For example, amygdala lesions abolished acquisition and expression of fear memory, as well as innate fear responses (Blanchard and Blanchard, 1972; Kellicutt and Schwartzbaum, 1963).

Cytoarchitecturally speaking, the amygdala can be divided into three structures: 1) cortical-like structure the basolateral amygdala; 2) striatal-like structure the central amygdala; 3) intercalated neurons. As cellular- and circuit-level understanding so far was mainly obtained by rodent research, in the next a few sections, I will summarize subnuclei of the amygdala in

rodents, especially mice, while most of the basic architecture and organizational principle are in common across species.

2.3.2. Basolateral amygdala

The basolateral amygdala (BLA) is a cortical-like structure; About 80% of BLA neurons are glutamatergic projection neurons and the rest are GABAergic interneurons. The BLA is comprised of the lateral (LA) and basal (BA) nuclei, and forms the primary sensory interface of the amygdala (**Fig. 2b**). Lesion studies demonstrated that the BLA itself (Campeau and Davis, 1995a; LeDoux et al., 1990) and either the auditory thalamus or the auditory cortex to the BLA (Campeau and Davis, 1995b; LeDoux, 1986) are essential for fear conditioning to auditory CSs.

An important step to understanding learning and memory mechanisms is to identify the essential substrate for the encoding and storage of fear memories. There is strong evidence that the BLA is a locus for the formation and storage of CS-US associations during fear conditioning. First, stepping forward from above mentioned permanent lesion studies, temporal inactivation methods yielded important information. For example, inactivation of BLA with muscimol, a $GABA_A$ receptor agonist, and intra-BLA infusion of NMDA receptor antagonist, APV, during fear conditioning resulted in abolished fear memory formation, suggesting that neuronal activity in BLA is required for CS-US association (Maren et al., 1996; Wilensky et al., 1999). Electrophysiological recording studies further support a role for the BLA in encoding and storing fear association. In a series of experiments, Quirk and LeDoux found that auditory fear conditioning enhanced spike-firing triggered by tone CSs (Quirk et al., 1995, 1997). Importantly, they also found that this plasticity in the BLA precedes plasticity in the auditory cortex, suggesting that the direct thalamo-amygdala projection, rather than indirect cortico-amygdala projections, mediate plasticity in the BLA (Quirk et al., 1997). Finally, both in vivo (Rogan et al., 1997) and in vitro (McKernan and Shinnick-Gallagher, 1997; Rumpel et al., 2005) experiments confirmed that LTP, including postsynaptic AMPA receptor trafficking, in the BLA underlies CS-US association. Collectively, these works established a strong link between synaptic plasticity in the BLA and fear learning at the behavioral level.

In addition to fear conditioning, the BLA also plays an important role in fear extinction. Inhibition of neuronal activity or disrupting synaptic plasticity in the BLA impairs extinction (Amano et al., 2011; Herry et al., 2008; Sotres-Bayon et al., 2007; Zimmerman and Maren, 2010). Along this line, an electrophysiological recording study carried by Herry and colleagues found that BLA contains a population selectively responsive to fear triggering CSs (Fear neurons) and ones activated only by extinguished CSs (Extinction neurons), and that the balance of activity between those two discrete functional populations parallels with the formation of stable extinction memories (Herry et al., 2008). The authors also demonstrated that Fear neurons and Extinction neurons are preferentially found in prelimbic (PL) and infralimbic (IL) subdivisions of mPFC projecting-BLA populations, respectively (Senn et al., 2014).

These data suggest that fear and extinction are mediated by functionally and anatomically discrete populations in the BLA. Hinted by this link between projection-target and function of the BLA neurons (also see (Stuber et al., 2011; Tye et al., 2013) for CeA and NAc projecting-BLA neurons), several groups set out to better characterize BLA projection neuron populations with a multifaceted approach including transcriptional identity (Kim et al., 2017; Namburi et al., 2015). However, the results are somewhat controversial, and even within a single projection-defined population, neurons exhibit heterogeneous activity profiles (Beyeler

et al., 2016). Thus, future study will have to solve this important question with finer granularity, such as di-synaptic projection specificity (see **Project 2**). Another important hypothesis driven by Herry and colleagues' findings are that Fear neurons and Extinction neurons interact locally to suppress each other and control the balance between them. This scenario very likely involves local BLA interneurons such as PV+ neurons (Davis et al., 2017). Alternatively, coordinated activity of intercalated clusters (see **2.3.4**) externally orchestrates those opposing populations. I directly addressed the latter possibility in **Project 1**.

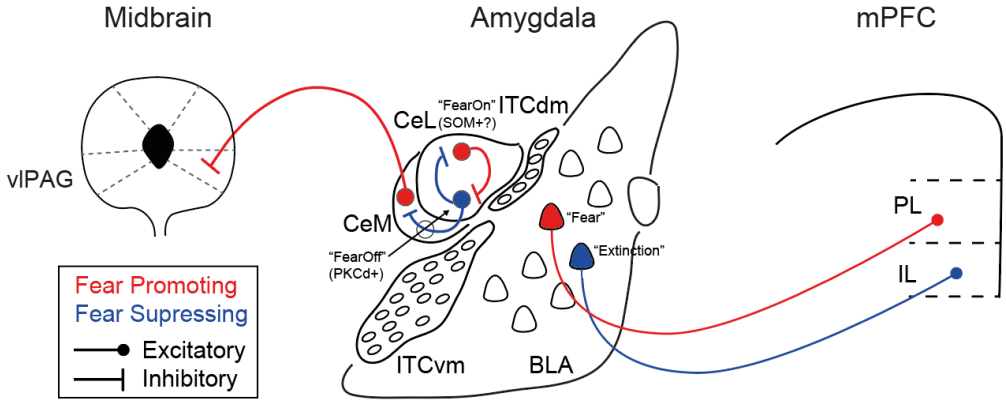

Fig. 3 | **Projection and local circuits of the basolateral and central amygdala underlying fear and extinction.**

2.3.3. Central amygdala

The central amygdala (CeA) has been thought to be a passive relay station sorting pre-processed information in the BLA out to brainstem downstream targets, including PAG or hypothalamus. However, recent studies suggest that CeA is also actively involved in fear memory formation (Ciocchi et al., 2010; Wilensky et al., 2006). Cell-type-specific circuit-level approach supports these earlier findings; Protein kinase C-δ expressing neurons (PKCδ+) show inhibition upon fearful CSs presentation and chemogenetically inhibiting this population leads to higher freezing (Ciocchi et al., 2010; Haubensak et al., 2010). In addition, BLA inputs onto SOM+ CeA are potentiated upon fear learning (Li et al., 2013). As PKCδ+ and SOM+ neurons in the lateral CeA (CeL) are largely mutually exclusive (Li et al., 2013), together with the finding that SOM+ neurons provide selective inhibition over the medial subdivision of CeA (CeM), which contains fear-mediating output neurons (LeDoux et al., 1988), a disinhibitory motif in the CeA was hypothesized (**Fig. 3**). However, recent virus-based circuit mapping studies found that CeL also contains a substantial amount of output neurons projecting to vlPAG (Penzo et al., 2014; Tovote et al., 2016; Xu et al., 2016). Thus, future studies will have to revise a classic model where the CeM exclusively serves as the brainstem output station of the amygdala.

2.3.4. Intercalated amygdala neurons

In contrast to extensively investigated amygdala nuclei BLA and CeA, functions of the intercalated (ITC) neurons are under-studied, and thus, still remain somewhat mysterious and elusive. In this section, I will summarize what is known and hypothesized about ITC neurons and list important remaining questions to be addressed in future work.

Basic properties of ITC neurons

ITC neuron is a peculiar small-sized GABAergic cell-type, constituting densely packed

clusters distributed in fiber bundles encapsulating the BLA (Millhouse, 1986). It is distinct from other GABAergic cell types found in the BLA and CeA in many aspects.

First, their developmental origin is different from others'. While BLA interneurons and CeA neurons are derived from medial/caudal ganglionic eminence and ventrolateral ganglionic eminence, respectively, dorsolateral ganglionic eminence selectively gives rise to ITC neurons with a distinct developmental genetic program (Kuerbitz et al., 2018, 2020; Waclaw et al., 2010).

Second, the cytoarchitecture of ITC neurons is unique. Unlike spatially salt-and-peppered organizations of BLA interneurons and each subtype of CeA neurons, ITC neurons make densely packed clusters (or cell masses) while thin cell strands seem to connect individual clusters forming a complex net encapsulation caudal side of the BLA (Milhouse, 1986). The organization of clusters seems to slightly differ even between rats and mice. In mice, three main clusters – dorsomedial (ITC_{dm}), dorsolateral (ITC_{l}), and ventromedial (ITC_{vm}) – are well reported (**Fig. 3**; see also Busti2011 for earlier 3D reconstruction; I updated cluster nomenclature in **Project 1**). In addition, except for a rare (< 5%) large-sized non-GABAergic ITC neurons found along the edges of the clusters (Bienvenu et al., 2015; Busti et al., 2011; Nitecka and Frotscher, 1989), and for a nitric oxide synthase (NOS) and somatostatin (SOM) positive paracapsular population (Bocchio et al., 2016; McDonald et al., 2012), all the ITC neurons are small-sized (7-12um) medium-spiny neurons with a round or fusiform shape.

Third, electrophysiological properties are also largely different from other amygdala neurons. Probably due to its small size, ITC neurons display high input resistance and low membrane capacitance (Amir et al., 2011; Busti et al., 2011; Geracitano et al., 2007; Marowsky et al., 2005) (see (Palomares-Castillo et al., 2012) for a summary). In vitro slice recordings pointed out a voltage-dependent K^+ conductance that inactivates in response to suprathreshold depolarizations, making ITC neurons hyperexcitable and supporting long-lasting tonic firing (Royer and Paré, 2003; Royer et al., 2000). Although in vivo recording from these tiny clusters were virtually impossible in small model animals such as rodents, Collins and Pare and colleagues utilized chronic implantation of electrodes in unanaesthetised cats and indeed found that ITC neurons show high-frequency spontaneous activity (Collins and Paré, 1999), suggesting a tonic inhibition allowing disinhibitory mechanisms in its downstream.

Finally, marker protein expression differentiates ITC neurons from surrounding other amygdala neurons. They, for example, exhibit strong immunoreactivity (protein expression) of dopamine receptor type1 (D1R), μ-opioid receptor (μOR), metabotropic glutamate receptor 7 (mGluR7), and several transcription factors including FoxP2 and Meis2 (Herkenham and Pert, 1982; Jacobsen et al., 2006; Kaoru et al., 2010). In spite that in vitro studies showed that both opioid and dopamine signaling hyperpolarize ITC neurons (Blaesse et al., 2015; Marowsky et al., 2005), their in vivo functions are not known.

Connectivity of ITC neurons

Because of its location between BLA and CeA, ITC_{dm} and ITC_{vm} have long been postulated to serve as an intermediate station mediating information flow from BLA to CeA. Indeed, BLA principal neurons form glutamatergic connections with medial ITCs (Jüngling et al., 2008; Royer et al., 2000). In turn, neurons in medial ITC clusters project to CeA, providing feedforward inhibition (Geracitano et al., 2007; Paré and Smith, 1993; Royer et al., 1999, 2000). In addition, the other direction of connections, from ITC_{dm} and ITC_{vm} to the BLA were also reported (Asede et al., 2015; Gregoriou et al., 2019).

As described above, principal ITC neurons appear to be largely homogenous regarding their cytoarchitecture. In contrast, ITC neurons are heterogeneous even within the same cluster in

terms of their external projection targets (Busti et al., 2011; Geracitano et al., 2007; Mańko et al., 2011), for example, ITC_{dm} contains at least three populations projecting to either ITC_{vm}, ansa lenticularis/tail of striatum, or CeM. However, those downstream targets of ITC neurons were identified by relatively small samples of single-cell reconstruction following in vitro whole-cell recordings, and thus, thorough projection mapping with modern circuit-based approaches need to be provided by future studies, especially for long-range projections. It would also be an interesting question whether there is a relationship between their projection-target and their function, which is the case in principal BLA neurons (**2.3.2**). Similarly, information about the input sources of each cluster is limited. Although earlier tracer-based studies reported that, in addition to the BLA, thalamic/cortical areas and neuromodulatory areas project to ITCs, the field awaits comprehensive mapping using retrogradely infectious viruses such as rabies viruses (see **2.4.1**).

ITC neurons also show local connectivity within each cluster. Interestingly, connections there are rarely reciprocal (Geracitano et al., 2007), suggesting there is some logic governing local connections. Nevertheless, the evidence is again limited to somewhat anecdotal reports, and thus, more comprehensive follow-up work should be performed.

Lastly, particularly attractive connections of ITCs among others are ones between individual clusters. ITC_{dm} and ITC_{vm} send their axonal projections to each other and make functional GABAergic connections (Busti et al., 2011; Geracitano et al., 2007). An intriguing finding obtained in the guinea pig, where medial ITC neurons make several clusters instead of two, is that connections between medial ITC clusters are polarized in such a way that a cluster located dorsally inhibit the next cluster located ventrally in a serial manner (Royer et al., 2000). This organization allows for complex inhibitory-disinhibitory-inhibitory interactions and binary-like computation (e.g. 0,1,0,1,...), suggesting precise spatiotemporal processing. Although mice exhibit only two medial ITC clusters, it was also postulated that ITC_{dm} dominantly inhibits ITC_{vm} (Duvarci and Pare, 2014). I updated this view by showing that ITC_{dm} and ITC_{vm} are reciprocally densely connected and forming a mutual inhibition motif (**Project 1**).

Roles of ITC neurons in fear and extinction

As described earlier, the neuronal activity of distinct neurons in the BLA and CeA possess critical roles in fear processing. Medial ITC clusters are interposed between the BLA and CeA, and thus, appear to be strategically suited to provide inhibition over BLA, by reducing the general excitability of the BLA (general inhibition model: (Marowsky et al., 2005; Pape, 2005), or by gating information flow from BLA to CeA (gating model: (Duvarci and Pare, 2014; Pape and Pare, 2010; Paré et al., 2004; Royer et al., 1999), and thus, have been highly implicated in fear extinction. Indeed, pharmacologically interfering with whole medial ITC clusters (both ITC_{dm} and ITC_{vm}) by means of toxin selectively targeting μOR-expressing neurons, attenuated extinction retrieval (An et al., 2017; Likhtik et al., 2008). Complementary, increasing BLA input to ITCs by means of neuropeptide S enhanced extinction learning and retrieval (Jüngling et al., 2008). Furthermore, extinction-related plasticity was identified in medial ITC neurons. In fear extinguished rats, BLA to medial ITCs excitatory connections were strengthened, in turn, ITCs provide enhanced inhibitory input onto the CeM neurons compared to in naïve or fear conditioned animals (Amano et al., 2010). The authors also showed that this effect is dependent on activity of IL, a subdivision of mPFC, which are implicated in fear extinction (Milad and Quirk, 2002). Collectively, those findings consolidated the view that ITC clusters, as a whole, are important for fear extinction. Important to add, Amano and colleagues performed ITC recordings from the adjacent BLA-CeA border region in rats, where ITC neurons only exist sparsely, at least in mice. This factor confounds to conclude whether ITC_{dm}, ITC_{vm}, or both exert this plasticity associated with fear extinction, awaiting future study to follow up.

Another line of research, however, reported that distinct medial ITC clusters could be selectively recruited in fear expression or in the retrieval of fear extinction (Busti et al., 2011; Hefner et al., 2008; Whittle et al., 2010). They used immediate early gene *Zif268* expression as a readout of neuronal activity and found that ITC_{dm} neurons are predominantly activated by fear recall, whereas ITC_{vm} neurons are activated by fear extinction, suggesting that ITC_{dm} and ITC_{vm} might have rather opposing roles in fear and extinction. Nevertheless, immediate early gene expression is only an indirect measure of neuronal activity and lacks temporal resolution (see **2.4.**), making it impossible to know what feature of fear and extinction activated those clusters differentially.

Whether IL directly provides excitatory input to ITC neurons is a research topic under active debate. It had been a generally accepted view that engagement of the BLA in extinction is gated by IL (Milad and Quirk, 2002; Sierra-Mercado et al., 2011; Sotres-Bayon et al., 2012) and that IL in parallel drives medial ITC clusters to provide feedforward inhibition on CeA thus inhibiting output from the amygdala (Amir et al., 2011; Berretta et al., 2005; Likhtik et al., 2005, 2008). However, a resent tracing study found almost no innervation from IL to medial ITCs (Pinard et al., 2012), and following optogenetics-assisted in vitro recording studies found that IL did not provide direct synaptic connections to ITCs but di-synaptically recruited ITCs via BLA (Cho et al., 2013; Strobel et al., 2015), and that rather PL (or more in general, dmPFC) provided direct input to ITCs (Adhikari et al., 2015). This recent evidence thus challenged a canonical view.

In spite of this recent progress, notably, mainly because of the methodological difficulties raised by the small size of ITC clusters and lack of genetic access, characterizing endogenous activity dynamics of neurons in distinct ITC clusters at single-cell resolution in behaving animals has been virtually impossible. Moreover, the question of how ITC clusters control functionally heterogeneous BLA and CeA populations in an orchestrated manner is unaddressed. In **Project 1**, I directly answer those questions by combining cutting-edge methodologies, including calcium imaging, tissue clearing, and virus-based circuit mapping (see **2.4.**).

2.4. Technical advances for the study of neuronal circuits

The recent two decades have witnessed eye-opening methodological advances that drive neuroscience research, especially cell-type-specific circuit neuroscience (Luo et al., 2008, 2018). In this section, I briefly summarize some of those new technologies that directly contributed to my thesis projects.

2.4.1. Genetic and viral tools

To achieve the operational definition – defining cell types using genetic tools that allow us to access specific subsets of neurons – several approaches have been devised. A strong advantage of executing research with the lab mouse is that it is highly genetically tractable. In particular, due to rapid progress in CRISPR-based genome editing (Hsu et al., 2014; Zhang, 2019), it is getting more accessible to generate genetically modified mice, including transgenic, knock-in/knock-out mice. In the context of cell-type-specific neuroscience study, so-called “Cre-driver” lines (Gerfen et al., 2013; Gu et al., 1994; Taniguchi et al., 2011; Tsien et al., 1996), which express Cre-recombinase only in a specific cell type has been widely used. Crossing them with “reporter” lines (Daigle et al., 2018; Madisen et al., 2010; Soriano,

1999), which express fluorescent protein- or functional protein-coding exogenous sequence in a Cre-dependent manner, allows us to flexibly realize cell-type-specific labeling, manipulation, or recording with various combinatorial possibilities.

A limitation of the "Cre-driver x reporter" approach is that, unless Cre expression is spatially restricted in a driver line, it is not possible to achieve spatially restricted, or brain-area-targeted expression of proteins of interest. To overcome this issue, a recombinant viral vector-based genome delivery system has been exploited. By controlling injection coordinates and volumes, experimenters can target microstructures in the brain at as precise as a ~10*10*10um^3 voxel resolution. Several neurotropic viruses such as adenoviridae (e.g. canine adenovirus 2), herpesviridae (herpes simplex), togaviridae (sindbis), and retroviridae (lenti) have been successfully applied (Nectow and Nestler, 2020). Here, I summarize the two most important viral vectors for projects in this thesis – adeno-associated virus (AAV, parvoviridae) and rabies virus (Rhabdoviridae).

Since its introduction, recombinant AAVs are currently the most widely used viral vector in modern circuit neuroscience research because it enables low- (or none-) toxic transduction of postmitotic non-dividing neurons and long-term stable gene expression (Klein et al., 1998; Samulski et al., 1989). These properties, together with low possibility of genome integration, also make AAV an prime candidate for clinical application (Haggerty et al., 2020; Roska and Sahel, 2018; Sahel et al., 2021). To achieve cell-type-specific labeling, there are largely three different yet combinable approaches: promoter, tropism, and intersection genetic switches such as above mentioned Cre-recombination system. Using cell-type-specific promoters is the most straightforward approach. However, because mammalian endogenous promoters are often large, it is challenging for AAVs due to its packaging capacity (< 5.0kb) (Dong et al., 1996). Although truncated or minimal promoters such as truncated human *synapsin-1* and minimal *fos* promoters have been introduced to circumvent this issue, they do not necessarily reflect endogenous expression patterns, precluding precisely predictable genetic access. The tropism (cell type–selective infectivity) of AAV serotypes has also been assessed for targeting specific cell populations. As each AAV serotype differs in capsid proteins, protein engineering with selection techniques has led to several cell-type-specific serotypes (Chan et al., 2017; Deverman et al., 2016; Ogden et al., 2019). Nevertheless, so far a variety of accessible cell-types with this strategy is very limited. Finally, the intersectional approach would currently be the most effective and convenient. This can be implemented with a Cre-dependent component such as loxp-stop-loxp, flip-excision (FLEX) or DIO, and a strong ubiquitously expressed promoter such as *CAG* or EF1α (Atasoy et al., 2008; Kuhlman and Huang, 2008; Sohal et al., 2009). By combining these Cre-dependent AAVs with cell-type specific Cre-driver lines, both cell-type-specificity and spatial selectivity can be realized.

Unlike AAVs, rabies viruses are selected for their preferential retrograde trans-synaptic infectivity. Wild-type rabies viruses, which have the ability to traverse multisynaptic pathways and the ability of replication to amplify signals in individual neurons, have been used for transneuronal circuit tracing for decades (Callaway, 2008; Ugolini, 1995). As the rabies virus is an RNA virus and does not have DNA phase in the life cycle, using promoters or Cre-recombination-based approach for cell-type-specific transduction. Thus, more recently, pseudotyped G-protein-deleted rabies viruses were engineered (Wickersham et al., 2007a, 2007b). By replacing G-protein coding region with GFP (or other functional proteins, Osakada2011) and replacing G-coating of the envelope membrane with EnvA, an avian virus envelope, pseudotyped viruses cannot infect mammalian cells. Therefore, by exogenously expressing TVA, a receptor for EnvA, in a cell-type-specific manner, selective infection to specific cell-type specificity was achieved. Since G-protein is essential both for the formation of new viral particles and transsynaptic jumping, G-protein is also expected to be

exogenously expressed in the same population, leading to cell-type-specific presynaptic mapping. This rabies virus-based trans-synaptic circuit mapping with manipulation and activity-monitoring serves as the core methodology for **Project 2**.

Collectively, those methods allow for visualizing, monitoring activities, and perturbing activities of specific subpopulations of neurons of interest.

2.4.2. In vivo calcium imaging

Historically, to make physiological recordings from living neurons, including those of living animals, electrophysiological recordings with electrodes have been widely used as a standard method. However, until very recently, the number of cells that could be recorded simultaneously was small (Jun et al., 2017; Steinmetz et al., 2021), and it is technically difficult to perform chronic recordings while tracking the same neurons. In addition, it is known that there is a substantial bias in sampling, for example, electrically silent neurons are inherently missed. To overcome these limitations, calcium imaging has been developed as a powerful alternative approach, in which cytosolic calcium ion concentration serves as a proxy for neuronal activity.

Early calcium imaging recordings were performed with synthetic fluorescent calcium dyes, which were initially developed by Tsien's group in the 1980s (Tsien, 1980). This allowed for measuring both action potential-related activity and synaptic input-related calcium influx in micro compartment such as dendrites and dendritic spines (Yuste and Katz, 1991). Combined with 2-photon microscopy (Denk et al., 1990), which allows for visualizing neurons located deep in scattering tissue, calcium imaging from single neurons revealed several important basic properties of neurons (Svoboda et al., 1997; Yuste and Denk, 1995). The development of bulk loading techniques using acetoxymethyl (AM) ester dyes, which can label virtually every neuron in a local circuit and allows for imaging hundreds to thousands of neurons simultaneously, further accelerated the spread of its application both to in vivo (Ohki et al., 2005; Stosiek et al., 2003) and in vitro (Ikegaya et al., 2004) configurations. However, chemical dyes essentially precluded chronic recordings and cell-type specific targeting.

To circumvent practical limitations of chemical calcium indicators, genetically encoded calcium indicators (GECIs) have gradually taken over use cases of synthetic dyes. Starting from FRET-based (Förster resonance energy transfer) sensors such as "Cameleon" series (Miyawaki et al., 1997), single-wavelength indicators, especially the ones dependent on circularly permuted green fluorescent protein designs (cpGFP), such as "Pericams" (Nagai et al., 2001) and "G-CaMP" (Nakai et al., 2001) have become the most popular design. This is primarily because cpGFP-based sensors are substantially brighter and conventional fluorescent microscopes sufficed to measure the signal. A considerable effort has been made to improve the sensitivity of sensors both by a combination of error-prone PCR-based mutagenesis and large-scale screening (Chen et al., 2013; Dana et al., 2016, 2019; Tian et al., 2009; Wardill et al., 2013) and by rational protein designing (Inoue et al., 2015, 2019), led to several refined G-CaMP (or GCaMP) derivatives. As it provided a single-action potential readout and allowed for monitoring calcium dynamics in single dendritic spines, GCaMP6 series have been particularly widely used (Chen et al., 2013).

Since in vivo 2-photon calcium imaging necessitates a head-fixed configuration (but see (Flusberg et al., 2008; Helmchen et al., 2001; Sawinski et al., 2009; Zong et al., 2017, 2021) for a series of effort for head-mountable 2-photon microscopes), and applications were mainly limited to cortical tissues. To expand the application of calcium imaging to deep brain

structures in freely moving mice engaging learning and memory tasks, Schnitzer and colleagues devised ultra-light head-mountable 1-photon microscopes (miniaturized microscope), and in combination with a GRIN lens (Graded-index) microendoscope, demonstrated long-term single-cell resolution calcium imaging in subcortical structure, including the hippocampus and the amygdala (Ghosh et al., 2011; Grewe et al., 2017; Ziv et al., 2013). As a trade-off, unlike 2-photon microscopy, identifying several cell types simultaneously using multiple wavelengths is not possible with the miniaturized microscope. In this thesis, I fully exploited this deep-brain calcium imaging method in all the publications and further established a tissue clearing-based post-hoc cell-type profiling pipeline to complement the shortcomings of the miniaturized microscope. I summarize this in the next section.

2.4.3. Tissue clearing-based post-hoc molecular profiling

Tissue clearing enables histological analysis without slicing the tissue, and thus, provides unambiguous 3D spatial information. The basic principle of making opaque tissues transparent is delipidation and subsequent refractive index-matching (RI) (see (Susaki and Ueda, 2016)for review). As lipid is the most light-scattering material in most of the biological tissues including the brain, firstly, it has to be removed. Dozens of methods have been reported and they can be largely divided into solvent-based approaches or aqueous detergent-based ones. Subsequently, the RI-matching process involves reagents with RI ranging 1.4-1.5. The idea is to remove water (low RI) and lipid (high RI) from the tissue and then to fulfill the space with reagents with similar RI of remaining components such as protein. Some tissue clearing methods do not only make tissues transparent, also make tissues highly permeable and allow for molecular profiling including antibody staining and in situ hybridization (Chen et al., 2016; Chung et al., 2013; Renier et al., 2014; Susaki et al., 2014, 2020; Tillberg et al., 2016).

To supplement molecular profiles in a post-hoc manner with neurons that are functionally characterized by 2-photon calcium imaging, conventional thin sectioning-based approaches have been used (Kerlin et al., 2010; Khan et al., 2018; Xu et al., 2020). However, methodological difficulty in registering two image data sets resulted in relatively low yield. Thus, I thought combining tissue clearing-based molecular profiling with calcium imaging should facilitate post-hoc identification of neurons by directly aligning 3D image datasets. This combination enabled the core of this thesis, **Project 1**.

2.5. Aims of this thesis

In this thesis, I aim to address the above-described issues. In **Project 1**, I characterize functions of the intercalated amygdala neurons in fear and extinction. In **Project 2**, I demonstrate that BLA neurons di-synaptically contacting vlPAG are the core pathway for fear memory formation.

3. Results and Discussion

3.1. **Project 1**: Intercalated amygdala clusters orchestrate switch in fear state (published as Hagihara et al., 2021, *Nature*)

Kenta M. Hagihara [1,2], Olena Bukalo [3], Martin Zeller [4], Ayla Aksoy-Aksel [4,5], Nikolaos Karalis [1], Aaron Limoges [3], Tanner Rigg [3], Tiffany Campbell [3], Adriana Mendez [3], Chase Weinholtz [3], Mathias Mahn [1], Larry S. Zweifel [6,7], Richard D. Palmiter [8,9], Ingrid Ehrlich [4,5], Andreas Lüthi [*1,2], Andrew Holmes [*3]

[1] Friedrich Miescher Institute for Biomedical Research, Maulbeerstrasse 66, 4058 Basel, Switzerland
[2] University of Basel, 4000 Basel, Switzerland
[3] Laboratory of Behavioral and Genomic Neuroscience, National Institute on Alcohol Abuse and Alcoholism, NIH, Bethesda, MD, USA
[4] Hertie Institute for Clinical Brain Research and Center for Integrative Neuroscience, 72076 Tübingen, Germany
[5] Department of Neurobiology, Institute for Biomaterials and Biomolecular Systems, University of Stuttgart, 70569 Stuttgart, Germany
[6] Department of Psychiatry and Behavioral Sciences, University of Washington, Seattle, WA, USA
[7] Department of Pharmacology, University of Washington, Seattle, WA, USA
[8] Howard Hughes Medical Institute, University of Washington, Seattle, WA USA
[9] Departments of Biochemistry and Genome Sciences, University of Washington, Seattle, WA, USA
[*]correspondence should be addressed to A. Lüthi. and A. Holmes.

Summary
Adaptive behaviour necessitates that memories are formed for fearful events, but also that these memories can be extinguished. Effective extinction prevents excessive and persistent reactions to perceived threat, as can occur in anxiety and 'trauma- and stressor-related' disorders[1,2]. However, while there is evidence that fear learning and extinction are mediated by distinct neural circuits, the nature of the interaction between these circuits remains poorly understood[3-8]. Here, through a combination of *in vivo* calcium imaging, functional manipulations, and slice physiology, we demonstrate that distinct inhibitory clusters of intercalated neurons (ITCs) located in the amygdala exert diametrically opposite roles during the acquisition and retrieval of fear extinction memory. Furthermore, we find that the ITC clusters antagonize one another via mutual synaptic inhibition and differentially access functionally distinct cortical- and midbrain-projecting amygdala output pathways. Our findings show that the balance of activity between ITC clusters represents a unique regulatory motif orchestrating a distributed neural circuitry regulating the switch between high and low fear states. This suggests a broader role for the ITCs in a range of amygdala functions and associated brain states underpinning the capacity to adapt to salient environmental demands.

Main
Animals are equipped with biological systems to detect and defend against environmental threats. Through associative learning, stimuli predicting threat can mobilize defensive responses to mitigate harm[9,10]. However, when threat-associated stimuli become innocuous, responses must adapt through the process of extinction, whereby a new memory is formed that coexists in opposition to the original fear memory[7,11-14]. Specialized neural systems have evolved to subserve fear and extinction which, when imbalanced, can cause persistent reactions to threat, as occurs in 'trauma- and stressor-related' disorders[2]. However, the

mechanisms governing the balance between fear and extinction at the neuronal circuit level are poorly understood.

One critical node within the neural circuitry underlying fear and extinction is the ITC clusters; densely packed GABAergic neurons surrounding the basolateral amygdala (BLA), distinguished from neighbouring neurons by their electrophysiological properties and distinct molecular phenotype[15-18]. The medial ITC clusters, located in the intermediate capsule at the BLA-central amygdala (CeA) junction, receive BLA input and modulate CeA activity through feed-forward inhibition[3,19] in a manner potentiated by extinction[20-22]. Accordingly, permanent ablation of the entire medial ITCs impairs extinction[22,23]. However, recent studies suggest functional heterogeneity between individual medial ITC clusters. Immediate-early gene (IEG) mapping demonstrates that fear and extinction differentially activate dorsomedial and ventromedial ITC clusters[15,24]. These clusters also have different inputs and output targets[25-27]. Yet due to their small size and location deep in the brain, it has proven challenging to elucidate ITC functions *in vivo* using traditional techniques.

ITC clusters differentially signal the presence and absence of an aversive stimulus

To overcome the difficulty in accessing the small ITC clusters, we employed *in vivo* deep-brain imaging to monitor Ca^{2+} activity in individual ITC neurons in freely moving mice, via a miniaturized microscope[28]. We separately targeted neurons in the dorsal cluster ITC_{dm} (corresponding to the Imp, 'anterior paracapsular' (Iap) and dorsal-most part of the 'intramedullary gray' (IMG) as defined in[14]) and ventral cluster ITC_{vm} (corresponding to the posterior portion of IN, according to[14]). Anatomical demarcation of the two clusters was demonstrated using tissue clearing-based immunohistochemical (IHC) labelling of Forkhead box protein P2 (FoxP2), as well as FoxP2-Cre;Ai14 (tdTomato reporter) and D1R-Cre;Ai14 mouse lines (FoxP2 and the dopamine D1 receptor are known markers for ITC neurons[14,17]) (**Extended Data Fig. 1, Supplementary Movie 1, Supplementary Table 1,** see **Methods**). To simultaneously target ITC_{dm}, BLA, and CeA, an adeno-associated virus (AAV) encoding a Ca^{2+} indicator, GCaMP6f was injected into the amygdala (**Extended Data Fig. 2a-c**), and a graded refractive index (GRIN) lens implanted (**Fig. 1a,b**). To isolate ITC_{dm} Ca^{2+} responses, we performed tissue clearing-based immunohistochemical (IHC) labelling of FoxP2, and selected FoxP2+ neurons from the GRIN lens images for analysis by registering maximum intensity projection Ca^{2+} images to 3D confocal images of cleared tissue (**Fig. 1c-e, Supplementary Movie 2,** see **Methods**).

Implanted mice were tested in a 5-day fear conditioning and extinction paradigm (see **Methods** and **Fig. 2a**). We first limited analysis to the shock-evoked Ca^{2+} responses during fear conditioning (Day2) – comprising 5 pairings of an auditory conditioned stimulus (CS) with a footshock unconditioned stimulus (US). We found footshocks reliably elicited strong responses in ITC_{dm} neurons (**Fig. 1f,g,j, Extended Data Fig. 2d, Supplementary Movie 3**) whereas, consistent with previous findings[28], simultaneously recorded neurons in CeA and BLA exhibited sparse and heterogeneous footshock responses (**Fig. 1f,g, Extended Data Fig. 2d**). Additional *in vivo* 2-photon Ca^{2+} imaging experiments performed in head-fixed animals, providing higher spatial resolution and simultaneous cell-type identification, confirmed that most ITC_{dm} neurons responded to shock, and that the shock-responsive cluster corresponds to ITC_{dm} at single-cell resolution (84.5%, 93/110 neurons, N = 5 mice, **Extended Data Fig. 3a-e**).

In contrast to ITC_{dm} neurons, we found that ITC_{vm} neurons did not show footshock responses (**Fig. 1h-j, Extended Data Fig. 2e-h**). The fraction of shock-responsive ITC_{vm} neurons was significantly smaller than for ITC_{dm} ($P = 1.6 \times 10^{-48}$, Chi-squared test). In addition, the activity of ITC_{dm} neurons, but not ITC_{vm}, was highly correlated during fear conditioning and during a home-cage session (**Extended Data Fig. 2i-n**), further supporting functional differences between the clusters. Finally, by employing dual-colour *in vivo* fibre photometry to

simultaneously measure the activity of ITC_{dm} and ITC_{vm} projections in the BLA, we found the activity in the two populations to be largely anti-correlated **(Extended Data Fig. 3f-j)**.

As extinction is based on the absence of an expected aversive stimulus[29,30], and the ITCs are ascribed a role in extinction[3,31,32], we next asked whether the clusters also differentially respond to omission of expected shock. To do so, we examined the extinction training session (Day3, see **Methods** and **Fig. 2a**), whereby mice were presented with the CS alone (25x), and aligned Ca^{2+} traces to CS-offset, when footshocks would have been delivered during conditioning. During the first 5 CS/no-US trials, the fraction of neurons responding to US-omission was greater in ITC_{vm} (28%) than ITC_{dm} (4%; $P = 5.8 \times 10^{-15}$, Chi-squared test), as was the average size of the omission response (**Fig. 1k,l, Extended Data Fig. 3k,l**). However, by the end of extinction training (trials 21-25), shock-omission responses in ITC_{vm} were markedly reduced, indicating they do not merely represent CS-offset, but reflect deviations from expectation. Together, these data demonstrate that ITC_{dm} and ITC_{vm} neurons oppositely represent the presence and absence of an aversive stimulus. These opposing functional profiles likely reflect differential connectivity with upstream brain regions. For example, shock responses of ITC_{dm} could be driven by multisensory and pain processing areas, such as the medial geniculate nucleus/posterior intralaminar nucleus thalamic complex[26,33,34].

CS responses of ITC clusters parallel the switch from high to low fear state

We next asked whether the clusters also exhibit differential fear state-dependent responses to conditioned CSs. We measured Ca^{2+} activity in ITC_{dm} and ITC_{vm} neurons as mice underwent successive sessions of CS/context habituation (Day1), CS-US conditioning (FC, Day2), CS-only extinction training (Ext1, Day3), additional extinction training (Ext2, Day4) and, finally, extinction retrieval (Retrieval, Day5) (**Fig. 2a,** see **Methods**). CS-elicited freezing, a readout of fear state, increased across conditioning trials and was maintained at fear retrieval (i.e., the early extinction trials on Day3) before progressively decreasing with extinction training, and remaining low on extinction retrieval (**Fig. 2b**).

We then functionally classified ITC neurons into three mutually exclusive categories, as previously applied to BLA neurons[22,35-37]. Fear neurons were selectively active during fear retrieval/early extinction, Extinction neurons developed responses by late extinction, and Extinction-resistant neurons showed sustained activity across extinction training (**Fig. 2c, Extendend Data Fig. 4a-c,** see **Methods**). ITC_{dm} contained a large fraction of Fear neurons (75% of CS-responsive neurons, 32% of recorded, $P < 0.01$), but only a small fraction of Extinction neurons (15% of CS-responsive neurons, 6% of recorded, $P < 0.01$) (**Fig. 2d, Extended Data Fig. 4d**). Conversely, there was an overrepresentation of Extinction neurons in ITC_{vm} (74% of CS-responsive neurons, 18% of recorded, $P < 0.01$), with a much smaller fraction of Fear neurons (18% of CS-responsive neurons, 5% of recorded, $P < 0.01$). There was only a small fraction (<5%) of Extinction-resistant neurons in either cluster ($P > 0.1$). Examining the dynamics of these responses revealed that most of ITC_{dm}-Fear neurons showed an onset-locked CS response during early extinction, suggesting rapid detection of the aversive properties of the CS. CS responses were much reduced, but not completely absent, at extinction retrieval (**Fig. 2e**). Conversely, CS-responses in ITC_{vm}-Extinction neurons emerged by the second session (Day4) of extinction training and these were maintained on extinction retrieval (Day5) (**Fig. 2e**). The delayed increase in ITC_{vm} neuron responses until Day4 suggests that a sufficient amount of extinction training and/or overnight extinction memory consolidation is required to recruit their activity; reminiscent of a similar pattern seen in BLA Extinction neurons[35].

Providing further evidence of the divergent activity in the two clusters, the overall amplitude of CS-responses positively correlated with freezing in ITC_{dm}-Fear neurons, but was anti-correlated with freezing in ITC_{vm}-Extinction neurons (**Fig. 2f,g**). These relationships held when considering all the recorded (not just functionally classified) neurons (**Extended Data Fig.**

5a,b). Importantly, ITC_{vm} neurons did not show tone responses on habituation (Day1), indicating that ITC_{vm} activity does not simply reflect a low fear state but represents the diminished fear state produced by extinction (**Extended Data Fig. 5c**). In contrast, ITC_{dm} neurons showed tone responses on habituation (Day1), which rapidly reduced across 5 trials, suggesting a habituation-like response to novelty and/or an attenuation of a response to the new tone's aversive properties (**Extended Data Fig. 5d**). Additional analysis showed that averaged Ca^{2+} traces from ITC_{dm}-Fear and ITC_{vm}-Extinction neurons aligned to freezing onset or offset did not indicate a strong correlation with freezing behaviour (**Extended Data Fig. 5e**).

When aligning responses to US-omission, ITC_{vm}-Extinction, but not ITC_{dm}-Fear, neurons showed strong responses (**Extended Data Fig. 5f)**. This finding is consistent with the shock-omission responses observed on Day3 of testing for the entire recorded ITC_{vm} population (**Fig. 1k,l**), which decreased on Day5 (**Extended Data Fig. 5g**). Indeed, US-omission responses were weakly positively correlated with extinguished (Day4) CS-responses ($R = 0.36$), suggesting functional overlap between ITC_{vm} neurons signalling shock-omission and extinction (**Extended Data Fig. 5h**). Collectively, these data show that the relative balance of activity between ITC_{dm} and ITC_{vm} neurons represents the prevailing conditioned fear state of the animal.

An intriguing corollary to these findings is whether interplay between the two ITC clusters is evident in other situations characterized by a shift from one behavioural state to another. To address this question, we used dual-cluster *in vivo* fibre photometry to simultaneously record Ca^{2+} activity in ITC_{dm} and ITC_{vm} neurons as mice explored an elevated zero maze (**Extended Data Fig. 6a)**. This experiment revealed that transitions between the closed and open quadrants of the maze corresponded to a marked shift in the balance of activity in the two clusters (**Extended Data Fig. 6b-e)**. Specifically, increased ITC_{vm} activity occurs when the animal moves from the protected, closed, to the unprotected, open, quadrants. Potentially, this increase in ITC_{vm} neuron activity may serve to inhibit defensive behaviour and thereby enable exploration of the unprotected open quadrants, analogous to the inhibition of freezing behaviour following extinction. These data suggest that a shift in the relative weighting of ITC cluster activity may more generally correspond to transitions between distinct behavioural states in response to changes in current environmental conditions.

ITC clusters differentially and bidirectionally regulate fear extinction

Given the diametrically opposite US and CS responses in ITC_{dm} and ITC_{vm} neurons, we next asked whether behaviour in this paradigm was impacted by causally manipulating the balance of activity between the clusters using *in vivo* chemogenetics. To this end, we expressed a Cre-dependent form of the Gi-coupled kappa-opioid receptor DREADD (KORD) in either ITC_{dm} or ITC_{vm} of FoxP2-Cre mice and Cre-negative controls, and systemically injected the pharmacologically inert ligand salvinorin B (SalB) to selectively inactivate either cluster. (For functional verification via *ex vivo* neuronal recordings in acute brain slices see **Extended Data Fig. 7**; for details and illustration of targeting success rates, see the **Methods** and **Extended Data Fig. 8,9**).

We found ITC_{vm} inactivation during extinction training impaired extinction acquisition, as evidenced by higher CS-induced (but not baseline) freezing in Cre+ versus Cre- mice on extinction retrieval the following day (without inactivation) (**Fig. 3a,b**). In a separate experiment, when mice acquired extinction memory and had ITC_{vm} inactivated during extinction retrieval, retrieval was impaired (**Fig. 3c**). Thus, ITC_{vm} is necessary for both extinction formation and retrieval. In a third experiment, we used the G_q-coupled DREADD, hM3Dq and systemic clozapine-n-oxide (CNO) injection to activate ITC_{vm} neurons during extinction retrieval. Employing a partial extinction training protocol (see **Methods**) to avoid freezing floor effects, we found that activating ITC_{vm} decreased CS-induced freezing, relative to Cre- controls, indicative of facilitated extinction retrieval (**Fig. 3d,e**). Next, we expressed hM3Dq or KORD in ITC_{dm} and administered CNO or SalB, respectively, to activate or inactivate this cluster during

extinction retrieval. The effects were opposite to the same manipulations in ITC_{vm} – compared to Cre- controls, ITC_{dm} activation during extinction retrieval increased (**Fig. 3f,g**), whereas ITC_{dm} inactivation decreased, CS-induced freezing on retrieval (**Fig. 3h,i**).

The effects of these cluster-specific manipulations strongly align with our imaging data, which had shown that Fear and Extinction neurons were overrepresented in (albeit not exclusively to) ITC_{dm} and ITC_{vm}, respectively. However, the opposite effects of inactivating ITC_{dm} (extinction-impairing) versus ITC_{vm} (extinction-promoting) seems at odds with prior evidence that cluster-wide pre-retrieval toxin-lesioning impairs extinction retrieval in rats[22,23]. To address this apparent discrepancy, we expressed KORD in both ITC_{dm} and ITC_{vm} of the same FoxP2-Cre mice. When SalB was injected prior to extinction retrieval, retrieval was impaired (**Extended Data Fig. 9**), demonstrating the effects of disrupting both clusters are in fact consistent across methodologies and species.

ITC clusters are reciprocally connected and mutually inhibitory

Our next aim was to test the hypothesis that the balance of activity between ITC_{dm} and ITC_{vm} was determined by mutual inhibitory interactions between the clusters. First, we selectively injected an AAV expressing Cre-dependent synaptophysin-GFP to target ITC_{dm} or ITC_{vm} in FoxP2-Cre mice (**Fig. 4a**). This revealed strong axonal projections making synaptophysin-positive putative synaptic connections in both directions. Note, we saw no somatic expression in projection target areas, excluding injection leakage and transsynaptic infection (**Fig. 4b, c**). Then, we asked whether these axons make functional GABAergic mono-synaptic connections by selectively infecting either ITC_{dm} or ITC_{vm} with an AAV encoding Cre-dependent channelrhodopsin-2 (ChR2) (**Extended Data Fig. 10a**) and photostimulating the ChR2-expressing axons in acute brain slices, while performing whole-cell patch-clamp recordings of neurons located in the other cluster (**Fig. 4d, e**).

Using this approach, we found synaptic connections in all the recorded ITC neurons (ITC_{vm}→ITC_{dm}: n=15/15; ITC_{dm}→ITC_{vm}: n=14/14), demonstrating dense inter-cluster reciprocal connectivity. Optically-evoked synaptic responses were blocked by the $GABA_A$-receptor blocker picrotoxin, with reversal potentials close to the equilibrium potential for chloride, confirming they were GABAergic IPSCs (**Fig. 4f,g, Extended Data Fig. 10b**). Furthermore, synaptic responses persisted upon joint application of the sodium channel blocker, tetrodotoxin, and potassium channel antagonist, 4-AP, indicating the connections were monosynaptic (**Fig. 4h,i**), as suggested by the anatomical data. Additional experiments using spatially-focused light to directly stimulate the clusters confirmed these results (**Extended Data Fig. 10c-h**). These data reveal that ITC_{dm} and ITC_{vm} are reciprocally and mono-synaptically connected by functional inhibitory synapses.

ITC clusters exert selective control over amygdala outputs regulating extinction

Tightly-coupled interconnectivity between ITC_{dm} and ITC_{vm} could provide a mechanism by which the balance of activity between the clusters shifts across high and low fear states. The clusters with a given balance could then control downstream circuits to orchestrate extinction, for instance through feed-forward inhibition onto CeA neurons[3]. An intriguing alternative route is through recently described ITC inputs to BLA[15,26,27]. To test these two possibilities, we expressed a Cre-dependent, GFP-fused and soma-targeted opsin, soCoChR-EGFP, in ITC_{dm} and ITC_{vm} of FoxP2-Cre mice (**Extended Data Fig. 11a**). We devised a configuration allowing selective photostimulation of each cluster in acute brain slices via two thin-fibre-coupled LEDs (**Fig. 4j**, **Extended Data Fig. 11b-k**).

Stimulation of ITC_{vm} neurons reliably evoked a postsynaptic response (73% of recorded neurons) in the medial CeA (CeM), a known target of ITC neurons[38], whereas ITC_{dm} stimulation did so only infrequently (9% of recorded neurons) (**Extended Data Fig. 12a-e**). Moreover, within CeM, we found that ventrolateral periaqueductal gray (vlPAG) projecting

neurons, a known fear-promoting pathway[39], also preferentially received inhibitory input from ITC_{vm} (**Extended Data Fig. 12f-i**).

Next, we examined ITC outputs to BLA, focusing on IL- and PL-projecting BLA neurons based on prior evidence that these populations, while being anatomically intermingled, represent extinction-promoting and extinction-opposing BLA output pathways, respectively[36]. We did so by separately labelling the two populations with two colours of the retrograde tracer cholera toxin B (CTB) (**Extended Data Fig. 12j-m,** see **Methods**). Recording CTB+ BLA neurons and their CTB- neighbours while optically stimulating either ITC_{vm} or ITC_{dm} revealed GABAergic (i.e., PTX-sensitive) connections from ITC_{vm} to PL-projecting BLA neurons and from ITC_{dm} to IL-projectors, but not vice versa (**Fig. 4j-n**). The connections from ITC_{dm} to IL-projecting BLA neurons were stronger (**Fig. 4n,o**) as compared to those from ITC_{vm} to PL-projectors.

Together, these data demonstrate a double dissociation in connectivity from specific ITC clusters to distinct CeM and BLA output pathways. Specifically, we find that the fear-promoting BLA→PL and CeM→vlPAG pathways are more strongly inhibited by ITC_{vm} than ITC_{dm}, while ITC_{dm} makes inhibitory inputs onto the extinction-promoting BLA→IL pathway (**Fig. 4p**). Interestingly, mPFC-projecting BLA neurons are known to preferentially contact IL and PL neurons that project back to the BLA[40], and these two mPFC→BLA projections are themselves differentially involved in fear extinction[5,41]. Thus, our data reveal that the ITC_{dm} and ITC_{vm} clusters have specific and direct access to major cortico-amygdala loops regulating the acquisition and retrieval of fear extinction memories.

Discussion

Due to increasing prevalence of psychiatric disorders in which fear persists because of impaired extinction, there is intense interest in elucidating the neural mechanisms by which an appropriate balance is achieved between avoiding threat-predicting stimuli and suppressing excessive defensive behaviour after uneventful encounters with those stimuli. Here, we uncover a substrate for achieving this balance at the level of the ITC clusters located in the intermediate capsule boundary between BLA and CeA. The ITC_{dm} and ITC_{vm} clusters form a mutually inhibitory network precisely accessing functionally distinct amygdala output pathways to orchestrate a broader circuitry underlying fear states.

Direct mutual inhibitory connections between ITC clusters would be an efficient mechanism to enable shifts in the weighting of activity in response to ongoing experience with the CS, such that the ITC_{dm}→ITC_{vm} relationship at fear retrieval is dynamically transformed to ITC_{vm}→ITC_{dm} with extinction. In turn, this dynamic process is likely modulated by upstream regions conveying information to the ITCs about the sensory and valence properties of the CS and US. The identity of the key upstream regions that shape ITC coding of fear and extinction states remain to be established. While dissociable neuronal populations and subregions in other brain regions are known to exert opposite effects on extinction[6-8,42], the ITCs appear unique in accommodating mutual inhibition as spatially separated inter-cluster connectivity. An advantage of a mutually inhibitory motif, as compared to a system requiring dynamical, bidirectional changes in a single neuronal population[43,44], is that it can amplify small differences in input to an all-or-none output pattern. This type of 'winner-take-all' mechanism has the capacity to increase the signal-to-noise ratio within a circuit to generate robust circuit-output and associated behavioural states[45,46].

Our findings provide evidence supporting a revised model of the role of the ITC clusters in switching between fear states. We also found that the balance of ITC cluster activity reflected the shift in behavioural states in response to potential environmental threat in the elevated zero maze; transitions from the maze's closed to open quadrants led to a relative increase in ITC_{vm} neuron activity. This shift is consistent with a role for the ITC_{vm} in inhibiting defensive behaviour and thereby enabling exploration of the unprotected open quadrants; an effect analogous to the inhibition of freezing behaviour following extinction. Such cross-task

similarity in neuronal function is not without precedent - BLA neuronal activity during elevated plus-maze open arm exploration is anti-correlated with conditioned freezing behaviour in the same mice[47]. Thus, shifts in the relative weighting of ITC cluster activity may correspond to transitions between behavioural states in response to changes in current environmental conditions, of which extinction and elevated zero maze exploration are just two examples.

Indeed, even beyond regulating transitions between states of high and low fear or anxiety, the ITC system could have a role in a wide-range of amygdala-mediated behavioural states, in particular those involving positive valence. This is likely given increasing evidence of the overlap in neural representations between fear extinction (or omission/secession of signals with negative valence) and reward[48-50]. Furthermore, ITCs could have profound influences also on behaviours subserved by regions receiving long-range projections from the ITCs, such as the cholinergic basal forebrain[15,51]. As such, the current insights could have broad implications for understanding how the ITCs could serve as a low-level interpreter of sensory, cognitive and emotional information to orchestrate a range of amygdala functions and associated brain states that underpin the ability to respond and adapt to salient environmental demands. Importantly, these implications could extend to human behaviour, given ITCs are present in the human brain[52,53] and amygdala dysfunction is a prominent feature of various psychiatric disease states. The finding that distinct ITC clusters subserve opposing roles in fear extinction suggests the intriguing possibility that the balance of ITC activity may contribute to individual differences in susceptibility to anxiety and trauma-related disorders.

Acknowledgements

We thank F. Ferraguti (Univ. Innsbruck) for valuable discussions on ITC cluster nomenclature; J. Felsenberg (FMI), P. Tovote (Univ. Würzburg), and A. Uematsu (RikenCBS / Univ. Tokyo) for reading and commenting on earlier versions of the manuscript; T. Mrsic-Flogel (UCL), M. Häusser (UCL) and B. Roska (FMI, IOB) for discussion and serving as thesis committee members for K.M.H.; E. Susaki (Univ. Tokyo) for sharing the CUBIC protocol; Y. Tanaka (Univ. Tokyo / Harvard) for sharing the NMDG-based slice preparation protocol; L. Choo (Univ. Basel) for slice physiology demonstration; the GENIE Project (HHMI Janelia) for making GCaMP6f, jGCaMP7f, jRGECO1a materials available; Bryan Roth (UNC) for making KORD, DREADD materials available; Karl Deisseroth (Stanford) for making the ChR2 material available; Edward Boyden (MIT) for making the soCoChR material available; All the Lüthi, Holmes, and Ehrlich lab members for discussion and support, especially T. Eichlisberger for excellent animal care; FMI animal facility, microscopy core facility (FAIM), especially L. Gelman and J. Eglinger, and IT department for constant support. This work was supported by the European Research Council (ERC) under the European Union's Horizon 2020 research and innovation program (grant agreement no. 669582), and a Swiss National Science Foundation core grant (310030B_170268) (all to A.Lüthi); by the NIAAA Intramural Research Program (to A.H.); by the German Research Foundation DFG EH 197/3-1 (to I.E.); and by the Novartis Research Foundation.

Author contributions

K.M.H., O.B., A.Lüthi., and A.H. conceived the project. K.M.H performed calcium imaging experiments, virus-based circuit mapping and the slice experiments in **Fig. 4j-o, Extended Data Fig. 11, 12** and analysed the data. O.B. performed chemogenetic manipulation experiments and analysed the data with A.Limoges, T.R., T.C., A.M., and C.W.. M.Z. and A.A.A performed the slice experiments in **Fig. 4d-i, Extended Data Fig.7, 10** and analysed the data. I.E. conceived slice experiments and supervised M.Z. and A.A.A.. N.K. performed fibre photometry with K.M.H.. M.M. helped establishing the slice physiology setup and provided K.M.H. with technical training. L.S.Z. and R.D.P. provided the FoxP2-Cre mouse line. K.M.H. prepared figures and drafted the manuscript. K.M.H., A.Lüthi., and A.H. wrote the manuscript. All the authors commented on and finalized the manuscript and figures. A.Lüthi. and A.H. supervised the entire project.

Competing interests

The authors declare no competing interests.

Methods

Mice

All animal procedures were performed in accordance with institutional guidelines and with current European Union guidelines, and were approved by the Veterinary Department of the Canton of Basel-Stadt, by the local government authorities for Animal Care and Use (Regierungspräsidium Tübingen, State of Baden-Württemberg, Germany), and by the NIAAA Animal Care and Use Committee. FoxP2-IRES-Cre mice (JAX#030541)[54] were used for Cre-dependent expression of viral vectors. For some experiments where a Cre-dependent expression system was not required, Arc-CreER mice[55] crossed with a tdTomato reporter line (Ai14) were used in addition to wild-type C57BL/6J mice. For 3D reconstruction, FoxP2-IRES-Cre mice crossed with Ai14 and D1R-Cre (JAX#37156) mice crossed with Ai14 were used. All lines were backcrossed to C57BL/6J. For behavioural experiments, only male mice (aged 1.5-3 months old at the time of virus injection) were used. Both male and female mice (2-5 months old at the time of injection, unless otherwise noted) were used for virus-based circuit tracings, *ex vivo* electrophysiology and immunohistochemistry. These analyses indicated no discernible differences between males and females; however, more detailed studies will be needed to examine potential sex differences in ITC circuit anatomy and function. Mice were individually housed for at least two weeks before starting behavioural paradigms. Animals were kept in a 12-h light/dark cycle with access to food and water *ad libitum*. All behavioural experiments were conducted during the light cycle.

Surgical procedures and viral vector injections

Buprenorphine (Temgesic, Indivior UK Limited; 0.1 mg/kg BW) was injected subcutaneously 30 min prior to the surgery. Mice were anesthetized using isoflurane (5% for induction, 1-2% for maintenance; Attane, Provet) in oxygen-enriched air (Oxymat 3, Weinmann) and then head-fixed on a stereotactic frame (Model 1900, Kopf Instruments). Lidocaine + Ropivacain (Lidocain HCl, Bichsel, 10mg/kg BW; Naropin, AstraZeneca, 3mg/kg BW) were injected subcutaneously as local anesthesia prior to incision to the skin. Postoperative pain medication included buprenorphine (0.01 mg/ml in the drinking water; overnight) and injections of meloxicam (Metacam, Boehringer Ingelheim; 5 mg/kg subcutaneously) for up to three days if necessary. Eyes were protected with ophthalmic ointment (Viscotears, Alcon). Rectal body temperature of the animal was maintained at 35-37°C using a feedback-controlled heating pad (FHC) while fixed on the stereotactic frame.

Deep brain imaging: AAV2/5.CaMK2.GCaMP6f[56] (600 nl, University of Pennsylvania Vector Core, UPenn, for simultaneous imaging of CeA, ITC_{dm}, and BLA) or AAV2/9.CAG.flex.GCaMP6f (200 nl, University of Pennsylvania Vector Core, UPenn, for ITC_{vm}) was unilaterally injected into the amygdala using a precision micropositioner (Model 2650, Kopf Instruments) and pulled volume-calibrated glass capillaries (Drummond Scientific, Cat.-No. 2-000-001, tip diameter about 15 μm) connected to a Picospritzer III microinjection system (Parker Hannifin Corporation) at the following coordinates; For ITC_{dm}: AP -1.4 mm (from bregma), ML -3.3 mm (from bregma), DV 4.4 mm (from pia); For ITC_{vm}: AP -1.6 mm (from bregma), ML -3.1 mm (from bregma), DV 5.0 mm (from pia); After waiting at least 10 min for diffusion of the virus, a gradient-index microendoscope (ITC_{dm}: ϕ1.0 x 9.0 mm, 1050-002179, Inscopix GRIN lens; ITC_{vm}: ϕ0.6 x 7.3 mm, 1050-002177, Inscopix GRIN lens) was implanted. The larger diameter lens was used to record from ITC_{dm} 1) to increase the probability of capturing this relatively small cluster in the field of view and 2) to provide simultaneous recordings from BLA and/or CeA neurons from the same lens. The smaller

diameter lens was used to record from ITC_{vm} to reduce damage to the overlying CeA. For dual-colour 2-photon imaging, a cocktail of AAV2/5.CaMK2.GCaMP6f and AAV2/1.CAG.FLEX.tdTomato (University of Pennsylvania Vector Core, UPenn) (600nl, 10-20:1 mixture ratio) was unilaterally injected targeting ITC_{dm}. A sterile 21-gauge needle was used to make an incision above the imaging site to avoid excessive brain pressure. The GRIN lens was subsequently lowered into the brain with a micropositioner (coordinates; For ITC_{dm}: AP -1.4 mm, ML 3.25 mm, DV 4.35 mm (from pia); For ITC_{vm}: AP -1.6 mm, ML 3.0 mm, DV 4.8 mm (from pia)) using a custom-built lens holder and fixed to the skull using UV light-curable glue (Henkel, Loctite 4305). Surface of the skull was sealed with Vetbond (3M). Dental acrylic (Paladur, Heraeus) was used to further seal the skull and attach a custom-made titanium head bar for fixation during the miniature microscope mounting procedure. The implanted GRIN lens was protected by rapid-curing silicone elastomers.

Chemogenetic manipulation: AAV2/8(the genome of serotype 2 packaged in the capsid from serotype 8).hSyn.KORD.IRES.mCitrine[57] (Addgene plasmid # 65417, packaged by Virovek (Hayward, CA, USA)) or AAV2/8.hSyn.DIO.hM3D(Gq)-mCherry[58] (Addgene viral prep # 44361-AAV8) was bilaterally injected to FoxP2-Cre experimental animals (Cre+) and Cre-control animals in a volume of 0.15 μL per hemisphere for individual clusters or 0.25 μL per hemisphere for both medial clusters with a 0.5 μL syringe (Neuros model 7001 KH, Hamilton Robotics, Reno, NV, USA) connected to a UMP3 UltraMicroPump and SYS-Micro4 Controller or Nanoliter NL2010MC4 injector (World Precision Instruments, LLC, Sarasota, FL, USA) at the following coordinates; for ITC_{dm} targeting: AP -1.4 mm, ML ±2.95 mm, DV -4.55 mm (from bregma); for ITC_{vm} targeting: AP -1.55 mm, ML ±2.75 mm, DV -5.15 mm; for dual ITC_{dm} and ITC_{vm} targeting: AP -1.43 mm, ML ±2.75 mm, DV -4.75 mm.

Virus-based circuit tracings: AAV2/1.hSyn.flex.synaptophysin-EGFP (packaged by VectorBiolabs, 10-25nl) was target-injected into either ITC_{dm} or ITC_{vm} (with the same coordinates as shown above) of FoxP2-IRES-Cre mice. Following viral injections, pipettes were left in place for 10 min and retracted slowly to better restrict virus infection. Three to five weeks after the injection, the animals were sacrificed for histological analysis.

Ex vivo electrophysiology: For KORD functionality assay (**Extended Data Fig.7**), AAV2/8.hSyn.KORD.ires.mCitrine was injected targeting both medial ITC clusters in FoxP2-ires-Cre mice as stated above. For inter-cluster connectivity assay (**Fig. 4d-i, Extended Data Fig. 10**), AAV2/1.EF1a.DIO.HChR2(H134R)-EYFP (U.Penn) was target-injected using a precision stereotactic frame (Model 1900, Kopf Instruments) into either ITC_{dm} or ITC_{vm} of FoxP2-IRES-Cre mice as noted above. For analysis of ITC-BLA connectivity (**Fig. 4j-o**), FoxP2-IRES-Cre mice were unilaterally injected into the amygdala with 500 nl of AAV2/9.hSyn.flex.soCoChR-EGFP[59] (Addgene # 107712-AAV9) (coordinates: AP -1.5 mm, ML ±3.15 mm, DV 4.2-5.0 mm (from pia)) so that both ITC_{dm} and ITC_{vm} would be infected. Mice were allowed to recover for 5-6.5 weeks for KORD functionality assay (**Extended Data Fig.7**), and for 2-4 weeks before *ex vivo* electrophysiology experiments (**Fig. 7, and Extended Data Fig. 10**). To retrogradely label PL- or IL-projecting BLA neurons, 50 nl of 0.5% cholera toxin B conjugated to either Alexa Fluor 555 or 647 (CTB555 or CTB647) was injected into the same hemisphere of the mPFC as the AAV injection at the following coordinates (for PL targeting: AP +1.55 mm, ML ±0.3 mm, DV 1.9 mm (from pia); for IL targeting: AP +1.75 mm, ML ±0.4 mm, DV 2.5 mm (from pia)). To label vlPAG-projecting CeM neurons, 100 nl of 0.2 % CTB555 in PBS were injected into the same side of the vlPAG as the AAV injection. To avoid the subcranial midline blood sinus while targeting the vlPAG, a hole with a diameter of 0.3 mm was drilled into the skull at ±1.7 mm from midline suture, and at the level of the lambda suture. The injection capillary was then slowly lowered at a zenith angle of 26° to the target depth of

3 mm below brain surface. CTB injections and AAV injections were performed in the same surgeries.

Fibre photometry recordings: ITC_{dm} and ITC_{vm} in the same hemisphere were targeted with 25 nl of AAV2/1.CAG.Flex.NES.jRGECO1a.WPRE[60] (Addgene) and AAV2/1.CAG.Flex.jGCaMP7f.WPRE[61], respectively, or AAV2/1.CAG.Flex.jGCaMP7f.WPRE was injected to target left ITC_{dm} and right ITC_{vm}. Following virus injections, an optical cannula comprised of a bare optical fibre (ϕ 0.4) and a fibre ferrule (Doric Lenses) was implanted in the BLA (AP -1.4 mm, ML ±3.3 mm, DV 4.3 mm (from pia)) for unilateral recordings. For bilateral recordings, ITC_{dm} and ITC_{vm} clusters were directly targeted by two optical cannulas with the same coordinates as virus injections. The surface of the skull was sealed with Vetbond (3M). Dental acrylic (Paladur, Heraeus) was used to further seal the skull and attach a custom-made titanium head bar for fixation. The ferrules were protected by rapid-curing silicone elastomers.

Immunohistochemistry

Mice were deeply anaesthetized with urethane (2 g/kg; intraperitoneally) and transcardially perfused with PBS followed by 4% paraformaldehyde (PFA) in PBS. Brains were post-fixed over night at 4°C and subsequently stored in PBS at 4°C. Coronal slices (120 μm) containing the BLA were cut with a vibratome (VT1000S, Leica). Sections were washed in PBS for 10 min two times, permeabilized with permeabilization solution[62] (0.2% Triton X-100, 20% DMSO, and 23 g/L Glycine in PBS) for 30 min at 37°C, blocked in blocking solution (0.2% Triton X-100, 10% DMSO, and 6% normal donkey serum (NDS) in PBS) for 30 min at 37°C. Slices were subsequently incubated in primary antibody solution (1:2000 rabbit anti-FoxP2 (Abcam, ab16046), 5% DMSO, 3% NDS, 0.2% Triton X-100, 10 mg/L Heparin in PBS) for 24 h at 37°C. After washing for 10 min three times with 0.2% Triton X-100 in PBS, sections were incubated for 24 h at 37 °C with a secondary antibody solution (1:500 donkey anti-rabbit Alexa Fluor 647 (Thermo Fisher Scientific), 3% NDS, 0.2% Triton X-100, and 10 mg/L heparin in PBS. After washing at least 30 min three times in PBS, sections were mounted on gelatin-coated glass slides and covered with anti-fade mounting medium and coverslips. Sections were scanned using a laser scanning confocal microscope (LSM700, Carl Zeiss) equipped with a 5x air objective (Plan-Apochromat 5x/0.15NA), a 10x air objective (Plan-Apochromat 10x/0.45NA), 20x air objective (Plan-Apochromat 20x/0.8NA) or 63x oil objective (Plan-Apochromat 63x/1.4NA).

3D reconstruction

For 3D reconstruction, thick coronal sections (3-4 mm) containing all the ITC clusters were prepared with a vibratome (VT1000S, Leica). The sections were then cleared using the CUBIC protocol[63]. A subset of sections was also stained with the FoxP2 antibody. The cleared tissues were imaged with a confocal microscope (Zeiss, LSM700) equipped with a 10x air objective (Zeiss, C Epiplan-Apochromat 10x/0.40NA) or 20x air objective (Zeiss, LD Plan-NEOFLUAR, 20x/0.4NA), which have a relatively long working distance (> 5 mm). The voxel size was 1-3 um * 1-3 um * 10um (x*y*z) to achieve single-cell resolution. Acquired images were imported to Imaris software (Bitplane) and individual ITC clusters were manually reconstructed plane-by-plane with manual contour drawing function in 'Measurement Pro' package. Densely packed regions with marker positive neurons were regarded as clusters. Semi-transparent mouse brain scheme was created using Brainrender[64].

Deep brain calcium imaging

Miniature microscope imaging: Two to six weeks after GRIN lens implantation, mice were head-fixed to check for sufficient expression of GCaMP6 using a miniature microscope[65] (nVista HD, Inscopix). Mice were briefly anesthetized with isoflurane to fix the microscope

baseplate (1050-002192, Inscopix) to the skull using blue light curable glue (Vertise Flow, Kerr). The microscope was removed and the baseplate was capped with a baseplate cover (1050-002193, Inscopix). Mice were habituated to the brief head-fixation on a running wheel for miniature microscope mounting for at least three days before the behavioural paradigm. Imaging data were acquired using nVista HD software (Inscopix) at a frame rate of 20 Hz with an LED power of 10-60% (0.9-1.7 mW at the objective, 475 nm), analogue gain of 1, and with 1080 x 1080 pixels. For individual mice, the same imaging parameters were kept across days. Timestamps of imaging frames and behavioural stimuli were collected for alignment using the Omniplex system (Plexon).

Fear conditioning and extinction paradigm: Two different contexts were used; Context A (extinction context) consisted of a clear cylindrical chamber (diameter: 23 cm) with a smooth floor, placed in a dark-walled sound attenuating chamber under dim light conditions. The chamber was scented and cleaned with 1% acetic acid. Context B (fear conditioning context) contained a clear square chamber (26.1 x 26.1 cm) with an electrical grid floor (Coulbourn Instruments) for footshock delivery, placed in a light-coloured sound attenuating chamber with bright light conditions, and was scented and cleaned with 70% ethanol. A stimulus isolator (ISO-Flex, A.M.P.I.) was used for the delivery of direct current (DC) shock. Both chambers contained overhead speakers for delivery of auditory stimuli, which were generated using a System 3 RP2.1 real time processor and SA1 stereo amplifier with RPvdsEx Software (all Tucker-Davis Technologies). Cameras (Stingray, Allied Vision) for tracking animal behaviour were also equipped in both chambers. Radiant Software (Plexon) was used to generate precise TTL pulses to control behavioural protocols and all the TTL signals including miniscope frame timings were recorded by Plex Control Software (Plexon) to synchronize behavioural protocols, behavioural tracking, and miniscope imaging.

On Day1 (Habituation), the mice were first imaged in their homecage for 10 min, and then placed in context A and exposed to 5 CSs (29 pips, 200 ms, 6-kHz pure tone, repeated at 1 Hz) following a 4-min baseline period. The ITI (inter tone interval) was 30 s. On Day2 (fear conditioning), mice were first imaged in their homecage for 10 min, and then fear conditioned in context B by pairing 5 CSs with an unconditioned stimulus (US; 1-s footshock, 0.65 mA DC; applied 800 ms after termination of the last (29th) pip) with a variable ITI of 60-90 s (after a 2-min baseline period). Animals remained in context B for 1 min after the last CS-US pairing. On Day3 and Day4 (extinction 1 and 2), fear memory was extinguished in context A. After a 4-min baseline period, animals were exposed to 25 CSs (ITI: 30 s). On Day5, extinction memory was assessed with 5 CS presentations (ITI: 30 s) following a 4-min baseline period.

Verification of implant sites (clearing-based, for ITC_{dm}): Upon completion of the behavioural paradigm, mice were lightly anesthetized with isoflurane, head-fixed and 3D-scanned with a 2-photon microscope (Ultima, Bruker) equipped with a Ti:Sapphire laser (Insight X3, Spectra Physics) and a 16x water objective lens (0.8NA, Nikon) or 25x water objective lens (1.05NA, Olympus), through the GRIN lens. After 2-photon microscopy, mice were transcardially perfused (as above). GRIN lenses and head bars were removed and brains were post-fixed in 4% paraformaldehyde overnight at 4°C. Horizontal thick sections (1.5-2.0 mm) containing the imaging site were cut with a vibratome (VT1000S). Sections were cleared and stained against FoxP2 using the CUBIC protocol[63] and the same combination of antibodies as above, and then imaged with a confocal microscope (Zeiss, LSM700) equipped with a 5x air objective (Zeiss, Plan-Apochromat 5x/0.15NA) or 20x air objective (Zeiss, LD Plan-NEOFLUAR, 20x/0.4NA), which have a relatively long working distance. Using blood vessels and fibres as landmarks, a maximum intensity projection of the movie acquired with a miniature microscope, a 3D stack acquired with the 2-photon microscope, and a 3D stack acquired with confocal microscopy were manually matched, and then, the area of the miniature microscope movie

corresponding to FoxP2-positive area between BLA and CeA in the confocal image were assigned as ITC_{dm}. Mice with obvious misplacement of the GRIN lens and with no FoxP2 signal were excluded from the analysis. For cases in which CeA was imaged in the periphery of the FOV, only data from ITC_{dm} and BLA were analysed.

Verification of implant sites (slice-based, for ITC_{vm}): Upon completion of the behavioural paradigm, mice were transcardially perfused (as above). GRIN lenses and head bars were removed, and brains were post-fixed in 4% paraformaldehyde overnight at 4°C. Coronal sections (120 μm) containing the imaging site were cut with a vibratome (VT1000S), immediately mounted on glass slides and coverslipped. To verify the GRIN lens position, sections were imaged with a confocal microscope as described above. Images were matched against a mouse brain atlas[66]. Mice with misplacement of the GRIN lens were excluded from the analysis.

2-photon calcium imaging: In a subset of mice used for miniature microscope experiments, awake head-fixed 2-photon imaging sessions were performed through the same implanted GRIN lenses using a 2-photon microscope (Ultima Investigator, Bruker) equipped with a Ti:Sapphire femtosecond laser (InSightX3, SpectraPhysics) and a 16x/0.8NA objective (N16XLWD-PF, Nikon). GCaMP6f and tdTomato were excited at 920 nm, and signals were filtered with a 517–567 nm band-pass filter and a 573–613 nm band-pass filter, respectively. Care was taken to shield the microscope objective and the photomultipliers from stray light. Images were obtained using Prairie View software (Bruker). Square regions (approximately 800 μm × 800 μm) were imaged at 512 × 512 pixels at 30 Hz with the resonant-galvo mode. Several planes were acquired from each animal. Aversive shocks (1 s, 2.00 mA DC) were generated by a stimulus isolator (ISO-Flex, A.M.P.I.) and applied through a pair of electrodes located on the skin of the face. Timing of shock presentations were synchronized with image acquisition by TTLs generated by the Prairie View software.

Chemogenetic manipulations and behavioural testing

Ligand injections: FoxP2-IRES-Cre mice and Cre-negative littermate controls were injected with a Cre-dependent AAV, as described above, and both groups were administered salvinorin B (SalB) or clozapine-N-oxide (CNO) to control for potential behavioral effects of the compounds per se. To activate KORD, mice were subcutaneously injected with 10 mg/kg SalB (catalogue # 11488; Cayman Chemical Company, Ann Arbor, MI, USA) 20 min before the behavioural testing. SalB was dissolved in DMSO at a 1 µl/g body weight injection volume using a 50 µl Hamilton Syringe (Hamilton Company, Reno, NV, USA). To activate hM3Dq, mice were injected intraperitoneally (i.p.) with 3 mg/kg CNO (catalogue # C0832-5MG; Sigma Aldrich) 30 min before the behavioural testing. CNO was dissolved in 10% DMSO in saline and injected at a volume of 10 µl/g body weight.

Fear conditioning and extinction paradigm: Behavioural tests started at 3.5 to 6 weeks after virus delivery. We did not find systematic relationship between the period between surgery and the effects of KORD both in vivo and ex vivo. Prior to testing, each mouse was handled for 2 min per day for 6 days and habituated to subcutaneous (for KORD) or intraperitoneal (for CNO) saline injections for 3 days. Fear conditioning was conducted in a 30 × 25 × 25 cm operant chamber (Med Associates, Inc., Fairfax, VT USA) with metal walls and a metal rod floor. To provide an additional olfactory cue, the chamber was cleaned between subjects with a 79.5% water/19.5% ethanol/1% vanilla extract solution. Following a 3-min baseline period, 3 pairings (60-90 s ITI) of CS (30 s, 80-dB white noise) and US (2 s 0.6 mA, co-terminating with the CS) were presented, followed by a 120-s stimulus-free period. The Med Associates Freeze Monitor system controlled CS and US presentation. Extinction training was conducted the following day (Day2) in a 27 × 27 × 14 cm operant chamber with transparent walls and a

floor covered with wood chips, cleaned between subjects with a 99% water/1% acetic acid solution and housed in a different room from training. After a 3 min baseline period, either 50 ('full extinction') or 10 ('partial extinction') CSs were presented (5 s ITI)[67]. Extinction memory retrieval was tested the next day (Day3) in the same context as extinction training with 5 CS presentations (5 s inter-CS interval), following a 3-min baseline period.

Post-behaviour examination of virus expression: To examine virus expression at the completion of behavioural tests, mice were terminally overdosed with pentobarbital and transcardially perfused with PBS followed by 4% PFA in PBS. Brains were post-fixed over night at 4°C and subsequently stored in 0.1 M phosphate buffer for 1-2 days at 4°C. Coronal sections (50 μm) were cut with a vibratome (Classic 1000 model, Vibratome, Bannockburn, IL, USA). Brain sections were incubated in 1% sodium borohydride followed by blocking solution (10% normal goat serum (Vector Laboratories) and 2% bovine serum albumin (MP Biomedicals, Santa Ana, CA, USA) in 0.05 M PBS with 0.2% Triton X-100) for 2 h at room temperature (20°C), then incubated at 4°C overnight in a cocktail of primary antibodies: 1) chicken anti-GFP (1:2000 dilution, Abcam cat#13970) to aid visualization of KORD, 2) Living Colors® DsRed Polyclonal Antibody (1:1000 dilution, Clontech Labs cat# 632496) to aid visualization of hM3Dq, and 3) rabbit anti-FoxP2 (1:2000 dilution, Abcam cat#16046) to visualize ITC. The next day, sections were incubated in a cocktail of secondary antibodies: Alexa 488 goat anti-chicken IgG (1:1000 dilution, Abcam cat#150169) and goat anti-rabbit Alexa 555 IgG (1:1000 dilution, Abcam cat# A21428). Sections were mounted and coverslipped with Vectashield HardSet mounting medium with DAPI (Vector Laboratories, Inc., Burlingame, CA, USA). Sections were imaged with an Olympus BX41 microscope (Olympus, Center Valley, PA, USA) and a Zeiss LSM 700 confocal microscope (Carl Zeiss Microscopy, Thornwood, NY, USA).

Images from the 139 Cre+ injected mice were inspected to determine whether virus expression was evident and restricted to the ITC cluster targeted and if so, whether expression was present in one or both hemispheres. Targeting success rates (rounded to the nearest %) were as follows: ITC_{vm}-targeting: 41% (21% bilateral, 20% unilateral); ITC_{dm}-targeting: 35% (17% bilateral, 17% unilateral), dual-cluster targeting: 42% (23% bilateral, 19% unilateral). Mice with absent expression were excluded from the analysis. Mice with unilateral or bilateral expression were combined given analysis of freezing behaviour on retrieval indicated generally similar results, as follows: 1) ITC_{vm} KORD inhibition during extinction training: 41.7 ± 13.1% freezing on extinction retrieval in bilateral Cre+ mice (vs Cre- controls: $P = 0.04$, Student's t-test, N = 4) and 35.2 ± 4.4% in unilateral Cre+ mice (vs Cre- controls: $P = 0.03$, N = 7), 2) ITC_{vm} KORD inhibition during extinction retrieval: 47.2 ± 2.8% freezing on extinction retrieval in bilateral Cre+ mice (vs Cre- controls: $P = 0.01$, N = 6) and 41.7 ± 8.3% in unilateral Cre+ mice (vs Cre- controls: $P = 0.3$, N = 2), 3) ITC_{vm} hM3Dq activation during extinction retrieval: 45.6 ± 8.9% freezing on extinction retrieval in bilateral Cre+ mice (vs Cre- controls: $P = 0.3$, N = 3) and 32.2 ± 7.8% in unilateral Cre+ mice (vs Cre- controls: $P = 0.04$, N = 3), 4) ITC_{dm} KORD inhibition during extinction retrieval: 22.5 ± 7.3% freezing on extinction retrieval in bilateral Cre+ mice (vs Cre- controls: $P = 0.002$, N = 4) and 35.7 ± 5.9% in unilateral Cre+ mice (vs Cre- controls: $P = 0.01$, N = 7), 5) ITC_{dm} hM3Dq activation during extinction retrieval: 51.3 ± 8.5% freezing on extinction retrieval in bilateral Cre+ mice (vs Cre- controls: $P = 0.01$, N = 5) and 31.7 ± 15.0% in unilateral Cre+ mice (vs Cre- controls: $P = 0.8$, N = 2), and 6) dual-cluster KORD inhibition during extinction retrieval: 43.9 ± 7.7% freezing on extinction retrieval in Cre+ mice with both clusters expressing virus bilaterally (vs Cre- controls: $P = 0.02$, N = 6) and 49.3 ± 3.2% in Cre+ mice with both clusters expressing virus in one hemisphere and at least one cluster expressing virus in the other hemisphere (vs Cre- controls: $P = 0.001$, N = 5). To illustrate expression patterns, virus expression in each mouse was overlayed to a corresponding coronal atlas image[66] and expression within each binned 35 µm * 40 µm

segment transformed to a numerical value (expression present =1, absent = 0). Images were then aggregated across mice included in the final behavioural analysis (separately for ITC_{vm}-targeted, ITC_{dm}-targeted and dual-cluster targeted) to generate a population heatmap of expression indicating the fraction of animals exhibiting expression at each binned segment (0: no mice expressed; 1: all mice expressed) (see **Extended Data Fig. 8 and 9**).

Ex vivo electrophysiology

KORD functionality verification and connectivity assays between ITCs: Mice were deeply anaesthetized with 3% isoflurane in oxygen and decapitated. The brain was rapidly extracted and cooled down in ice-cold slicing artificial cerebrospinal fluid (ACSF) containing (in mM): 124 NaCl, 2.7 KCl, 26 NaH_2CO_3, 1.25 NaH_2PO_4, 10 $MgSO_4$, 2 $CaCl_2$, 18 D-Glucose, 4 ascorbic acid, equilibrated with carbogen (95% O_2 / 5% CO_2). Coronal brain slices (320 μm) containing the amygdala were cut in ice-cold slicing ACSF with a sapphire blade (Delaware Diamond Knives) on a vibrating microtome (Microm HM 650 V, Thermo Scientific). Slices were collected in a custom-built interface chamber with recording ACSF containing (in mM): 124 NaCl, 2.7 KCl, 26 NaH_2CO_3, 1.25 NaH_2PO_4, 1.3 $MgSO_4$, 2 $CaCl_2$, 18 D-Glucose, 4 ascorbic acid, equilibrated with carbogen. Slices were recovered at 37°C for 40 min and stored at room temperature. Whole-cell patch-clamp recordings were performed in a submersion chamber under an upright microscope (Olympus BX51WI), where slices were superfused with recording ACSF at 31°C. Recordings were performed using an Axon Instruments Multiclamp 700B amplifier and a Digidata 1440A digitizer (Molecular Devices). Glass micropipettes (6-8 MΩ resistance) were pulled from borosilicate capillaries (ID 0.86 mm, OD 1.5 mm, Science Products, Germany).

For KORD functionality verification the resting membrane potential and spikes were recorded in current-clamp mode with K-Gluconate based internal solution containing (in mM): 130 K-Gluconate, 5 KCl, 4 Mg-ATP, 0.4 Na-GTP, 10 Na2-phosphocreatine, 10 HEPES, 0.6 EGTA (290-295 mOsm, pH 7.2-7.3). Signals were low-pass filtered at 10 kHz and digitized at 20 kHz. Salvinorin B (Tocris Bioscience) was prepared as 1mM stock solution in DMSO, diluted to 100nM in ACSF on the day of recording, and perfused via the bath. Data from ITC_{dm} and ITC_{vm} cells were pooled for analysis.

For connectivity assays between ITC clusters, post synaptic currents were recorded in voltage-clamp configuration with cesium-based internal solution containing (in mM): 115 Cs-methanesulphonate, 20 CsCl, 4 Mg-ATP, 0.4 Na-GTP, 10 Na_2-phosphocreatine, 10 HEPES, 0.6 EGTA (290-295 mOsm, pH 7.2-7.3). Signals were low-pass filtered at 2 kHz (4-pole Bessel) and digitized at 10 kHz. Series resistance was monitored and data rejected if it changed > 25% over the course of an experiment. ChR2 was stimulated with 470 nm light pulses (0.5-1 ms duration) delivered by an LED (CoolLED *p*E) through the microscope's submersion objective (Olympus LUMPlanFL 60x, 1.0 NA). By restricting the light path aperture, illumination was confined to a small spot within the slice (80 μm diameter). Drugs were prepared from frozen stocks, diluted in ACSF and applied via superfusion for pharmacological experiments. Picrotoxin (PTX, 100 μM, Sigma, Germany) was used to block GABAergic transmission, tetrodotoxin (TTX, 1 μM, Biotrend, Germany) was first applied alone, and subsequently together with 4-aminopyridine (4-AP, 100 μM, Tocris Bioscience) to assess monosynapticity of evoked postsynaptic currents[68]. In most experiments with on-cluster stimulation, 20 μM DNQX (Biotrend, Germany) was added to the recording ACSF to block fast glutamatergic transmission.

Connectivity assays from ITCs to BLA: Mice were deeply anaesthetized (ketamine 250 mg/kg and medetomidine 2.5 mg/kg bodyweight, injected intraperitoneally) and transcardially perfused with ice-cold (0-2°C) NMDG-based solution[69,70] (in mM: 2.5 KCl, 1.25 NaH_2PO_4 (1 H_2O), 10 $MgSO_4$ (7 H_2O), 0.5 $CaCl_2$ (2 H_2O), 30 $NaHCO_3$, 20 HEPES, 25 Glucose, 93 NMDG,5

Sodium Ascorbate, 2 Thiourea, 3 Sodium Pyruvate, 93 HCl, oxygenated with 95% O_2/5% CO_2, pH 7.3-4) for 3 min. The brain was rapidly removed from the skull, and coronal brain slices (300 μm) containing ITCs and BLA were prepared in ice-cold NMDG-based solution with a vibrating-blade microtome (HM650V, Microm) equipped with a sapphire blade (Delaware Diamond Knives). For recovery, slices were kept in the dark for 10 min at 33°C in an interface chamber containing the NMDG-based solution and afterwards at room temperature (20-24°C) in Hepes-holding solution (in mM: 20 HEPES, 92 NaCl, 2.5 KCl, 1.25 NaH_2PO_4 (1 H_2O), 2 $MgSO_4$ (7 H_2O), 2 $CaCl_2$ (2 H_2O), 25 Glucose, 30 $NaHCO_3$, 5 Sodium Ascorbate, 2 Thiourea, 3 Sodium Pyruvate, oxygenated with 95% O_2/5% CO_2, pH 7.4) for at least 1 h until recording.

Experiments were performed in a submerged chamber on an upright microscope (BX50WI, Olympus) superfused with oxygenated recording ACSF (in mM: 123 NaCl, 3 KCl, 1.25 NaH_2PO_4 (1 H_2O), 1 $MgCl_2$ (6 H_2O), 2 $CaCl_2$ (2 H_2O), 11 Glucose, 26 $NaHCO_3$, 10 μM CNQX and 10 μM CPP) at a perfusion rate of 4 ml/min at 32°C. $EGFP^+$ ITC clusters and CTB^+ BLA projection neurons were visualized using epifluorescence and a 5x air immersion objective(LMPlanFI 5x/0.15 NA, Olympus) or a 40x water immersion objective (LumPlanFI 40x/0.8 NA, Olympus). Patch electrodes (for BLA, 3-5 MΩ; for ITCs, 7-8 MΩ;) were pulled from borosilicate glass tubing and filled with internal solution (for voltage-clamp recordings in mM: 110 CsCl, 30 K-gluconate, 1.1 EGTA, 10 HEPES, 0.1 $CaCl_2$, 4 Mg-ATP, 0.3 Na-GTP, 4 QX-314 chloride, pH 7.3; for current-clamp recordings in mM: 130 K-methylsulfate, 10 HEPES, 10 Na-phosphocreatine, 4 Mg-ATP, 0.3 Na-GTP, 5 KCl, 0.6 EGTA, pH 7.3). In some experiments, 0.4% biocytin was added to post-hoc visualize recorded neurons. Voltage-clamp recordings from BLA neurons were acquired in whole-cell mode at a holding potential of -70 mV. soCoChR expressing ITC_{dm} and ITC_{vm} were photostimulated using blue LEDs (PlexBright Blue, 465 nm, with LED-driver LD-1, Plexon) connected to optical fibres (0.39NA, FT200EMT, Thorlabs) positioned above them. Five blue light pulses of 0.6 mW (at the fibre-tip) with 10-ms duration were applied at a frequency of 0.5 Hz. Inhibitory postsynaptic currents were averaged across at least 10 light pulses. In some slices, PTX (100 μM) was administered with the recording ACSF for the last cell recorded from. In current-clamp recordings from ITCs, spikes were evoked from a holding potential of about -70 mV with the same blue light stimulation protocol as above. Data was acquired with a Multiclamp 700B amplifier, Digidata 1440A A/D converter and pClamp 10 software (all Molecular Devices) at 20 kHz and filtered at 10 kHz. Data were excluded if the access resistance exceeded 25 MΩ or 10% of the membrane resistance or changed more than 20% during the recordings. All chemicals were purchased from Sigma-Aldrich except for CNQX, CPP and QX-314 (Tocris Bioscience).

Post-hoc histological analysis for connectivity assays between ITCs: Following recordings, slices were sandwiched between two cellulose nitrate filter papers (0.45 μm pore size, Sartorius, Germany) and fixed in 4% PFA in 0.1 M phosphate buffered saline (PBS, pH 7.4) overnight. To confirm cluster-specific ChR2- EYFP expression, fixed slices were re-sectioned at 60 μm thickness with a vibrating microtome (Microm HM 650 V, Thermo Scientific). Free floating sections were incubated in blocking solution (20% horse serum, 0.03% Triton X-100 in PBS) for 2 h at room temperature, and then overnight in PBS with 10% blocking solution and primary antibodies at a 1:1000 dilution; in all cases against EYFP fused to channelrhodopsin2 (Goat- anti-GFP polyclonal), in some batches also against FoxP2 (Rabbit-anti-FoxP2 polyclonal). On the next day, sections were washed 3 times for 10 min in PBS, and incubated for 2 h at room temperature in PBS with 10% blocking solution and secondary antibodies at 1:1000 dilution; in all cases with Donkey-anti-goat-Alexa488, for FoxP2 staining additionally with Donkey-anti-rabbit-Alexa555. Slices were then washed 3 times for 10 minutes in PBS, incubated for 25 min in 1:500 Neurotrace 435/455 in PBS, and washed 3 more times for 10 minutes in PBS. Sections were then mounted on glass slides in mounting medium (Vectashield, Vector Laboratories) and imaged with a confocal microscope (LSM 710, Zeiss).

Fibre photometry recording

A modified Doric Fibre Photometry system was used to perform the recordings. Three different excitation wavelengths were used (465 nm for Ca^{2+}-dependent jGCaMP7f activity, 560 nm for Ca^{2+}-dependent jRGECO1a activity, and 405 nm to record an isosbestic, Ca^{2+}-independent, reference signal that serves to correct for photo-bleaching and movement-related artifacts[71]. The light intensity used for each wavelength was < 100 μW at the fibre tip. Optical patch cables were extensively photo-bleached before recordings to reduce auto-fluorescence and a lock-in modulation/demodulation procedure was used to improve the signal-to-noise ratio and spectral separation of the fluorescent signals[72]. Data were digitized and recorded at 20 kHz.

Elevated zero maze paradigm: The elevated zero maze with a 55 diameter and a 5 cm width corridor was composed of two open and two closed quadrants, which are equivalent to 90° each, elevated at 50 cm above the ground. Two external walls and two internal walls with 15 cm height for the closed quadrants were made of opaque plastic and transparent plexiglass, respectively. Mice were allowed to freely explore the maze for 15 min. Mouse behaviours were video recorded with a camera controlled with a custom written code in Bonsai[73], while synchronized with photometry recording via TTL pulses. The videos were post-hoc analysed by a second custom written code in Bonsai and the position of the mouse in the open versus closed quadrants determined as the central position of the body mass.

Quantification and statistical analysis

Analysis of behaviour during calcium imaging: All behavioural sessions were recorded using an overhead camera (Stingray, Allied Vision) and Cineplex software (Plexon) at 40 Hz. Mice were tracked using contour tracking, and freezing behaviour was automatically scored with the assistance of a frame-by-frame analysis of pixel change (Cineplex Editor, Plexon). Freezing behaviour minimum duration threshold was set to 2 s. Automatically detected freezing epochs were manually inspected on the video recording to eliminate false-positive and false-negative freezing bouts (e.g., during micro-grooming episodes or due to motion artefacts caused by cable movement, respectively). Annotated freezing data were then temporally aligned with miniscope imaged data and finally downsampled to 10 Hz.

Analysis of behaviour for chemogenetic manipulation: Behavioural sessions were video recorded with The Med Associates Freeze Monitor system (fear conditioning) or with GoPro HERO7 video camera (extinction training and retrieval). Based on the recorded videos, freezing was manually scored at 5 s intervals throughout testing by an experienced observer blind to genotype. The mean numbers of freezing observations per baseline period and 5x CS blocks were converted to a percentage [(number of freezing observations/total number of observations per period) × 100] for analysis. Mice with freezing scores on any CS-block >3 standard deviations from the group mean were excluded from the analysis.

Analysis of miniature microscope calcium imaging data: Imaging frames were down-sampled to 540 × 540 pixels at 10 Hz and normalized across the whole frame by dividing each frame by a Fast Fourier Transform band pass-filtered version of the frame using ImageJ (NIH)[28]. Motion artifact correction and PCA/ICA-based cell detection was performed with MosaicAPI (Inscopix) for MATLAB. Edges of cell masks were then smoothed by open/close functions. Raw calcium traces were obtained by averaging all the pixel values in each mask. Slow drift of the baseline signal over the course of minutes was removed using a low-cut filter (Gaussian, cutoff, 2 – 4 min). Relative changes in calcium fluorescence F were calculated by $\Delta F/F0 = (F - F0)/F0$ (with F0 = median fluorescence of entire trace). When a cell pair showed (1) distance between centroids < 15 pixels (2) correlation coefficient between entire time courses > 0.6, one of the pair was manually eliminated to avoid double-counting. Finally, pairs of the mask

and the trace of all the cells were manually inspected to exclude false-positive/negative cell mask allocation. For fear extinction, images from consecutive 5 days were concatenated before the motion correction procedure. When there was major displacement of the field of view (FOV) and same set of neurons were not able to be identified across days, animals were excluded.

To define responsive cells, trial-averaged Ca^{2+} signals were compared between the stimulus and temporally-equivalent baseline period using a Wilcoxon rank-sum test with a significance threshold of $P < 0.05$. The windows for averaging were 2 s (shock), 4 s (CS-offset), and 29 s (CS), from stimulus-onset. AUC (area under the curve) ΔF/F values were calculated using these same windows. A cell was classified as a fear neuron if it exhibited a significant tone response after fear conditioning (CS 1-5 during Ext1 (Day3), when freezing levels were highest), but no significant response after extinction (CS 21-25 during Ext2 (Day4), when freezing levels were lowest), and vice versa for extinction neurons. Finally, units were classified as extinction-resistant neurons if they displayed a significant tone response during both time points.

Analysis of 2-photon calcium imaging data: The images were analysed by using custom written in-house software running on MATLAB (Mathworks). First, acquired images were motion corrected with NoRMCorre[74]. Artifacts caused by bi-directional scanning were corrected by shifting odd lines and even lines. Cell outlines were manually identified using ROI-manager function in ImageJ, based on motion corrected movies and maximum intensity projections. Time courses of individual cells were extracted by summing the pixel values within the cell outlines. Slow drift of the baseline signal over the course of minutes was removed using a low-cut filter (Gaussian, cutoff, 2–4 min). Raw calcium signal time courses were corrected to minimize out-of-focus signal contamination: neuropil signals were subtracted from cell body signals after multiplying by a fixed contamination ratio: 0.7 as previously described[75,76].

Analysis of fibre photometry recordings: Analysis was performed with custom programs written in MATLAB (Mathworks). Data with obvious motion artifacts in the isosbestic channel were discarded. De-modulated raw Ca^{2+} traces were down-sampled to 1 kHz and then de-trended using a low-cut filter (Gaussian, cutoff, 2-4 min) to correct for slow drift of the baseline signal due to bleaching. Filtered traces were Z-scored by mean and standard error of the entire trace.

Analysis of slice whole-cell recordings: Data were analysed with custom written codes in Python 3.7 (Anaconda distribution) running the pyABF module, custom written Macros in IgorPro (Wavemetrics, USA), or custom programs written in MATLAB (Mathworks) using abfload (Harald Hentschke/Forrest Collman) function. Connectivity was defined by comparing signal vs baseline (10 trials), while statistical significance was assessed by Wilcoxon signed-rank test.

Statistical analyses and data presentation

All data are expressed as the mean ± standard error of the mean (SEM), unless stated otherwise. Two-sided Wilcoxon rank-sum test was used to compare two independent groups. For paired comparison, we used Wilcoxon signed-rank test or paired-t test based on distribution and n size of the data. An ANOVA was performed when more than two groups were compared, which was followed by Tukey-Kramer post-hoc method. For multiple comparisons against a baseline, Dunnett's test was used. For comparing 2 distributions, Kolmogorov Smirnov test was applied. For trend, Jonckheere-Terpstra test was used. For categorical data, Chi-squared test or Fisher's exact test (when sample sizes and expected frequencies are small) was applied. For repeated observations of freezing scores, a repeated

measures ANOVA was used, which was followed by Sidak post-hoc method. All data analyzed by ANOVA were normally distributed according to a Kolmogorov-Smirnov test on the ANOVA residuals. Throughout the study, $P < 0.05$ was considered statistically significant. No statistical methods were used to pre-determine sample sizes, but our sample sizes are similar to those generally employed in the field.

Data availability

The data that supports the findings of this study will be available at: https://data.fmi.ch/PublicationSupplementRepo/

Code availability

Custom-written codes used to analyse data from this study are available upon reasonable request from the corresponding authors.

Hagihara et al. Fig. 1

Single Column

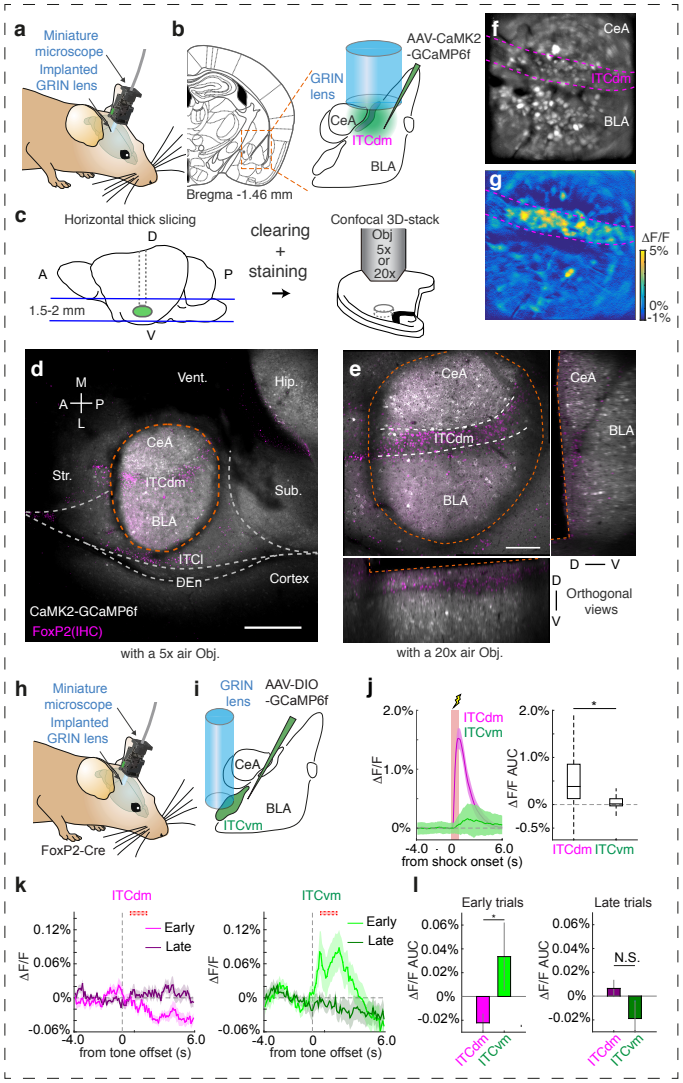

Fig. 1 | ITC clusters differentially signal the presence and absence of an aversive stimulus.
a, Schematic showing endoscopic imaging with a miniaturized microscope in a freely moving mouse.
b, Prior to GRIN lens implantation, an AAV encoding CaMK2-GCaMP6f was injected targeting CeA, BLA and the ITC_{dm} cluster. A GRIN lens was then implanted above the injection site.
c, Schematic showing post-hoc identification of ITC_{dm} neurons. *Left:* Following *in-vivo* calcium imaging experiments, mice were sacrificed and horizontal sections containing imaged FOVs with 1.5-2.0 mm thickness were cut. The slices were cleared using the CUBIC protocol and stained with anti-FoxP2 antibody. *Right:* Cleared and stained slices were imaged using a confocal microscope. Gray lines indicate position of implanted GRIN lens.
d, Example confocal image of cleared and stained tissue acquired with a 5x objective (obtained from the same mouse shown in **f,g**). Orange dotted line indicates outline of GRIN lens implanted area. Scale bar: 500 μm. Str.: Striatum; Vent.: Ventricle; DEn: Dorsal endopiriform nucleus; Hip.: Hippocampus; Sub.: Subiculum
e, Same sample as shown in **d**, acquired with a 20x objective. XZ and YZ orthogonal views were visualized in an isotropic manner. Scale bar: 250 μm. See also **Supplementary Movie 2**.
f, Maximum-intensity projection image of BLA, CeA, and ITC_{dm} neurons acquired with a miniature microscope. Dashed magenta lines indicate the FoxP2-positive area shown in **f** with dashed white lines, which was identified as ITC_{dm} cluster. The image approximately corresponds to 600 µm × 600 µm.
g, A ΔF/F map showing clustered ITC_{dm} activation. See also **Supplementary Movie 3**.
h, Schematic showing miniature microscope imaging in a freely moving mouse.
i, Prior to GRIN lens implantation, an AAV encoding CAG-DIO-GCaMP6f was injected targeting the ITC_{vm} cluster. A GRIN lens was then implanted above the injection site.
j, *Left:* Averaged Ca^{2+} responses to footshocks of all the recorded ITC_{dm} neurons (magenta, n = 271 neurons, from 9 mice) and ITC_{vm} neurons (green, n = 372 neurons, from 6 mice). Red shading indicates footshock US presentations (1s). *Right:* Averaged ΔF/F values. * $P = 2.1 \times 10^{-32}$, Wilcoxon rank-sum test.
k, Trial-averaged ΔF/F Ca^{2+} time course of all the ITC_{dm} (left) or ITC_{vm} (right) neurons in response to footshock US omissions on the first 5 and the last 5 trials. Dotted red boxes indicate the expected timing of US delivery.
l, Averaged ΔF/F responses to US omissions on the first (left) and the last 5 trials.
* $P = 0.0039$, N.S.: $P = 0.98$, Wilcoxon rank-sum test.
Data shown in **j-l** were obtained from the same animals as shown in **Fig. 2**.

Hagihara et al. Fig. 2

Single Column

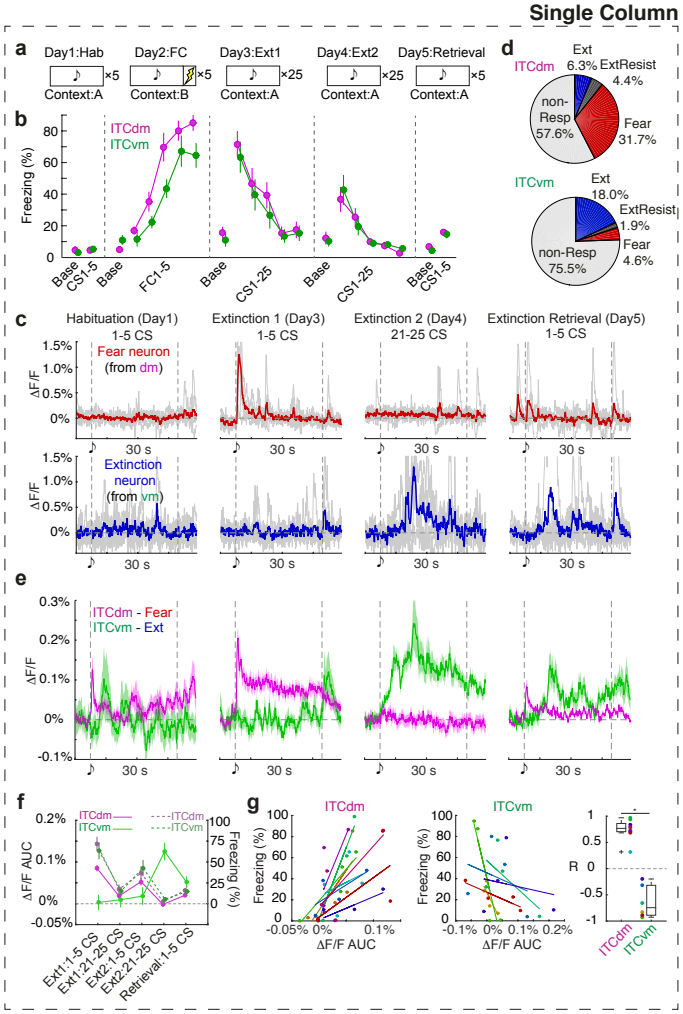

Fig. 2 l CS responses of ITC clusters parallel the switch from high to low fear state.
a, 5-day fear conditioning and extinction paradigm.
b, Freezing behaviour values from ITC_{dm} targeted (magenta, N = 9) and ITC_{vm} targeted (green, N = 6) mice.
ITCdm: FC1-5: $P = 4.7*10^{-9}$ (ascend); Ext1 CS1-25: $P = 4.2*10^{-7}$ (descend); Ext2 CS1-25: $P = 1.9*10^{-9}$ (descend); ITCvm: FC1-5: $P = 1.8*10^{-7}$ (ascend); Ext1 CS1-25: $P = 3.9*10^{-5}$ (descend); Ext2 CS1-25: $P = 7.5*10^{-6}$ (descend); Jonckheere-Terpstra test for trend.
c, Representative Ca^{2+} traces of fear and extinction neurons from ITC_{dm} and ITC_{vm}, respectively. 5-trial averaged traces are shown in colour and traces from individual trials are shown in gray.
d, Fractions of Fear, Extinction, and Extinction Resistant neurons in the ITC_{dm} (n = 271 neurons, from 9 animals) and ITC_{vm} (n = 372 neurons, from 6 animals) clusters. $P = 6.3 \times 10^{-20}$, Chi-squared test. Fear neurons: $P < 0.01$; Extinction neurons: $P < 0.01$; Extinction Resistant neurons: $P > 0.10$.
e, Averaged Ca^{2+} responses to tone CSs of ITC_{dm} fear neurons (magenta, n = 86) and ITC_{vm} extinction neurons (green, n = 67). Vertical dotted lines indicate onsets and offsets of CSs. For responses in the entire recorded population, which includes the same task phase-classified neurons shown here, aligned and baseline-normalized to tone-offset, see **Fig. 1k**.
f, Averaged ΔF/F values (solid lines) and averaged freezing behaviour (dotted lines) from ITC_{dm} and ITC_{vm} targeted animals during each of the 5 stages of extinction training and retrieval.
g, Relationships between 5-trial averaged ΔF/F values (as in panel **f**) and corresponding freezing behaviour during each of the 5 stages of extinction training and retrieval, for ITC_{dm} fear neurons (*Left*) and ITC_{vm} extinction neurons (*Center*). Data points (5 points per animal, 1 per testing stage) and lines (fitted with linear regression) are colour-coded by individual animal (ITC_{dm}: N = 9; ITC_{vm}: N = 6). R (correlation coefficient) values of the fitted lines are plotted (*Right*); dots are coloured as in the left panels. * $P = 4.0 \times 10–4$, Wilcoxon rank-sum test.

Hagihara et al. Fig. 3

Double Column

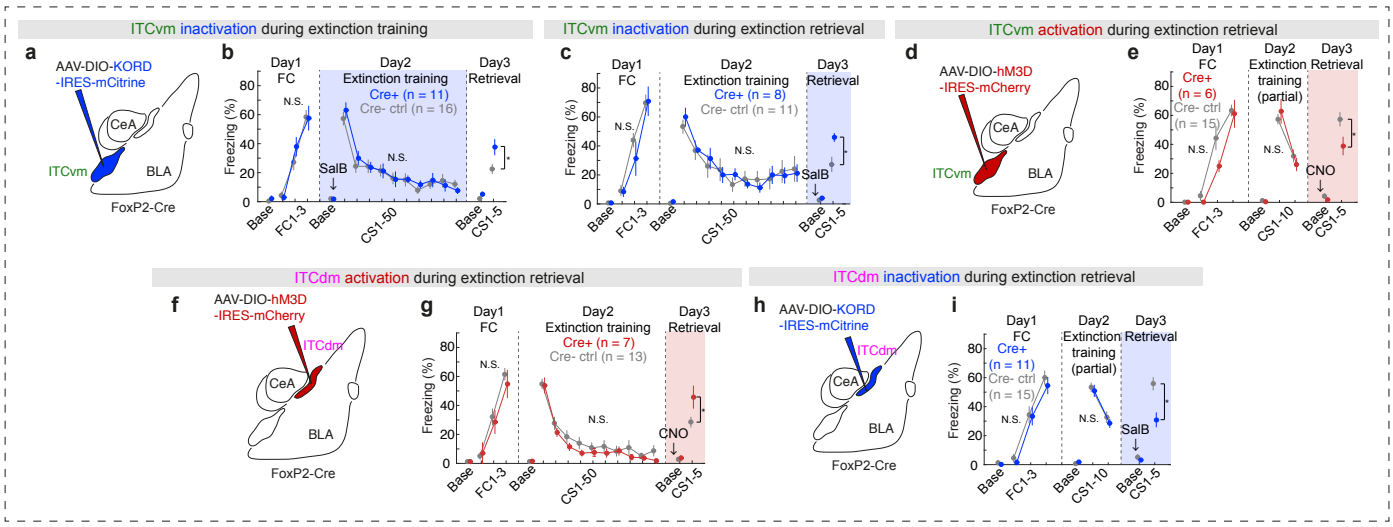

Fig. 3 | ITC clusters differentially and bidirectionally regulate fear extinction.
a, Schematic showing chemogenetic manipulation experiments. An AAV encoding Cre-dependent KORD was targeted to ITC_{vm} neurons in FoxP2-Cre mice.
b,c, Freezing behaviour of experimental (Cre+) and control (Cre-) mice; for all chemogenetic experiments, controls were injected with the AAV and administered with the ligand. Arrows and colour-shadings indicate the timing of SalB administration relative to full (50-trial) extinction training (**b**) or retrieval (**c**). Freezing levels on extinction retrieval (Day3) in **b**: Cre+: 37.6 ± 5.2%; Cre-: 22.5 ± 3.1%; * $P = 0.0013$; in **c**: Cre+: 45.8 ± 2.7%; Cre-: 27.3 ± 4.9%; * $P = 0.0005$, repeated measures ANOVA followed by Sidak post-hoc test.
d, An AAV encoding Cre-dependent hM3Dq was targeted to ITC_{vm} neurons in FoxP2-Cre mice.
e, Freezing behaviour of experimental (Cre+) and control (Cre-) mice. Arrow and colour-shading indicate the timing of CNO administration prior to partial (10-trial) extinction retrieval. Freezing levels on extinction retrieval (Day3): Cre+: 38.9 ± 6.1%; Cre-: 57.3 ± 4.6%; *$P = 0.0079$
f, An AAV encoding Cre-dependent hM3Dq was targeted to ITC_{dm} neurons in FoxP2-Cre mice. Arrow and colour-shading indicate the timing of CNO administration prior to full (50-trial) extinction retrieval.
g, Freezing levels on extinction retrieval (Day3): Cre+: 45.7 ± 7.6%; Cre-: 28.5 ± 3.3%; * $P = 0.0044$
h, An AAV encoding Cre-dependent KORD was targeted to ITC_{dm} neurons in FoxP2-Cre mice.
i, Freezing behaviour of experimental (Cre+) and control (Cre-) mice. Arrow and colour-shading indicate the timing of SalB administration prior to partial (10-trial) extinction retrieval. Freezing levels on extinction retrieval (Day3): Cre+: 30.9 ± 4.8%; Cre-: 55.8 ± 4.2%; * $P < 0.0001$
N.S.: not significant. We did not observe significant differences on Day1, Day2 and in baseline on Day3. For histological verification of virus expression and success rates of AAV targeting to specific ITC clusters, see **Extended Data Fig. 8** and **Methods.**

Hagihara et al. Fig. 4

Single Column

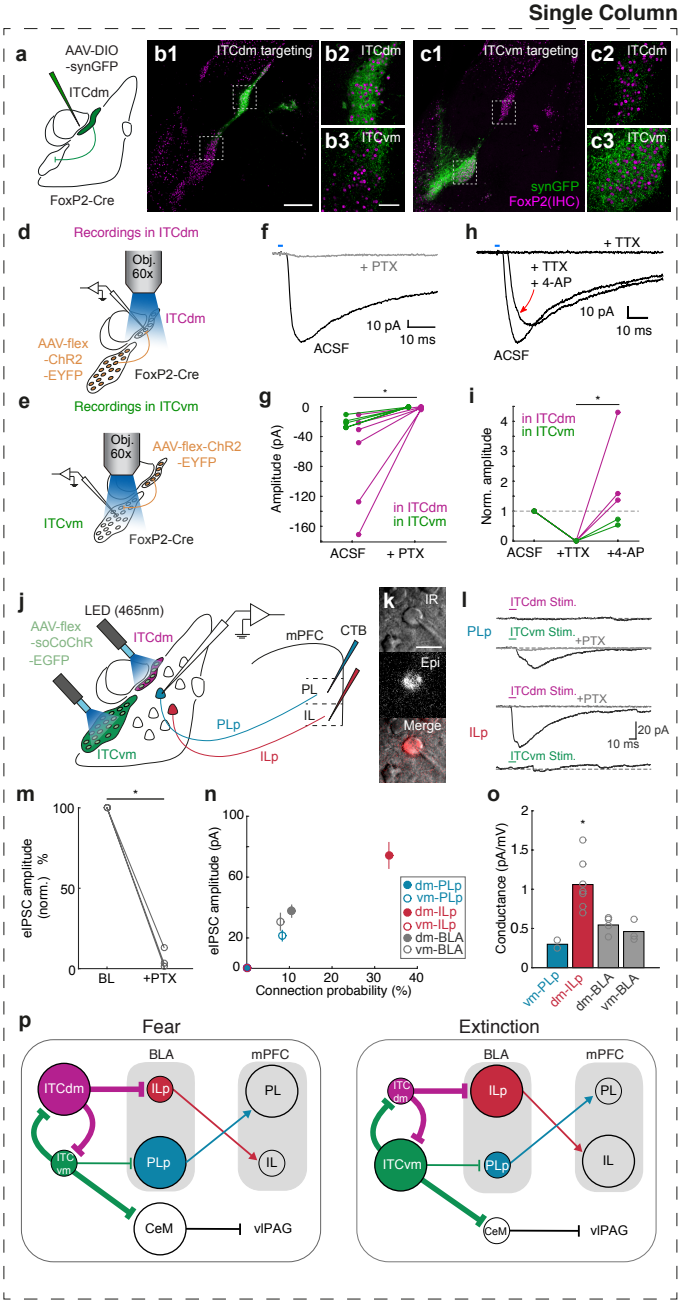

Fig. 4 | ITC clusters exert reciprocal inhibition and selective control over amygdala outputs regulating extinction.

a, Schematic showing inter-cluster virus-based tracing experiments (ITC_{dm}-targeted example shown, same strategy used for ITC_{vm}-targeting). An AAV encoding Cre-dependent synaptophysin-GFP was targeted to ITC_{dm} or ITC_{vm} neurons in FoxP2-Cre mice.

b,c, Confocal images from ITC_{dm} (**b**) or ITC_{vm} (**c**) injected animals. FoxP2 expression was visualized using immunohistochemistry (IHC). Injections were repeated in 5 animals for ITC_{dm} and 4 animals for ITC_{vm}. Scale bars: 500 μm (**b1**, same for **c1**); 200 μm (**b3**, same for **b2**, **c2**, **c3**).

d,e, Schematic showing inter-cluster *ex vivo* slice electrophysiology experiments. An AAV encoding Cre-dependent ChR2-EYFP was targeted to ITC_{vm} (**d**) or ITC_{dm} (**e**) neurons in FoxP2-Cre mice. Recordings were performed in the other ITC cluster while photostimulating incoming axons expressing ChR2-EYFP.

f, Example IPSC (at -70mV holding potential) evoked by photostimulation of ChR2-EYFP-expressing axons. Picrotoxin (PTX) abolished IPSCs, demonstrating $GABA_A$ receptor dependency.

g, Summary of PTX experiments. Magenta lines represent $ITC_{vm} \rightarrow ITC_{dm}$ connections (n = 6 neurons from 6 mice); green lines represent $ITC_{dm} \rightarrow ITC_{vm}$ connections (n = 5 neurons from 4 mice). * P = 0.011, paired-t test.

h, Example IPSC (at -70mV holding potential) evoked by photostimulation of ChR2-expressing axons. Mono-synaptic IPSCs were isolated by subsequent application of Tetrodotoxin (TTX) and TTX + 4-Aminopyridine (4-AP).

i, Summary of TTX + 4-AP application experiments ($ITC_{vm} \rightarrow ITC_{dm}$: n = 3 neurons from 3 mice, $ITC_{dm} \rightarrow ITC_{vm}$: n = 2 neurons from 2 mice). * P = 0.029, one-way ANOVA followed by Tukey-Kramer.

j, Schematic showing long-range circuit *ex vivo* slice electrophysiology experiments. ITC_{dm} and ITC_{vm} neurons were targeted with an AAV encoding Cre-dependent soCoChR in FoxP2-Cre mice. Two optical fibres for photostimulation were placed above the ITC clusters. PL- and IL-projecting BLA neurons were retrogradely labelled with CTB injections into the PL or IL.

k, Example images of a CTB-positive BLA neuron under the microscope for slice recordings. Scale bar: 20 μm.

l, Example IPSCs recorded from PL- (PLp) and IL-projecting (ILp) BLA neurons (at -70mV holding potential) evoked by selective photostimulation of soCoChR-expressing ITC clusters. Picrotoxin (PTX) application completely blocked IPSCs, demonstrating $GABA_A$ receptor dependency.

m, Mean normalized evoked IPSC before and after PTX application (ITCdm→ILp, ITCvm→PLp, ITCvm→ unidentified, total: n = 3 neurons from 3 mice). * P = 0.030, paired-t test. BL: Baseline.

n, Connection probability and mean evoked IPSC amplitudes from the two ITC clusters to PL- or IL-projecting BLA neurons and unidentified (CTB-) BLA neurons (PLp: PL-projecting, n = 24 neurons; ILp: IL-projecting, n = 21 neurons; BLA: unidentified, n = 38 neurons). Note, dm-PLp and vm-ILp connections were not observed, and thus, their data points are superimposed at **0**.

o, Synaptic conductance of evoked IPSCs from connected neurons. Slopes were calculated from IPSC amplitudes acquired at three different holding potentials (–60, –70, and –80mV). * P = 0.0028, one-way ANOVA followed by Tukey-Kramer.

p, Schematic illustrating state-dependent functional changes in amygdala circuitry regulated by ITC clusters. Size of nodes indicates activity levels and width of connections represent putative functional connection strength.

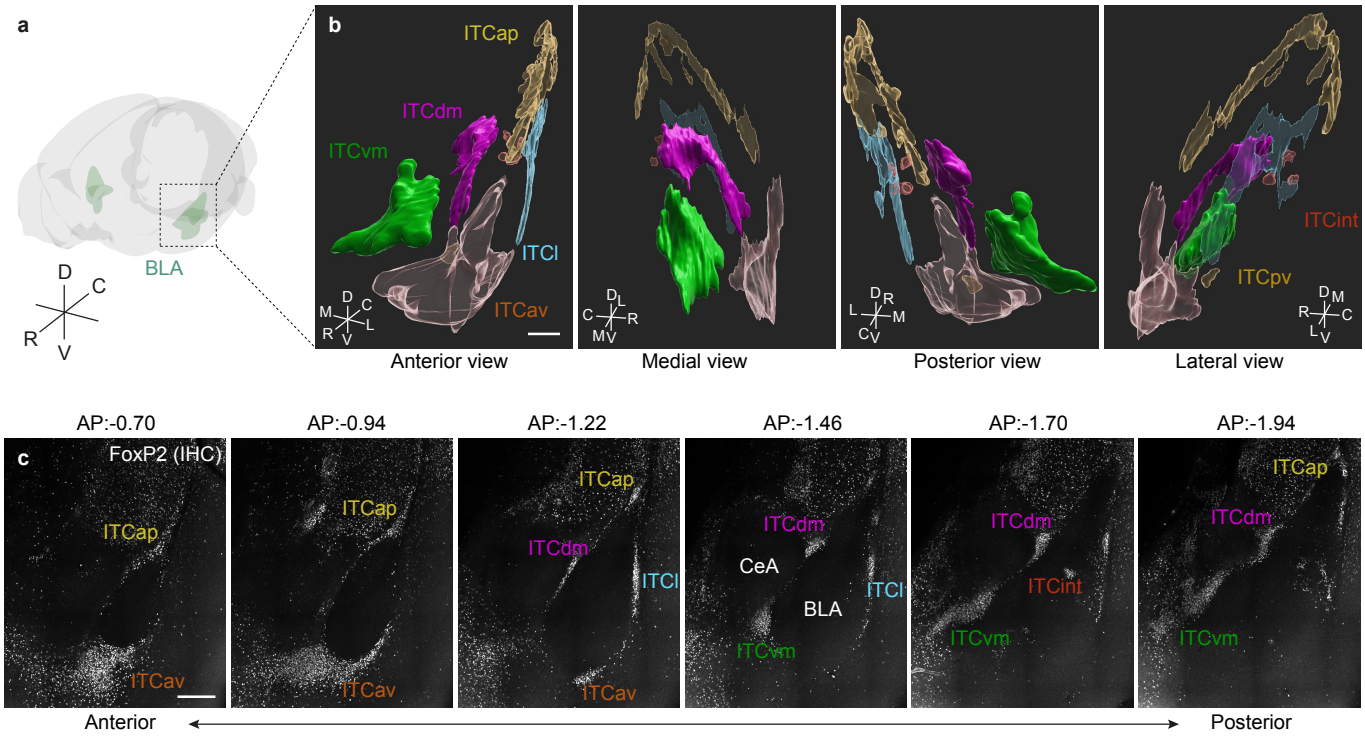
a
BLA
D
C
R
V
b
ITCap
ITCdm
ITCvm
ITCl
ITCav
ITCint
ITCpv
Anterior view
Medial view
Posterior view
Lateral view
AP:-0.70
AP:-0.94
AP:-1.22
AP:-1.46
AP:-1.70
AP:-1.94
c
FoxP2 (IHC)
CeA
BLA
Anterior
Posterior

Extended Data Fig. 1 | 3D-reconstruction of individual ITC clusters

a, Schematic of a mouse brain volume. R: Rostral; C: Caudal; D: Dorsal; V: Ventral.

b, 3D reconstructions were separately obtained via 1) anti-FoxP2 immunostaining, 2) a FoxP2-Cre x Ai14 mouse, and 3) D1R-Cre x Ai14 mouse, in triplicate for each method. ITC_{ap}: apical; ITC_{dm}: dorsomedial; ITC_{vm}: ventromedial; ITC_{l}: lateral; ITC_{av}: anteroventral; ITC_{int}: internal; ITC_{pv}: posteroventral

R: Rostral; C: Caudal; D: Dorsal; V: Ventral; M: Medial; L: Lateral; Scale bar: 300 µm.

c, Example planes of a cleared 3D-tissue obtained from a WT mouse stained with an anti-FoxP2 antibody covering the anterior-posterior axis of ITC clusters. Bregma levels are indicated above each panel. Scale bar: 300 µm.

See also **Supplementary Movie 1** and **Table 1**.

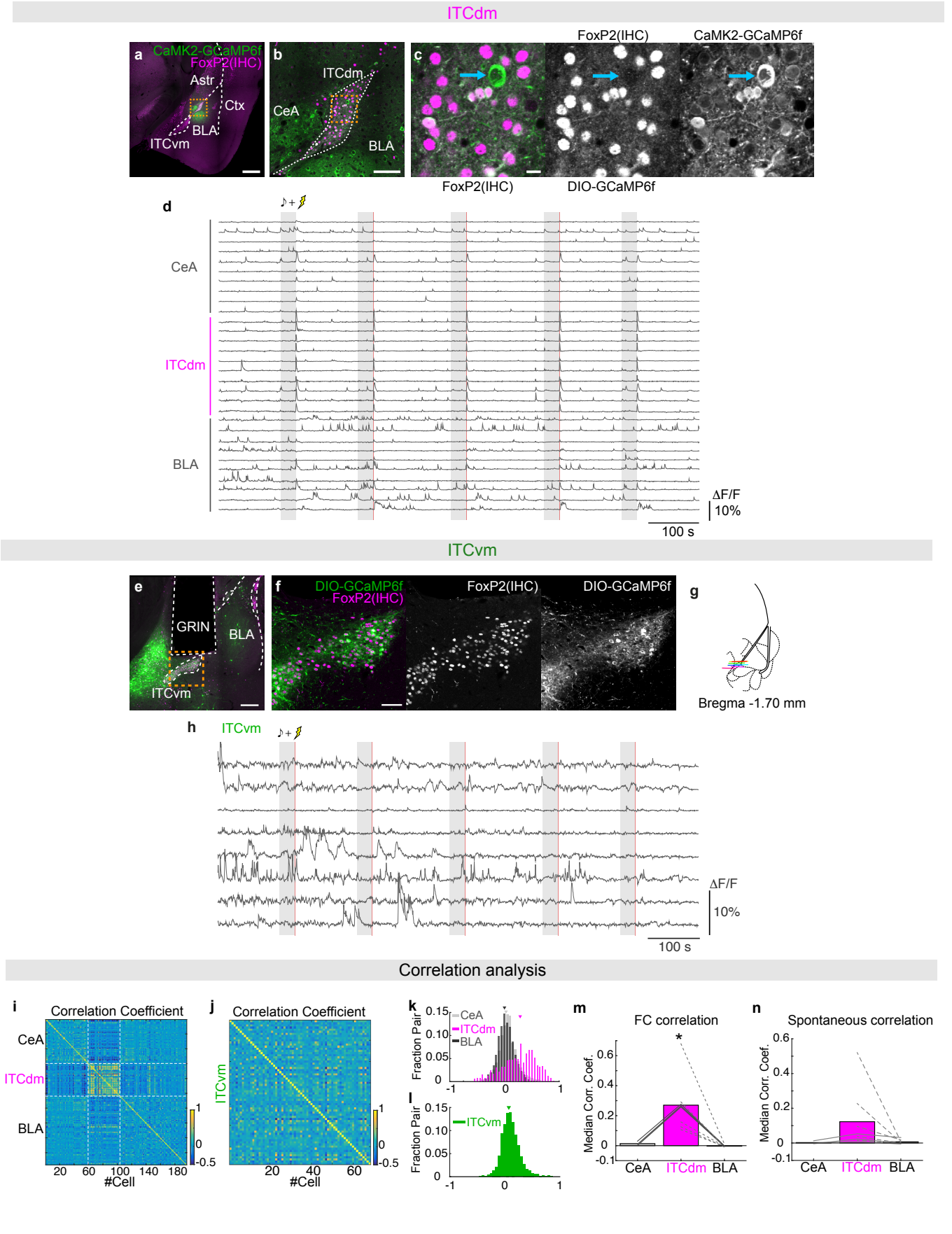
ITCdm
a
CaMK2-GCaMP6f
FoxP2(IHC)
Astr
Ctx
BLA
ITCvm
b
ITCdm
CeA
BLA
c
FoxP2(IHC)
CaMK2-GCaMP6f
FoxP2(IHC)
DIO-GCaMP6f
d
CeA
ITCdm
BLA
ΔF/F
10%
100 s
ITCvm
e
GRIN
BLA
ITCvm
f
DIO-GCaMP6f
FoxP2(IHC)
FoxP2(IHC)
DIO-GCaMP6f
g
Bregma -1.70 mm
h
ITCvm
ΔF/F
10%
100 s
Correlation analysis
i
Correlation Coefficient
CeA
ITCdm
BLA
20 60 100 140 180
#Cell
1
0
-0.5
j
Correlation Coefficient
ITCvm
20 40 60
#Cell
1
0
-0.5
k
Fraction Pair
0.15
0.10
0.05
0
CeA
ITCdm
BLA
-1 0 1
l
Fraction Pair
0.15
0.10
0.05
0
ITCvm
-1 0 1
m
FC correlation
*
Median Corr. Coef.
0.6
0.4
0.2
0
-0.1
CeA ITCdm BLA
n
Spontaneous correlation
Median Corr. Coef.
0.6
0.4
0.2
0
-0.1
CeA ITCdm BLA

Extended Data Fig. 2 | Ca^{2+} imaging from ITC_{dm} and ITC_{vm}.

a-c, Histological validation of GCaMP6f expression. Wild-type mice (not used for *in vivo* imaging) (N = 2) were injected with an AAV-CaMK2-GCaMP6f and sacrificed after 1 month of expression. Thin slices (120 μm) were cut and stained with an anti-FoxP2 antibody. In addition to BLA and CeA neurons, most of the FoxP2-positive ITC_{dm} neurons expressed GCaMP6f. Blue arrow shows a putative large, FoxP2-negative ITC neuron. Scale bars: 500 μm (**a**), 100 μm (**b**), and 10 μm (**c**).

d, Example Ca^{2+} traces from simultaneously imaged neurons in the CeA, ITC_{dm}, and BLA with a miniature microscope during fear conditioning. Data obtained from the same mice as shown in **Fig. 1d-g**. Gray shading indicates CS presentation (30 s); red line indicates footshock US presentations (1 s).

e,f, Histological validation of GCaMP6f expression in ITC_{vm} neurons. FoxP2-Cre mice were injected with an AAV encoding Cre-dependent GCaMP6f, implanted with a GRIN lens, and sacrificed after behavioural experiments. Thin slices (120 μm) were cut and stained with an anti-FoxP2 antibody. Scale bars: 200 μm (**e**), 50 μm (**f**).

g, Summary of histologically confirmed GRIN lens implantation locations for ITC_{vm} recordings. Animals with off-target implantations were excluded from analysis.

h, Example Ca^{2+} traces from neurons in the ITC_{vm} cluster during fear conditioning. Gray shading indicates CS presentation (30 s); red line indicates footshock US presentations (1s). Images of GCaMP6f expression from the same mouse are shown in panel **e,f**.

i,j, Correlation matrices of all simultaneously-recorded neuron pairs in CeA, ITC_{dm}, and BLA (**i**), or in ITC_{vm} (**j**) from representative animals. The entire recording session (11 min) was used.

k, Distributions of correlation coefficients from CeA/CeA, ITC_{dm}/ITC_{dm}, and BLA/BLA pairs. Arrows indicate median of the distributions.

l, Distribution of correlation coefficients from ITC_{vm}/ITC_{vm} pairs. Arrow indicates median of the distribution.

m, Summary of medians of correlation coefficient distribution shown in **(k)**. Solid lines indicate individual animals in which CeA, the ITC_{dm} cluster, and BLA were simultaneously imaged (N = 3). Dotted lines indicate animals in which only the ITC_{dm} cluster and BLA were simultaneously imaged (N = 5). * P = 0.007, one-way ANOVA followed by Tukey-Kramer.

n, Medians of correlation coefficient distribution. The same analysis as **(m)** was applied to data from home-cage recording sessions. ITC_{dm} neurons also shows a trend towards a higher correlation in the absence of CS or US stimulation. * P = 0.12, one-way ANOVA.

ITCdm 2-photon imaging

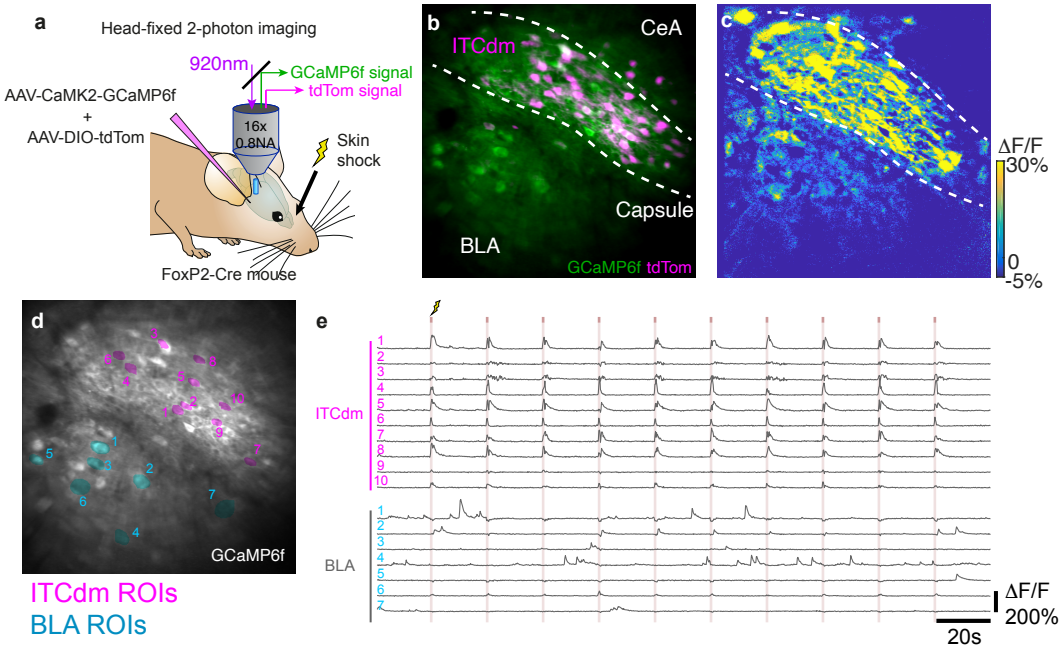

ITCdm and ITCvm photometry

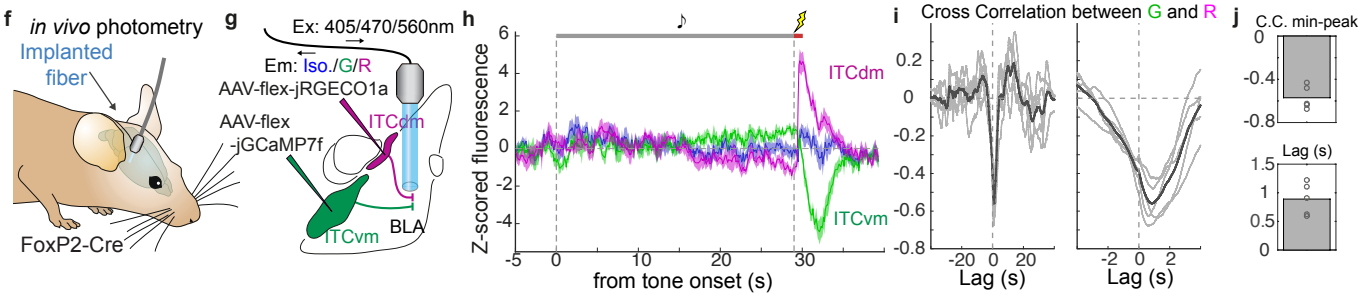

Shock omission responses

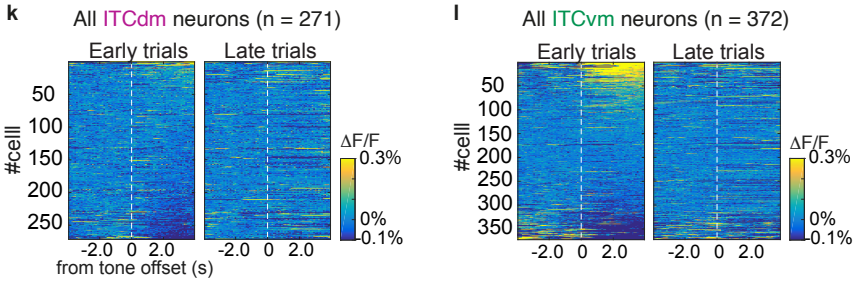

Extended Data Fig. 3 | 2-photon imaging and fibre photometry.
a, Schematic showing dual-colour *in vivo* 2-photon imaging through the implanted GRIN lens. ITC_{dm} neurons were labelled by co-injection of an AAV expressing Cre-dependent tdTomato in FoxP2-Cre mice. A GRIN lens was implanted above ITC_{dm} and surrounding BLA and CeA to record Ca^{2+} responses to aversive skin shocks (USs).
b, Mean projected FOV. Green: GCaMP6; Magenta: tdTomato. The dashed lines indicate the intermediate capsule surrounding ITC_{dm}.
c, Heatplot of Ca^{2+} responses (ΔF/F) to US presentations showing clustered activation of ITC_{dm} neurons.
d, ROIs corresponding to ITC_{dm} (Magenta) and BLA (Blue) neurons. ROI numbers correspond to traces shown in **e**.
e, Example Ca^{2+} traces from ITC_{dm} and BLA neurons. Red lines indicate US presentations (1 s). Note, we confirmed that face skin shock used in this experiment and footshock similarly activated ITC_{dm} neurons (data not shown).
f, Schematic illustrating *in vivo* fibre photometry in a freely moving mouse.
g, ITC_{dm} and ITC_{vm} clusters were targeted with AAVs encoding Cre-dependent jRGECO1a or jGCaMP7f, respectively. Recording fibres were placed in BLA to simultaneously monitor axon terminal Ca^{2+} dynamics of ITC_{dm} and ITC_{vm} axons. Isosbestic control signals were recorded in the blue channel.
h, Example traces of simultaneously recorded dual-colour Ca^{2+} signals and a control signal during a fear conditioning session.
i, Cross correlation traces between two simultaneously recorded Ca^{2+} signals. Dark gray lines represent 5-trial averaged traces and light gray lines represent individual trials.
j, (*Top*) Minimum peak values of cross correlation. (*Bottom*) Lags of the minimum peak points. (N = 2 mice)
k,l, Activity heatplot of trial-averaged responses (*Left*: first 5 trials, *Right*: last 5 trials) to footshock US omissions of all the recorded ITC_{dm} (n = 271 neurons, from 9 mice) (**k**) or ITC_{vm} neurons (n = 372 neurons, from 6 mice) (**l**) aligned by CS offset. Cells were sorted based on their averaged ΔF/F responses in the first 5 trials.

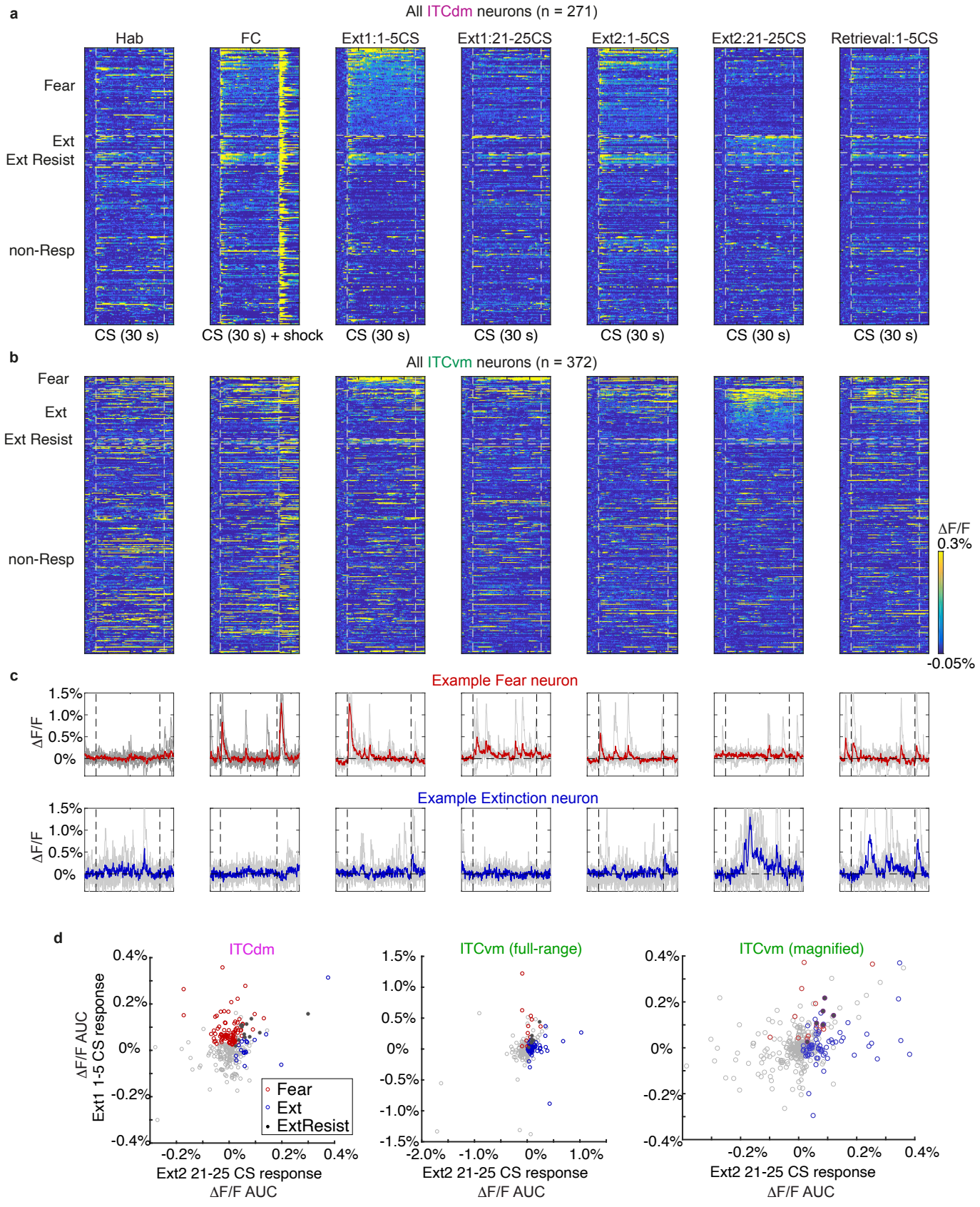
a
All ITCdm neurons (n = 271)
Hab
FC
Ext1:1-5CS
Ext1:21-25CS
Ext2:1-5CS
Ext2:21-25CS
Retrieval:1-5CS
Fear
Ext
Ext Resist
non-Resp
CS (30 s)
CS (30 s) + shock
CS (30 s)
CS (30 s)
CS (30 s)
CS (30 s)
CS (30 s)
b
All ITCvm neurons (n = 372)
Fear
Ext
Ext Resist
non-Resp
ΔF/F
0.3%
-0.05%
c
Example Fear neuron
ΔF/F
1.5%
1.0%
0.5%
0%
Example Extinction neuron
ΔF/F
1.5%
1.0%
0.5%
0%
d
ITCdm
ITCvm (full-range)
ITCvm (magnified)
ΔF/F AUC
Ext1 1-5 CS response
0.4%
0.2%
0%
-0.2%
-0.4%
Fear
Ext
ExtResist
-0.2%
0%
0.2%
0.4%
Ext2 21-25 CS response
ΔF/F AUC
1.5%
1.0%
0.5%
0%
-0.5%
-1.0%
-1.5%
-2.0%
-1.0%
0%
1.0%
Ext2 21-25 CS response
ΔF/F AUC
0.4%
0.2%
0%
-0.2%
-0.4%
-0.2%
0%
0.2%
0.4%
Ext2 21-25 CS response
ΔF/F AUC

Extended Data Fig. 4 | Population activity of ITC_{dm} and ITC_{vm} neurons.
a,b, Heatplots of all recorded neurons. (**a**) 271 ITC_{dm} neurons from 9 mice and (**b**) 372 ITC_{vm} neurons from 6 mice throughout the entire 5-day fear conditioning/extinction paradigm. Neurons were sorted by their classification into Fear, Extinction, Extinction Resistant, and non-Responsive neurons.
c, Example Ca^{2+} traces of a Fear and Extinction neuron from ITC_{dm} and ITC_{vm}, respectively for all time points indicate shown in panels **(a,b)**. Habituation, Ext1: 1-5, Ext2: 21-25, and Retrieval time points are duplicated in **Fig. 2c**.
d, Scatter plots visualising distributions of tone responses of all the recorded ITC_{dm} neurons (Left) and ITC_{vm} neurons (Middle and Right) during Extinction1:1-5trials and Extinction2:21-25trials. Functional cell-types – Fear, Extinction, and Extinction Resistant neurons – are plotted with different colours, non-responsive neurons in grey (c.f. **Fig. 2d**).

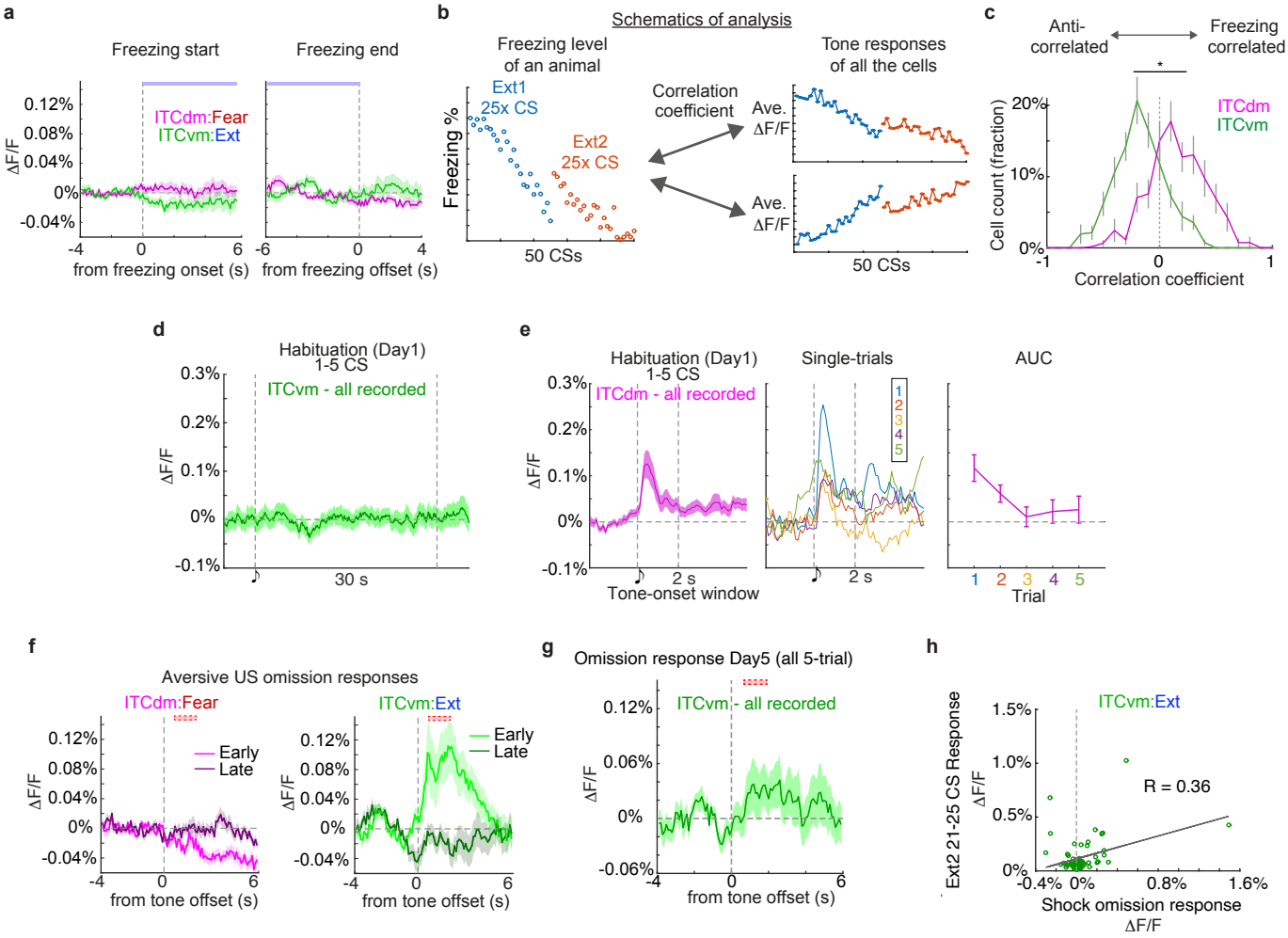
a
Freezing start
Freezing end
ITCdm:Fear
ITCvm:Ext
ΔF/F
0.12%
0.08%
0.04%
0%
-0.04%
-4
0
6
-6
4
from freezing onset (s)
from freezing offset (s)
b
Schematics of analysis
Freezing level of an animal
Freezing %
Ext1 25x CS
Ext2 25x CS
50 CSs
Correlation coefficient
Tone responses of all the cells
Ave. ΔF/F
Ave. ΔF/F
50 CSs
c
Anti-correlated
Freezing correlated
*
ITCdm
ITCvm
Cell count (fraction)
20%
10%
0%
-1
0
1
Correlation coefficient
d
Habituation (Day1)
1-5 CS
ITCvm - all recorded
ΔF/F
0.3%
0.2%
0.1%
0%
-0.1%
30 s
e
Habituation (Day1)
1-5 CS
ITCdm - all recorded
Single-trials
AUC
ΔF/F
0.3%
0.2%
0.1%
0%
-0.1%
1
2
3
4
5
2 s
2 s
Tone-onset window
1 2 3 4 5
Trial
f
Aversive US omission responses
ITCdm:Fear
ITCvm:Ext
Early
Late
ΔF/F
0.12%
0.08%
0.04%
0%
-0.04%
-4
0
6
from tone offset (s)
from tone offset (s)
g
Omission response Day5 (all 5-trial)
ITCvm - all recorded
ΔF/F
0.12%
0.06%
0%
-0.06%
-4
0
6
from tone offset (s)
h
ITCvm:Ext
R = 0.36
Ext2 21-25 CS Response ΔF/F
1.5%
1.0%
0.5%
0%
-0.4% 0%
0.8%
1.6%
Shock omission response ΔF/F

Extended Data Fig. 5 | Properties of ITC_{dm} and ITC_{vm} neurons during fear extinction.
a, Schematics illustrating the analysis shown in (**b**). Correlation coefficients between trial-by-trial (in total, 50 CS trials) freezing levels and CS-response amplitudes of all the recorded neurons across two days of extinction. Distribution of those correlation coefficients (one value from each neuron) were first normalized in each animal, then mean ± SEM values were acquired from all ITC_{dm} and ITC_{vm} recordings and visualized.
b, The distribution of correlation coefficients for ITC_{dm} neurons was skewed towards 1, indicating a larger fraction showed a CS response pattern positively correlated with freezing behaviour. In contrast, ITC_{vm} neurons exhibited the opposite tendency; a response pattern anti-correlated with freezing behaviour. $^{*}P = 1.64 \times 10^{-40}$, Kolmogorov–Smirnov test.
c, Trial-averaged ΔF/F Ca^{2+} responses of ITC_{vm} neurons aligned to tone on habituation (Day1).
d, (*Left*) Averaged Ca^{2+} responses to tone CS onset of ITC_{dm}. Vertical dotted lines indicate onsets and 2 seconds time-window of CSs for AUC analysis. (*Center*) Single-trial average of all the ITC_{dm} neurons. (Right) Area under the curve (AUC) quantification of single-trial responses shown in the *Center* panel. $P = 0.027$, one-way ANOVA.
e, Trial-averaged ΔF/F Ca^{2+} responses of ITC_{dm} Fear and ITC_{vm} Extinction neurons aligned to freezing onset and offset.
f, Trial-averaged ΔF/F Ca^{2+} responses of ITC_{dm} Fear and ITC_{vm} Extinction neurons aligned to US omission on Day3. Early: CS1-5, Late: CS21-25. Dotted red boxes indicate the expected timing of US delivery.
g, Trial-averaged ΔF/F Ca^{2+} responses of all recorded ITC_{vm} neurons aligned to US omission on Day5. The dotted red box indicates the expected timing of US delivery.
h, Relationship between CS responses during last 5 trials of extinction training on Day4 and US omission responses on Day3 in ITC_{vm} Extinction neurons shows a weak positive correlation.

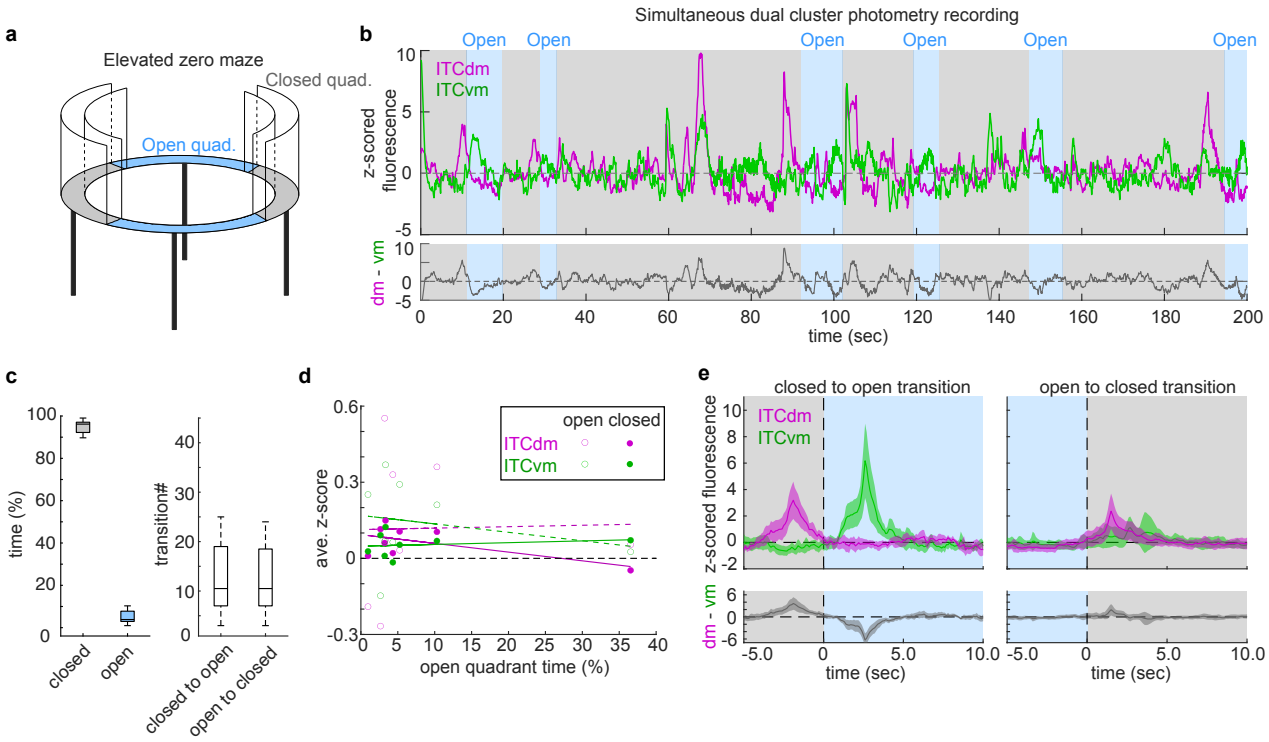
a
Elevated zero maze
Closed quad.
Open quad.
b
Simultaneous dual cluster photometry recording
Open
ITCdm
ITCvm
z-scored fluorescence
dm - vm
time (sec)
c
time (%)
transition#
closed
open
closed to open
open to closed
d
open closed
ITCdm
ITCvm
ave. z-score
open quadrant time (%)
e
closed to open transition
open to closed transition
ITCdm
ITCvm
z-scored fluorescence
dm - vm
time (sec)

Extended Data Fig. 6 | Simultaneous photometry recordings from ITC_{dm} and ITC_{vm} during state transition

a, Schematic of an elevated zero maze apparatus.

b, (Top) Example z-scored Ca^{2+} traces of simultaneously recorded ITC_{dm} (magenta) and ITC_{vm} (green) neurons with the corresponding location in the maze indicated with gray (closed quadrant) and blue (open quadrant) shading. (Bottom) Difference between the ITC_{dm} and ITC_{vm} signals.

c, (Left) Percentage of time spent in closed and open quadrants. (Right) Total number of transitions from close to open quadrants (15 ± 3.9, mean ± SEM) or from open to closed quadrants. N = 5 mice.

d, Averaged activity of ITC_{dm} or ITC_{vm} neurons in the closed or open quadrants did not correlate with the total time spent in open quadrants. Regarding the larger variability in ITC activities in open quadrants, we note that the time an animal spent in open quadrants was, on average, much shorter than that in closed quadrants (**c**). As such, activity in open quadrants was to a lesser extent averaged out, resulting in higher variability. 8 sessions from N = 5 mice.

e, (Top) Averaged Ca^{2+} traces during transitions between quadrants. Changes in the balance between ITC_{dm} and ITC_{vm} parallel a transition from a closed to an open quadrant. (Bottom) Difference between the ITC_{dm} and ITC_{vm} signals.

Briefly stated, the results of this experiment make at least three important points: 1) the role of the ITC clusters extends beyond signaling acute, cue-triggered fear states to conditioned fear stimuli to encompass state transitions during exploration of a potentially threatening environment, 2) the clusters exhibit markedly divergent, opposing responses to transitions between protected and unprotected environments, as they do in response to conditioned and extinguished fear cues, 3) the pattern of results shows that increased ITC_{vm} activity occurs when the animal moves from the protected, closed, to the unprotected, open, quadrants. Potentially, this increase in ITC_{vm} neuron activity may serve to inhibit defensive behaviour and thereby enable exploration of the unprotected open quadrants, analogous to the inhibition of freezing behaviour following extinction. Such cross-task neuronal function is not without precedent, for example BLA neuronal activity during elevated plus-maze open arm exploration is anti-correlated with conditioned freezing behaviour in the same mice[47].

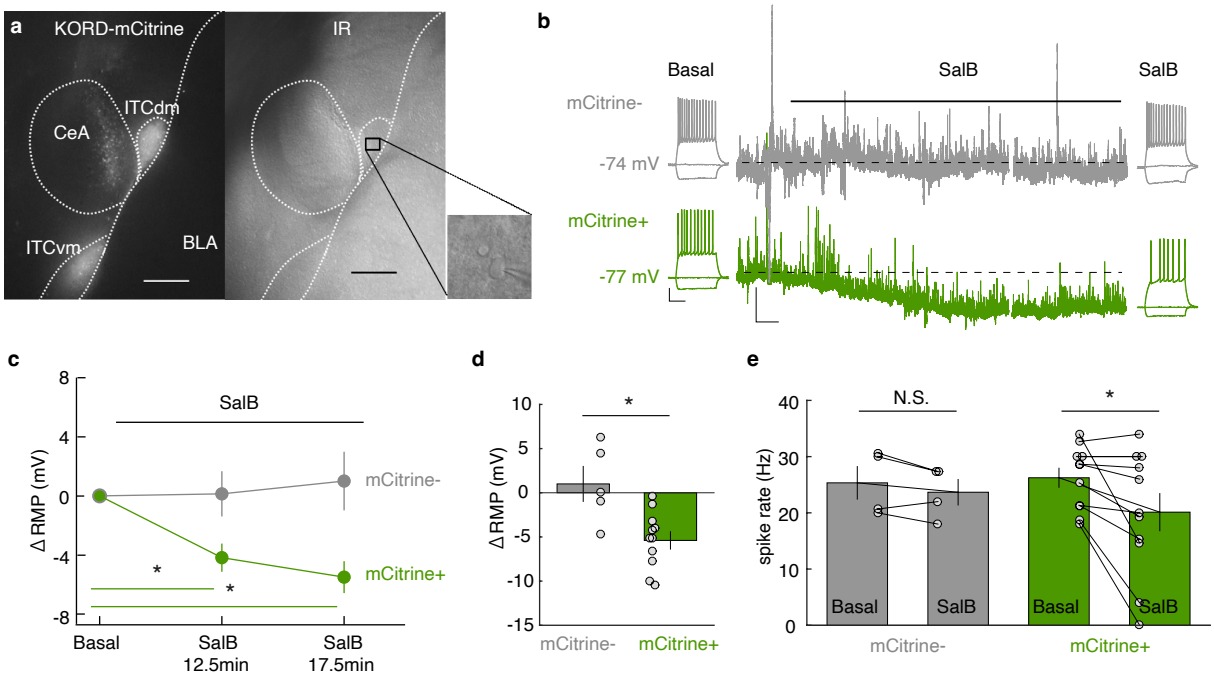
a
KORD-mCitrine
IR
CeA
ITCdm
ITCvm
BLA
b
Basal
SalB
SalB
mCitrine-
-74 mV
mCitrine+
-77 mV
c
SalB
Δ RMP (mV)
mCitrine-
mCitrine+
Basal
SalB 12.5min
SalB 17.5min
d
Δ RMP (mV)
mCitrine-
mCitrine+
e
N.S.
spike rate (Hz)
Basal
SalB
Basal
SalB
mCitrine-
mCitrine+

Extended Data Fig. 7 | *Ex vivo* validation of KORD.

a, Fluorescence (mCitrine, left) and infrared (IR, right) images from a slice used for recordings in a FoxP2-Cre mouse injected with an AAV-DIO-KORD-mCitrine into ITC_{dm} and ITC_{vm}. Inset: Infrared image from a recorded ITC_{dm} neuron. Scale bar: 200 μm.

b, Representative current-clamp traces illustrating supra-threshold responses to a +60 pA current injection and continuous recording of the resting membrane potential (RMP) during application of Salvinorin B (SalB, 100 nM) from control (mCitrine-) and KORD-infected (mCitrine+) ITC neurons. Scale bars: RMP: 5 mV, 1 min; current steps: 20 mV, 200 ms.

c, SalB application induced a significant hyperpolarization of the membrane potential in mCitrine+ neurons (n = 10 neurons from 4 mice) at both time points vs. baseline (12.5-min: * $P = 0.003$, 17.5-min: * $P = 0.0001$, Dunnett's test). Changes in membrane potential were not significant in the mCitrine- control neurons (n = 5 neurons from 3 mice) at both time points vs. baseline (12.5-min: $P = 0.99$, 17.5-min: $P = 0.84$, Dunnett's test).

d, Comparison of membrane potential changes (ΔRMP) at 17.5 min after application of SalB. Changes in KORD-infected neurons (mCitrine+) were significantly different from control (* $P = 0.013$, Wilcoxon rank-sum test; n = 5 neurons from 3 mice and n =11 neurons from 5 mice for mCitrine- and mCitrine+, respectively).

e, Comparisons of spike rates in response to +60 pA current injections before and 17.5 min after application of SalB. KORD-infected neurons (mCitrine+, n = 11) significantly reduced spike rate (from 26.2 ± 1.69 Hz to 20.1 ± 3.30 Hz, * $P = 0.016$, Wilcoxon signed-rank test). In contrast, mCitrine- neurons (n = 4 neurons from 3 mice) did not show a significant reduction in spike rate (from 25.3 ± 2.89 Hz to 23.7 ± 2.27 Hz, $P = 0.25$, Wilcoxon signed-rank test).

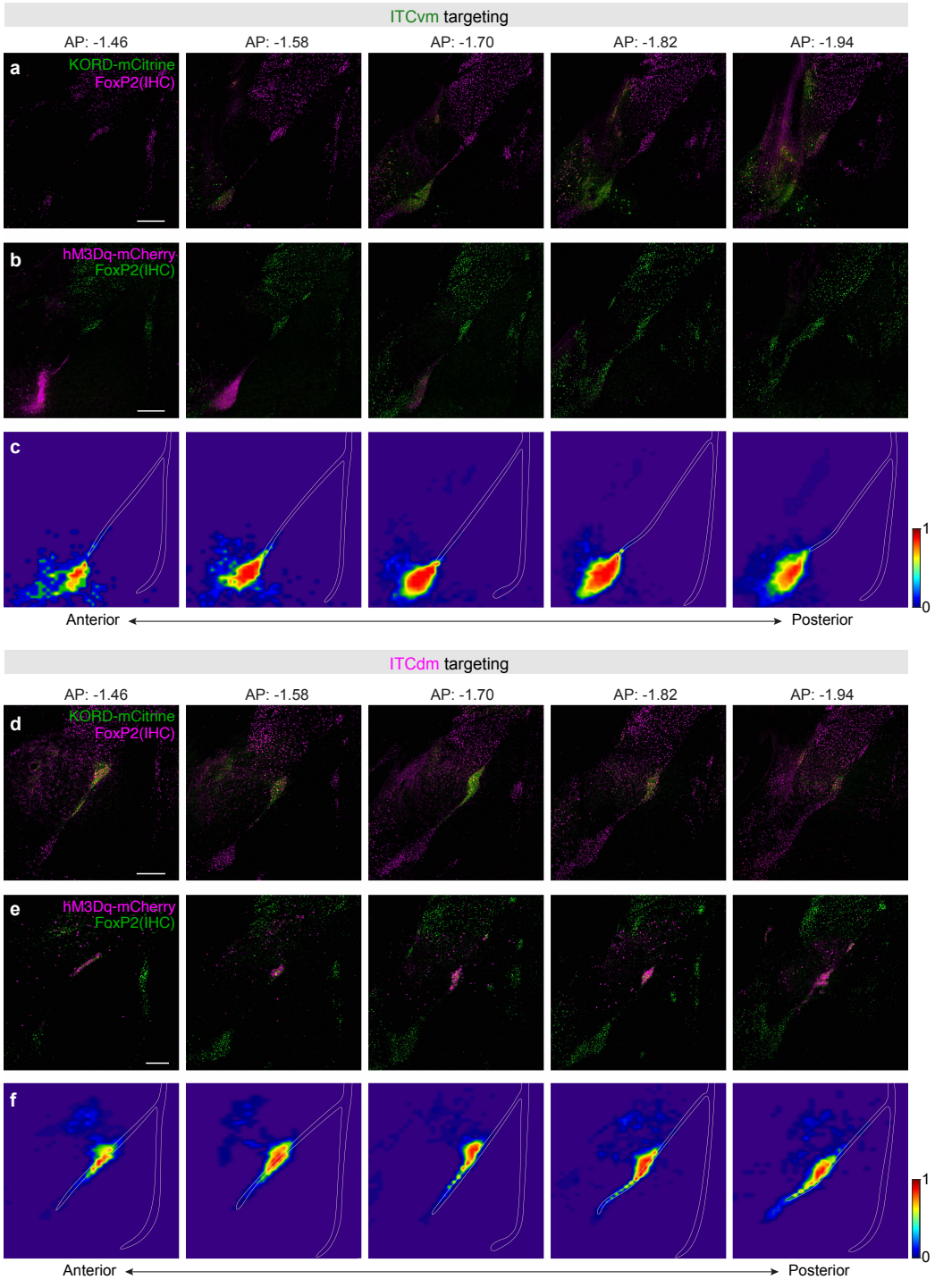
ITCvm targeting
AP: -1.46
AP: -1.58
AP: -1.70
AP: -1.82
AP: -1.94
a
KORD-mCitrine
FoxP2(IHC)
b
hM3Dq-mCherry
FoxP2(IHC)
c
1
0
Anterior
Posterior
ITCdm targeting
AP: -1.46
AP: -1.58
AP: -1.70
AP: -1.82
AP: -1.94
d
KORD-mCitrine
FoxP2(IHC)
e
hM3Dq-mCherry
FoxP2(IHC)
f
1
0
Anterior
Posterior

Extended Data Fig. 8 | Histology for chemogenetic manipulations of distinct ITC clusters.
a, Examples of histological validation of KORD-mCitrine expression in ITC_{vm} neurons across multiple anterior-to-posterior coronal sections. Following all the behavioural experiments (**Fig. 3**), mice were sacrificed and slices (50 μm) cut and stained with an anti-FoxP2 antibody. Scale bar: 200 μm.
b, Examples of histological validation of hM3Dq-mCherry expression in ITC_{vm} neurons across multiple anterior-to-posterior coronal sections. Scale bar: 200 μm.
c, Heatmaps illustrating virus expression aggregated across Cre+ mice in **(a)** and **(b)**. Scale bar indicates the fraction of animals exhibiting expression at each locus (0: no mice expressed; 1: all mice expressed).
d, Examples of histological validation of KORD-mCitrine expression in ITC_{dm} neurons across multiple anterior-to-posterior coronal sections. Scale bar: 200 μm.
e, Examples of histological validation of hM3Dq-mCherry expression in ITC_{dm} neurons across multiple anterior-to-posterior coronal sections. Scale bar: 200 μm.
f, Heatmaps illustrating virus expression aggregated across Cre+ mice in **(d)** and **(e)**. Scale bar indicates the fraction of animals exhibiting expression at each locus (0: no mice expressed; 1: all mice expressed). Bregma levels are note above the panels in **(a)** and **(d)**.

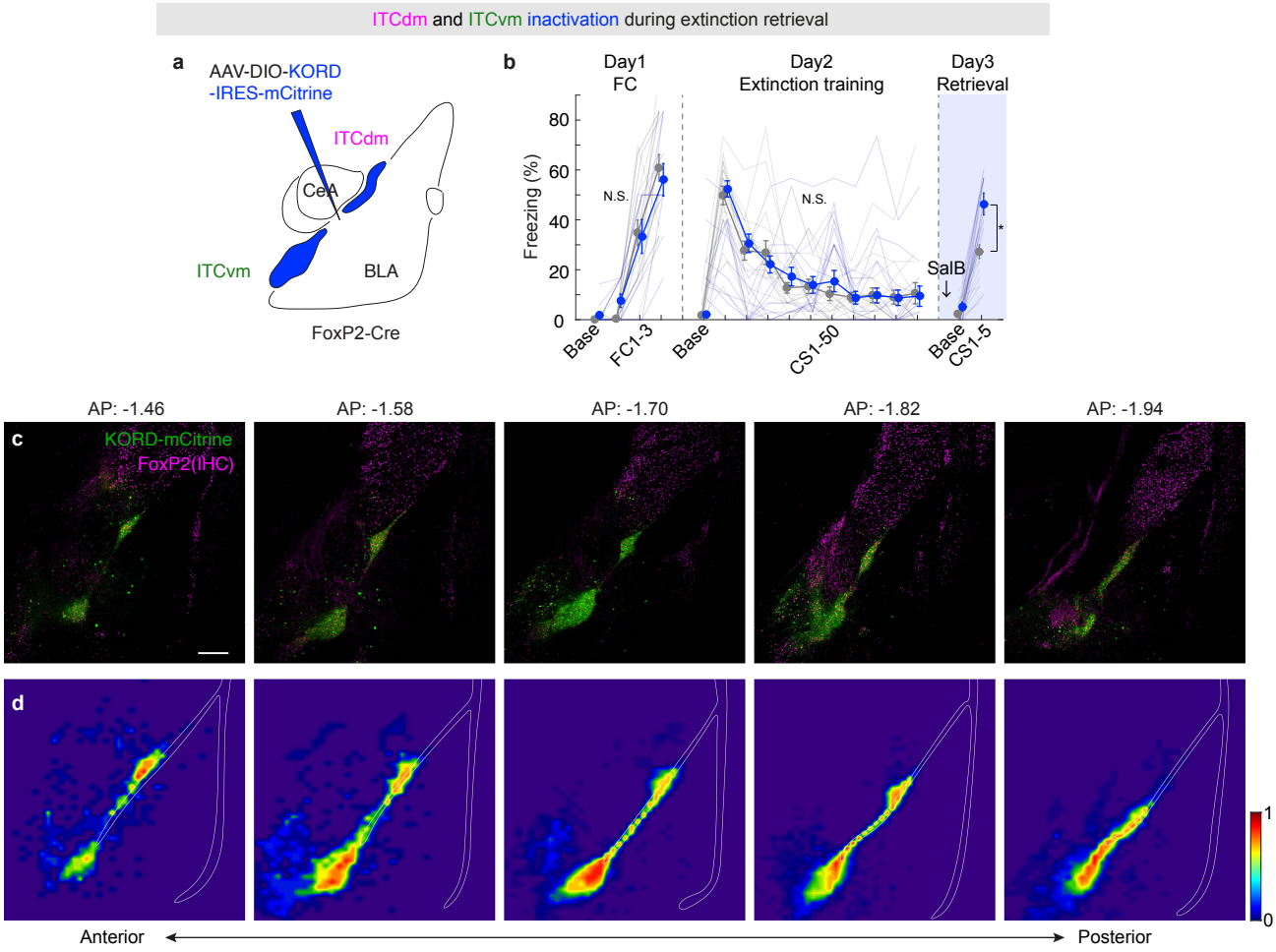
ITCdm and ITCvm inactivation during extinction retrieval
a
AAV-DIO-KORD
-IRES-mCitrine
ITCdm
CeA
ITCvm
BLA
FoxP2-Cre
b
Day1
FC
Day2
Extinction training
Day3
Retrieval
Freezing (%)
80
60
40
20
0
N.S.
N.S.
*
SalB
Base
FC1-3
Base
CS1-50
Base
CS1-5
AP: -1.46
AP: -1.58
AP: -1.70
AP: -1.82
AP: -1.94
c
KORD-mCitrine
FoxP2(IHC)
d
1
0
Anterior
Posterior

Extended Data Fig. 9 | Chemogenetic manipulations of both ITC_{dm} and ITC_{vm} clusters.
a, Schematic showing the dual-cluster chemogenetic manipulation experiment. An AAV encoding Cre-dependent KORD was targeted to both ITC_{vm} and ITC_{dm} neurons in FoxP2-Cre mice.
b, Freezing behaviour of experimental (Cre+) and control (Cre-) mice; controls were injected with the AAV and administered with the ligand. Arrows and colour-shadings indicate the timing of SalB administration prior to extinction retrieval. Freezing levels on extinction retrieval (Day3): Cre+: 46.4 ± 4.3%; Cre-: 27.3 ± 2.7%; * $P < 0.0001$, repeated measures ANOVA followed by Sidak post-hoc test; N.S.: not significant.
c, Examples of histological validation of KORD-mCitrine expression in ITC_{vm} and ITC_{dm} neurons across multiple anterior-to-posterior coronal sections. Following behavioural experiments, mice were sacrificed and slices (50 μm) cut and stained with an anti-FoxP2 antibody. Scale bar: 200 μm.
d, Heatmaps illustrating virus expression aggregated across Cre+ mice. Scale bar indicates the fraction of animals exhibiting expression at each locus (0: no mice expressed; 1: all mice expressed).

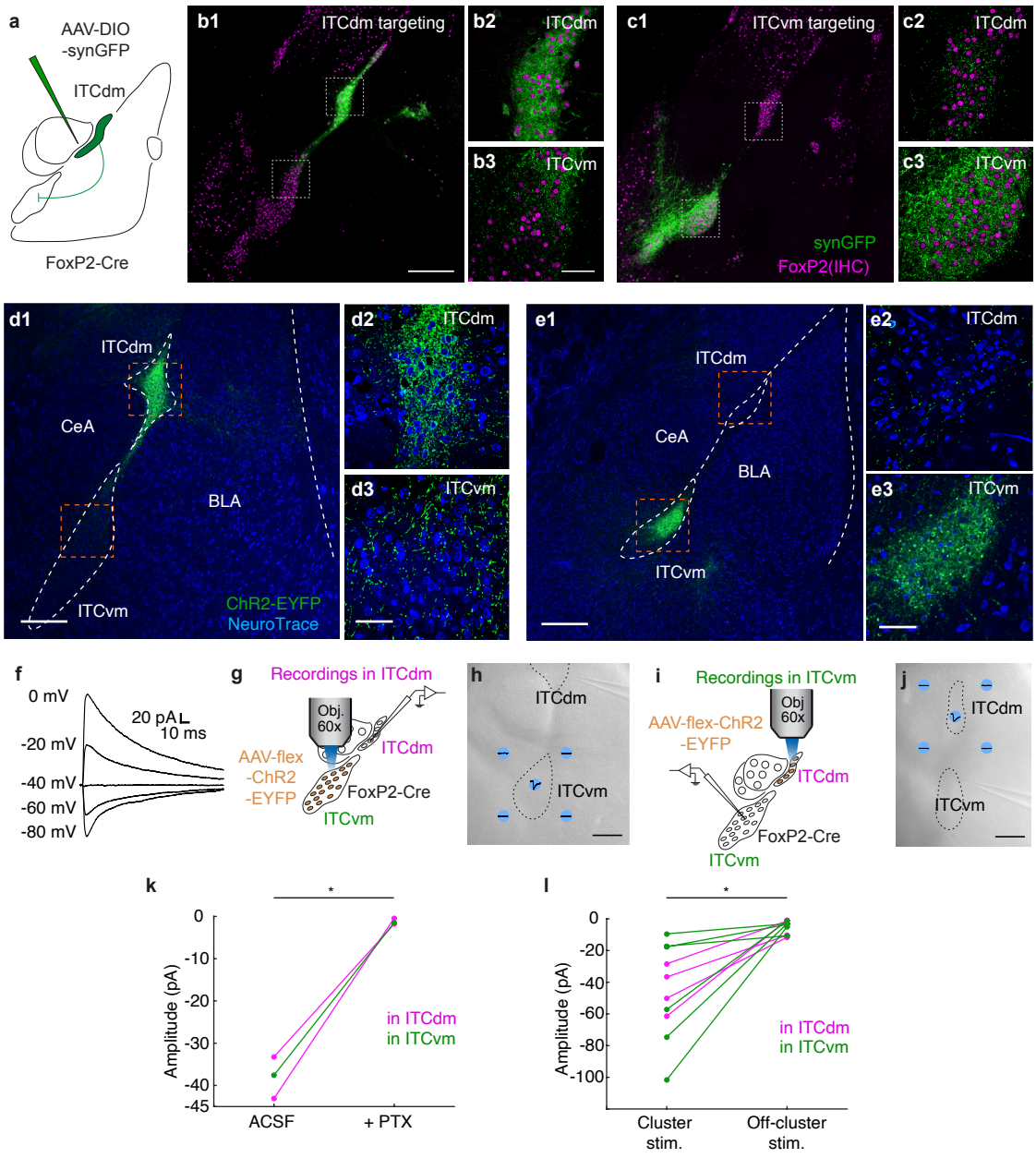
a
AAV-DIO
-synGFP
ITCdm
FoxP2-Cre
b1
ITCdm targeting
b2
ITCdm
b3
ITCvm
c1
ITCvm targeting
c2
ITCdm
c3
ITCvm
synGFP
FoxP2(IHC)
d1
ITCdm
CeA
BLA
ITCvm
ChR2-EYFP
NeuroTrace
d2
ITCdm
d3
ITCvm
e1
ITCdm
CeA
BLA
ITCvm
e2
ITCdm
e3
ITCvm
f
0 mV
-20 mV
-40 mV
-60 mV
-80 mV
20 pA
10 ms
g
Recordings in ITCdm
Obj.
60x
AAV-flex
-ChR2
-EYFP
ITCdm
FoxP2-Cre
ITCvm
h
ITCdm
ITCvm
i
Recordings in ITCvm
Obj
60x
AAV-flex-ChR2
-EYFP
ITCdm
FoxP2-Cre
ITCvm
j
ITCdm
ITCvm
k
*
Amplitude (pA)
0
-10
-20
-30
-40
-45
in ITCdm
in ITCvm
ACSF
+ PTX
l
*
Amplitude (pA)
0
-20
-40
-60
-80
-100
in ITCdm
in ITCvm
Cluster
stim.
Off-cluster
stim.

Extended Data Fig. 10 | Reciprocal inhibitory connections between ITC clusters.
a, Histological validation of selective ChR2 expression in ITC_{dm} (**a1-3**) and ITC_{vm} (**a4-6**). Scale bars: 500 μm (**a1,4**); 50 μm (**a3,6**).
b, Representative example of IPSCs recorded at different holding potentials from an ITC_{dm} neuron.
c,e, Schematic illustrating *ex vivo* slice electrophysiological experiments with direct cluster stimulation. The ITC_{vm} (**c**) or ITC_{dm} (**e**) cluster was targeted with an AAV encoding Cre-dependent ChR2. Recordings were performed in the other cluster while selectively photostimulating the ChR2-positive cluster or the surrounding area with aperture-restricted stimulation (see **Methods**).
d,f, Images taken from the recording setup illustrating positions of on- and off-cluster stimulation for ITC_{vm} while recording in ITC_{dm} and vice versa.
g, Summary of PTX application experiments (n = 3 from 3 mice). Magenta lines represent $ITC_{vm} \rightarrow ITC_{dm}$ connections and green lines represent $ITC_{dm} \rightarrow ITC_{vm}$ connections. * $P = 0.005$, paired-t test.
h, Summary of experiments shown in (**c**)-(**f**). On-cluster photostimulation evoked significantly larger IPSCs than off-cluster stimulation. Note, the highest value out of the 4 off-cluster stimulation sites were used. * $P = 0.0016$, paired-t test.

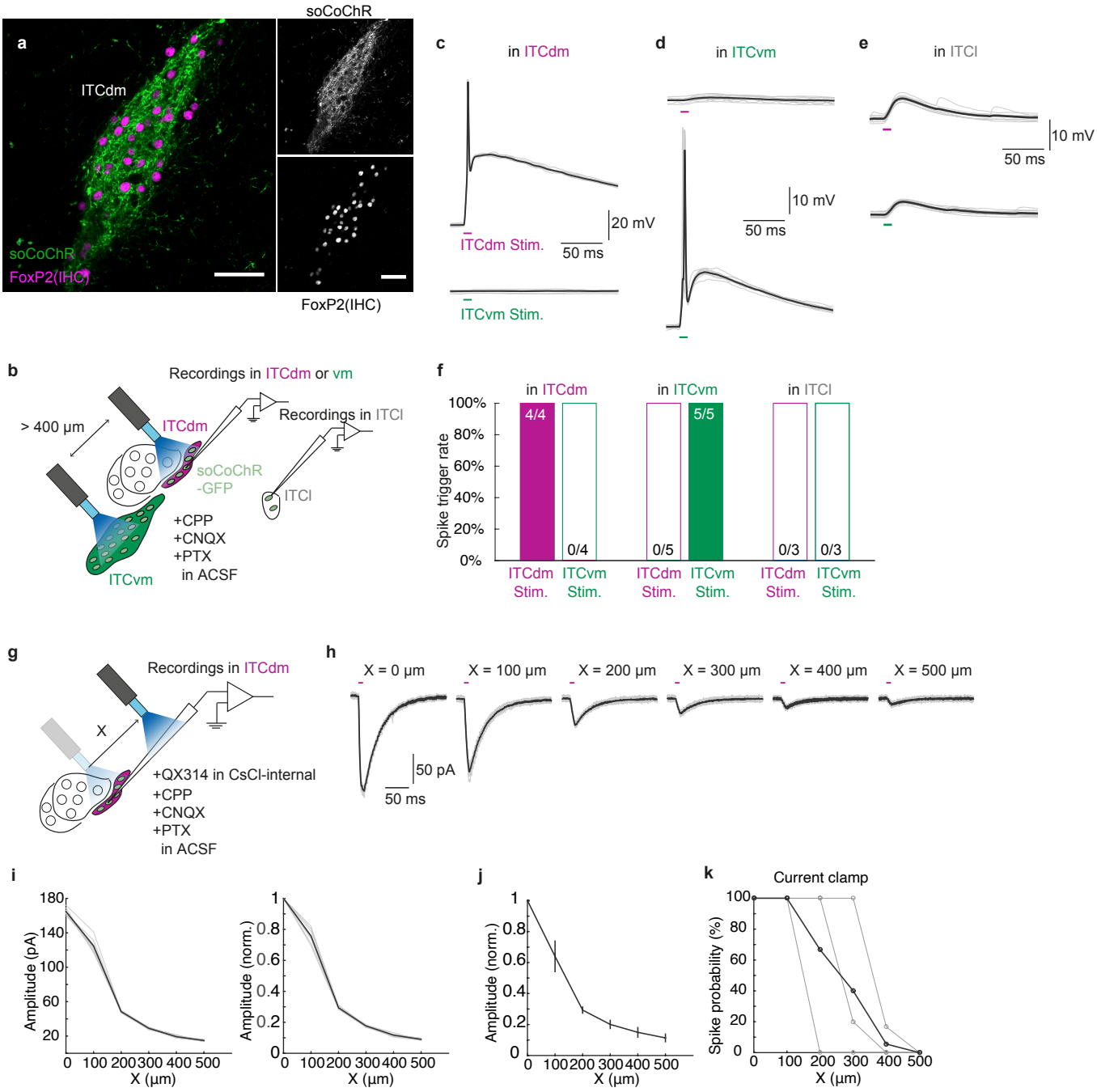
a
soCoChR
ITCdm
soCoChR
FoxP2(IHC)
FoxP2(IHC)
b
Recordings in ITCdm or vm
> 400 µm
ITCdm
Recordings in ITCl
soCoChR
-GFP
ITCl
+CPP
+CNQX
+PTX
in ACSF
ITCvm
c
in ITCdm
20 mV
ITCdm Stim.
50 ms
ITCvm Stim.
d
in ITCvm
10 mV
50 ms
e
in ITCl
10 mV
50 ms
f
in ITCdm
in ITCvm
in ITCl
Spike trigger rate
100%
80%
60%
40%
20%
0%
4/4
0/4
0/5
5/5
0/3
0/3
ITCdm Stim.
ITCvm Stim.
ITCdm Stim.
ITCvm Stim.
ITCdm Stim.
ITCvm Stim.
g
Recordings in ITCdm
X
+QX314 in CsCl-internal
+CPP
+CNQX
+PTX
in ACSF
h
X = 0 µm
X = 100 µm
X = 200 µm
X = 300 µm
X = 400 µm
X = 500 µm
50 pA
50 ms
i
Amplitude (pA)
180
140
100
60
20
0 100 200 300 400 500
X (µm)
Amplitude (norm.)
1
0.8
0.6
0.4
0.2
0
0 100 200 300 400 500
X (µm)
j
Amplitude (norm.)
1
0.8
0.6
0.4
0.2
0
0 100 200 300 400 500
X (µm)
k
Current clamp
Spike probability (%)
100
80
60
40
20
0
0 100 200 300 400 500
X (µm)

Extended Data Fig. 11 | Selective *ex vivo* ITC cluster stimulation.
a, Histological validation of selective soCoChR expression. Scale bars: 50 μm.
b, Schematic illustrating *ex vivo* slice electrophysiological experiments. ITC_{dm} and ITC_{vm} neurons were targeted with an AAV encoding Cre-dependent soCoChR. Two optical fibres for photostimulation were placed above the ITC clusters. Whole-cell recordings were performed from neurons in the ITC_{dm}, ITC_{vm}, and lateral ITC (ITC_l) clusters. To block synaptic currents, CPP (10 μM), CNQX (10 μM), and PTX (100 μM) were applied.
c-e, Example responses to photostimulation of ITC_{dm} or ITC_{vm} clusters recorded under current-clamp configuration from ITC_{dm} (**c**), ITC_{vm} (**d**), and ITC_l (**e**) neurons.
f, Summary of experiments shown in **b-e**. All recorded ITC_{dm} and ITC_{vm} neurons fired action potentials selectively in response to photostimulation with the corresponding fibre. ITC_l neurons did not fire action potentials upon photostimulation of ITC_{dm} or ITC_{vm} clusters.
g, Schematic illustrating experiments wherein the position of the optical fibre was systematically moved away from the optimal location (X = 0 μm). To block synaptic currents, CPP (10 μM), CNQX (10 μM), and PTX (100 μM) were applied. These experiments further confirm spatial resolution of the photostimulation configuration.
h, Example voltage-clamp recordings from an ITC neuron showing IPSCs evoked at different positions of the optical fibre.
i, *Left*: Quantification of peak IPSC amplitudes of the neuron shown in (**h**). *Right*: Normalized by the value at X = 0 μm.
j, Summary of all recorded neurons (n = 3 from 3 mice).
k, Summary of additionally performed current-clamp recordings (n = 3 from 3 mice).

ITC to CeM connectivity

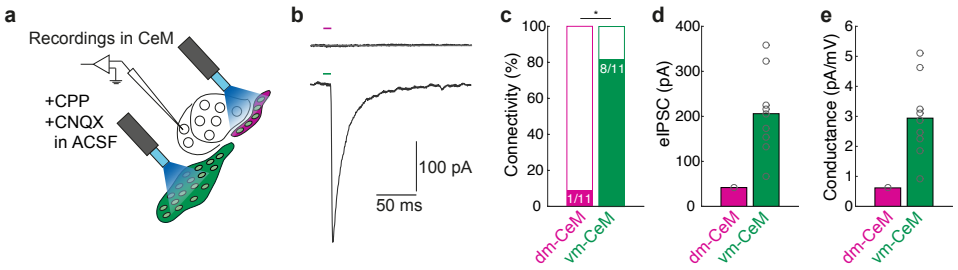

ITC to PAG-projecting CeM neuron connectivity

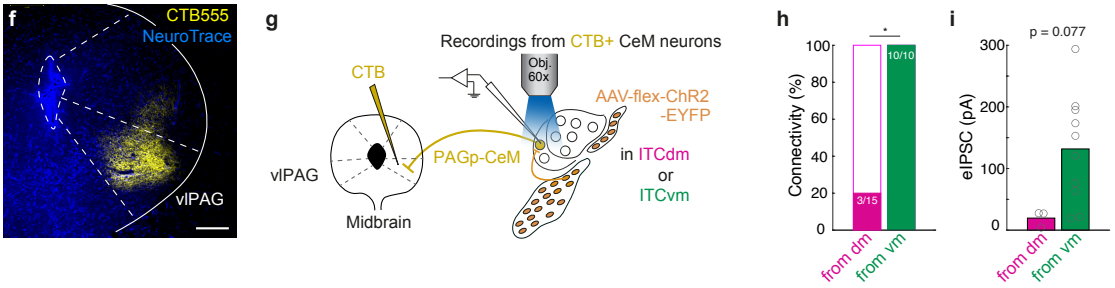

PL/IL-projecting BLA neurons histology

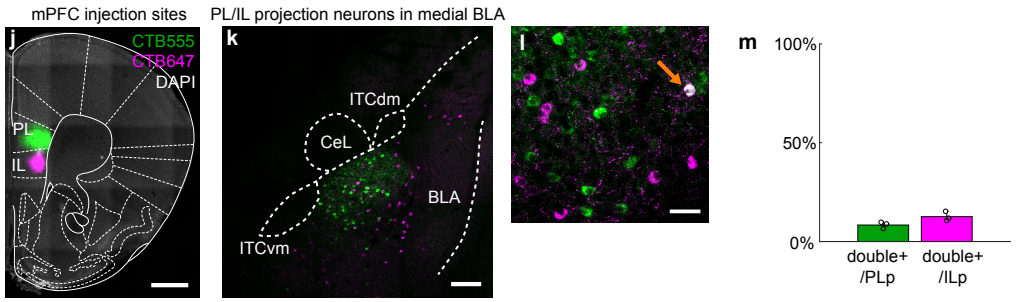

Summary scheme

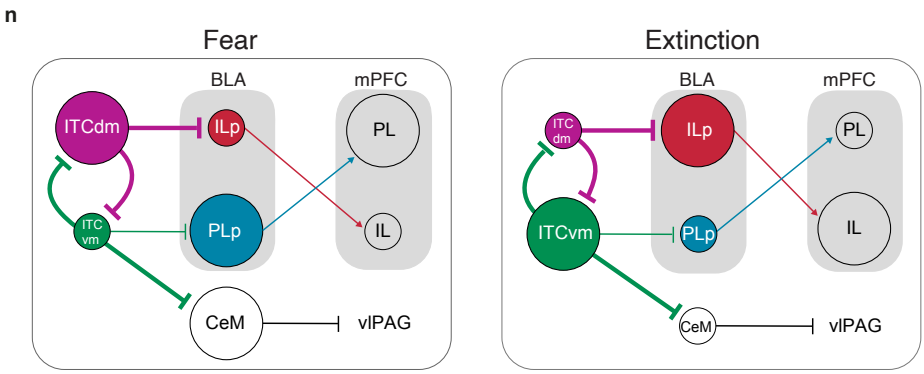

Extended Data Fig. 12 | ITC to CeM connectivity.

a, Schematic illustrating the experimental design used to assess connectivity between ITC_{dm} or ITC_{vm} neurons and CeM neurons. To isolate IPSCs, CPP (10 μM) and CNQX (10 μM) were applied.

b, Example voltage-clamp recording from a CeM neuron showing selective IPSC elicited by stimulation of the ITC_{vm} but not ITC_{dm}.

c, Summary of connectivity from ITC_{dm} and ITC_{vm} to CeM (n = 11 neurons from 4 mice). * $P = 7.5 \times 10^{-3}$, Fisher's exact test.

d, Evoked IPSC amplitudes recorded from CeM neurons (at -70mV holding potential) in response to stimulation of ITC_{dm} or ITC_{vm} clusters.

e, Synaptic conductance calculated based on IPSC amplitudes recorded at three different holding potentials (–60, –70, and –80 mV).

f, Example injections of CTB555 targeted to the ventrolateral periaqueductal gray (vlPAG). Scale bar: 200 μm.

g, Schematic illustrating the experimental design used to assess connectivity between ITC_{dm} or ITC_{vm} neurons and CeM neurons projecting to the vlPAG. vlPAG-projecting CeM neurons were retrogradely labelled with CTB injections into the vlPAG. Whole-cell recordings were performed in CTB+ CeM neurons while photostimulating incoming axons expressing ChR2-EYFP from either the ITC_{dm} or ITC_{vm}.

h, Summary of connectivity from ITC_{dm} and ITC_{vm} to vlPAG-projecting CeM neurons (n = 15, 10 neurons from 4, 4 mice). * $P = 0.0001$, Fisher's exact test.

i, Evoked IPSC amplitudes recorded from CTB+ CeM neurons (at 0 mV holding potential) in response to stimulation of axons from ITC_{dm} or ITC_{vm}.

j, Example injections of CTB555 and CTB647 targeted to the PL or IL, respectively. Scale bar: 500 μm.

k, Example BLA histology showing PL- (PLp) and IL-projecting (ILp) BLA neurons. Both subpopulations are located in the medial part of the BLA. Scale bar: 200 μm.

l, Mostly non-overlapping PLp and ILp subpopulations; orange arrow indicates an example of a double-labelled neuron. Scale bar: 50 μm.

m, Quantification of double-labelled neurons (N = 3 mice).

3.2. **Project 2**: Di-synaptic specificity of an amygdala-midbrain pathway for fear learning (published as Massi*, Hagihara* et al., 2021, *Science Advances*)

Léma Massi[1,4], Kenta M. Hagihara[1,2,4], Julien Courtin[1], Julian Hinz[1,2], Christian Müller[1], Maria Sol Fustiñana[1], Chun Xu[1,3], Nikolaos Karalis[1,4], and Andreas Lüthi[1,2,4,5,*]
[1] Friedrich Miescher Institute for Biomedical Research, Maulbeerstrasse 66, CH-4058 Basel, Switzerland. [2] University of Basel, Basel, Switzerland. [3] Institute of Neuroscience, Center for Excellence in Brain Science and Intelligence Technology, Chinese Academy of Sciences, Shanghai, China.

[4]:These authors contributed equally to this work
[5]:Lead contact
*Correspondence: andreas.luthi@fmi.ch

Summary
Memory encoding and retrieval relies on specific interactions across multiple brain areas. Even though connections between individual brain areas have been extensively studied, the anatomical and functional specificity of neuronal circuit organization underlying serial information transfer across multiple brain areas remains unclear. Here, we combine trans-synaptic viral tracing, optogenetic manipulations, and recordings of calcium dynamics to dissect fine-scale connectivity linking the basolateral (BLA) and central amygdala (CeA) with the periaqueductal gray (PAG), three brain areas necessary for conditioned fear. We identify a distinct BLA subpopulation that connects di-synaptically to PAG via CeA. This specific di-synaptic pathway is necessary for fear learning, and exhibits learning-related plasticity, in contrast to the non-specific monosynaptic projections. Together, our findings demonstrate the utility of multi-synaptic approaches for functional circuit analysis and indicate that di-synaptic specificity may be a general feature of neuronal circuit organization.

Introduction
Learning to associate potential threats with predictive cues is a critical adaptive brain function. Previous work has identified BLA and CeA (Tovote et al., 2015) as indispensable brain structures for the acquisition and expression of conditioned fear memories. Based on anatomical tracing studies (Pitkänen et al., 1997), pharmacological (Jimenez and Maren, 2009), and optogenetic manipulations (Namburi et al., 2015; Tye et al., 2011), a canonical model has been developed in which conditioned sensory inputs are transmitted in a serial manner from the BLA to CeA and eventually to the ventrolateral periaqueductal gray (vlPAG), a midbrain structure involved in the generation of conditioned defensive behaviors, such as freezing (Fanselow, 1991; LeDoux et al., 1988; Li, 2019; Penzo et al., 2014; Tovote et al., 2016). However, there remains scant, controversial experimental evidence for a role of this pathway from the BLA to the vlPAG, as opposed to alternative (Nagase et al., 2019; Palmiter, 2018) or more complex indirect pathways (Kim et al., 2017) in the acquisition and expression of conditioned appetitive and aversive behaviors (Kim et al., 2016, 2017; Namburi et al., 2015). In particular, it remains unknown whether this information transmission is organized at the brain region level or whether there is a specific subpopulation of BLA neurons projecting to the CeA that eventually reaches the vlPAG to drive behaviorally relevant responses.

Results
To disentangle these possibilities, we first sought to describe the anatomical specificity of the BLA-CeA-vlPAG pathway. To achieve this, we used a di-synaptic rabies virus (RV) approach, by injecting a retrograde Cre virus into vlPAG and RFP-encoding EnvA pseudo-typed G-protein-deleted RV into CeA (**Figure S1A**). We found rabies-labeled neurons preferentially located in the posterolateral part of BLA (BLAp, **Figure S1B-C**), suggesting the existence of a BLA subpopulation di-synaptically connected to the vlPAG. Although a recent study has

systematically investigated BLAp outputs and found various subcortical projections including lateral septum, bed nucleus of the stria terminalis, and mediodorsal thalamic nucleus, its CeA connectivity was not addressed (Hintramayan et al., 2021). In addition, earlier tracing studies described that both BLAp and anterior BLA (in particular, basal amygdala, BA) send axons to the medial CeA (Krettek and Price, 1978; Pare and Pare,1995; Pitkänen, 1997), suggesting that conventional axon tracing methods are not sufficient to describe the underlying anatomical specificity of the BLAp. Notably, as previously described, we found no direct projection from BLA to vlPAG (Xu et al., 2016) (**Figure S1D-F**).

The identification of this BLAp-CeA-vlPAG pathway raised the question of the function of this pathway for fear learning and expression. Before investigating the functional roles of this BLAp-CeA-vlPAG pathway, we wanted to assess the involvement of the general BLA to CeA mono-synaptic pathway in the acquisition and expression of conditioned freezing responses. To achieve this, we optogenetically inhibited CeA-projecting BLA neurons using an intersectional viral approach (**Figure 1,** see **STAR Methods**). Notably, inhibition of CeA-projecting BLA neurons during auditory fear conditioning (FC) had no effect on freezing behavior during FC (**Figure 1E**) or, consistent with previous work (Namburi et al., 2015), the retrieval of the fear memory the next day (**Figure 1F**). Since BLA neurons are functionally highly heterogeneous, we hypothesized that the simultaneous inhibition of all CeA-projecting BLA neurons might have masked the effect of specific pathways involved in the acquisition and expression of conditioned fear. Therefore, we next tested whether the above anatomically described di-synaptic pathway could play a critical role in fear learning. To achieve this, we used the di-synaptic RV with ArchT-encoding RV (**Figure 1C, D,** see **STAR Methods**). When we optogenetically inhibited BLAp-CeA-vlPAG pathway during FC, we found no effects on freezing behavior during FC (**Figure 1E**), but a marked deficit in memory retrieval the next day (**Figure 1F**). These effects could not be attributed to RV-associated toxicity because, in the absence of photo-silencing, rabies-infected animals could be re-conditioned (**Figure S2**).

This specific involvement of the disynaptic BLAp-CeA-vlPAG pathway in memory retrieval, raised the question of how are these neurons connected to control the behavioral output. Indeed, the CeA contains functionally and molecularly distinct neuronal subpopulations (Fadok et al., 2017; Kim et al., 2017; Li, 2019). Previous work identified somatostatin-expressing CeA neurons (SST+) as a major subpopulation projecting to vlPAG (Kim et al., 2017; Penzo et al., 2014), and stimulation of SST+ CeA neuron somata elicits freezing behavior in naïve and conditioned animals (Fadok et al., 2017; Li et al., 2013) (but see (Kim et al., 2017)). However, it remains unknown whether it is the vlPAG projections of SST+ CeA neurons that mediates this effect. In contrast, a previous study has implicated these projections in appetitive rather than aversive behavior (Kim et al., 2017). Using cell-type specific RV tracing, we established that BLAp neurons targeted SST+ CeA neurons projecting to vlPAG (**Figure 2A, Figure S3**, see **Supplemental Notes**). We rarely found rabies positive neurons in the medial part of the BLA, which is juxtaposed to the CeA, suggesting that Cre-dependent AAV injections targeting SST+ CeA neurons did not cause leakage into in SST+ BLA neurons (**Figure S3E**). Further, using ArchT-mediated optogenetic inhibition during FC, we showed that this di-synaptic pathway is indispensable both for the acquisition and the retrieval of conditioned freezing responses (**Figure 2B,C**). These effects are likely due to BLAp inputs directly onto SST+ CeA neurons projecting to vlPAG, rather than due to axonal collaterals of SST+ CeA cells to other regions, because optogenetic inhibition of the axonal terminals of SST+ CeA neurons in vlPAG recapitulated the behavioral effects of the di-synaptic circuit inhibition (**Figure 2D-F**).

Next, to selectively monitor the activity dynamics of BLAp neurons projecting onto SST+ CeA neurons during FC and memory retrieval, we used GCaMP6s-encoding RV and fiber photometry (**Figure 3, Figure S4**). We found that BLAp neurons projecting to undefined SST+

CeA neurons showed robust US responses but did not show CS responses during conditioning or retrieval (**Figure 3A-D**). In stark contrast, BLAp neurons projecting to vlPAG-projecting SST+ CeA neurons not only responded to the US but developed CS responses during FC that remained stable on retrieval the next day (**Figure 3E-J**). Finally, single-neuron resolution Ca^{2+} imaging using a miniaturized microscope revealed that target-non-defined BLAp neurons showed bi-directional CS responses, similar to observations made in anterodorsal BLA (Grewe et al., 2017) (**Figure S5**). Thus, the lack of population CS responses in the BLAp neurons projecting to the target-non-defined population of SST+ CeA neurons, reflects the heterogenous CS responses of individual BLAp neurons, while the di-synaptic target-defined BLAp subpopulation selectively undergoes learning-related plasticity.

Discussion

By combining the anatomical specificity of trans-synaptic tracing with functional recordings and optogenetic manipulations, we demonstrate that the acquisition and expression of conditioned fear memories is mediated by a di-synaptic projection linking a distinct subpopulation of BLAp neurons to the vlPAG via SST+ neurons in the CeA. Our data raise novel questions regarding upstream brain areas processing CS- and US-related information that feed into the BLAp-CeA-vlPAG pathway, and the nature of interactions between this and other neural circuits, such as the parabrachial-CeA pathway (Nagase et al., 2019; Palmiter, 2018) and a neuronal population located in the medial CeA (CeM) that exerts dis-inhibitory control over vlPAG (Haubensak et al., 2010; Tye et al., 2011). In the current study, we could not combine rabies-based GCaMP expression with the single-neuron resolution imaging due to technical difficulty (see **STAR Methods**). In the future, with improved RV with low toxicity rabies viruses, it would be an essential step to further characterize heterogeneity within mono- or di-synaptically labeled BLA subpopulation. Finally, our results indicate that functional analysis of a neuronal pathway should take into account not only the target area, but also the genetic identity (Schwarz et al., 2015) as well as the anatomical projection targets of the postsynaptic neurons.

Acknowledgements

We thank K. Miyamichi (RIKEN BDR), A. Holmes (NIH/NIAAA), and J. Fadok (Tulane) for reading and commenting on the manuscript; K. Yonehara (Aarhus, NIG) for the rabies helper plasmid design, high-titer rabies virus production protocols, and reading and commenting on the manuscript; S. Arber (FMI) for the Synaptophysin-GFP construct; F. Osakada (Nagoya) and E. Callaway (Salk) for rabies virus materials; the GENIE Project (HHMI Janelia) for making the GCaMP6s material available; E. Boyden (MIT) for making the ArchT material available; All the Lüthi lab members for discussion and support, especially T. Eichlisberger for excellent animal care; FMI animal facility, microscopy core facility (FAIM), and IT department for constant support. This work was supported by the European Research Council (ERC) under the European Union's Horizon 2020 research and innovation program (grant agreement no. 669582), and a Swiss National Science Foundation core grant (310030B_170268) (all to A.L.); and by the Novartis Research Foundation. NARSAD young investigator award to L.M.; SNSF Ambizione grant (PZ00P3_180057) to J.C.; Novartis Presidential Postdoc Fellowship to M.S.F.; EMBO (ALTF 1579-2010) to C.X.; EMBO (ALTF 914-2018) and Marie Sklodowska-Curie (grant agreement no. 843236) to N.K.

Author contributions

L.M. and A.L. initiated the project. K.M.H., N.K., and A.L. conceptualized the study. L.M performed behavioral experiments and virus-based circuit mapping with the help from J.C., C.M., and M.S.F.. N.K. and M.S.F. analyzed behavioral data. K.M.H. performed photometry experiments and analyzed the data under supervision by N.K.. L.M. performed endoscopic calcium imaging with help from J.C., K.M.H., and M.S.F.. J.H. and K.M.H. analyzed endoscopic calcium imaging data with help from J.C.. K.M.H. and C.X. produced rabies

viruses. L.M. drafted earlier versions of part of the figures. K.M.H. prepared all the figures and drafted the manuscript. K.M.H. and A.L. wrote the manuscript. All the authors commented on and finalized the manuscript and figures. A.L. supervised the entire project.

Declaration of interests
The authors declare no competing interests.

STAR Methods

CONTACT FOR REAGENT AND RESOURCE SHARING

Further information and requests for resources and reagents should be directed to and will be fulfilled by the Lead Contact, Andreas Luthi (andreas.luthi@fmi.ch).

EXPERIMENTAL MODEL AND SUBJECT DETAILS

Mice

SST-ires-Cre (Taniguchi et al., 2011), hCAR (Tallone et al., 2001), tdTomato reporter (Ai14), and wildtype C57/BL6J (Harlan/Envigo) mice were used. Genetically modified mice were backcrossed to a C57BL/6J background for at least seven generations. Mice were individually housed for at least 2 weeks before starting behavioral paradigms in open cages. Littermates of the same sex were randomly assigned to experimental groups. For behavioral experiments, only male mice (aged 2–3 months at the time of injection) were used. Male and female mice (aged 2–4 months at the time of injection) were used for rabies tracings. These analyses indicated no discernible differences between males and females. Room temperature was set at 22 °C (±2 °C) and room humidity was set at 55% (±10%). Mice were kept in a 12-h light/dark cycle with access to food and water ad libitum. Behavioral experiments were performed during the light cycle and all mouse procedures were performed in accordance with institutional guidelines at the Friedrich Miescher Institute for Biomedical Research and were approved by the Veterinary Department of the Canton of Basel-Stadt.

METHOD DETAILS

Virus preparations

The SADΔG rabies viruses were generated as described before (Osakada and Callaway, 2013; Xu et al., 2016) with a slight modification to achieve a higher titer (Wertz et al., 2015). In brief, ΔG-mCherry (Osakada et al., 2011), ΔG-GFP (Wickersham et al., 2007), ΔG-ArchT-GFP (Xu et al., 2016), and ΔG-GCaMP6s (Wertz et al., 2015) viruses were amplified from local viral stocks in B7GG cells (Baby hamster kidney cells expressing T7 RNA polymerase, rabG and histone-tagged GFP). EnvA pseudotyped rabies viruses was generated in BHK-EnvA cells. The virus was concentrated by two rounds of centrifugation, suspended in Hank's Balanced Salt Solution (GIBCO) and titered in HEK293-TVA cells (kindly provided by J. A. T. Young, Salk Institute) with serial dilutions of the virus. The titers of the EnvA pseudotyped rabies used for injections were in the range of $5 \times 10^8 – 1.0 \times 10^{10}$ infectious units/mL. Virus was stored at -80°C until further use. CAV2-Cre (Soudais et al., 2001) virus was kindly provided by E. Kremer (University of Montpellier, France). The titer was 3.1×10^{12} pp/mL. AAV.EF1a.DIO.TVA950.2A.CVS11G plasmid was a generous gift provided by K. Yonehara (Krabbe et al., 2019). It was packaged as AAV2/7 serotype at Vector BioLabs. AAV.hSyn.flex.synaptophysin-EGFP (Pecho-Vrieseling et al., 2009) was a generous gift provided by S. Arber. It was packaged as AAV2/1 serotype at Vector BioLabs.

Stereotaxic surgeries

Buprenorphine (Temgesic, Indivior UK Limited; 0.1 mg/kg BW) was injected subcutaneously 30 min prior to the surgery. Mice were anesthetized using isoflurane (5% for induction, 1-2% for maintenance; Attane, Provet) in oxygen-enriched air (Oxymat 3, Weinmann) and then head-fixed in a stereotaxic frame (Model 1900, Kopf Instruments). Lidocaine + Ropivacain (Lidocain HCl, Bichsel, 10mg/kg BW; Naropin, AstraZeneca, 3mg/kg BW) were injected subcutaneously as local anesthesia prior to incision to the skin. Postoperative pain medication included buprenorphine (0.01 mg/ml in the drinking water; overnight) and injections of meloxicam (Metacam, Boehringer Ingelheim; 5 mg/kg subcutaneously) for three days after the surgery. Eyes were protected with ophthalmic ointment (Viscotears, Alcon). Rectal body temperature of the animal was monitored and maintained at 35-37°C using a feedback-controlled heating pad (FHC) while fixed on the stereotactic frame.

Viral injections and fiber/lens implantation

A volume of 50–200 nl virus solution (depending on viral titer and area) was pressure-injected intracranially using calibrated glass pipets (5 µl microcapillary tube; Sigma-Aldrich) connected to a picospritzer III (Parker). For targeting the vlPAG, to avoid the sub-cranial midline blood sinus, craniotomy with a diameter of 0.3 mm were made bilaterally into the skull at ±1.7 mm from midline suture, and at the level of the lambda suture. The injection capillary was then slowly lowered using a hydraulic micropositioner (Kopf Instruments model 2650) at a zenith angle of 26° to the target depth of 3 mm below brain surface. Coordinates for CeA injections: AP -1.1 mm (from bregma), ML ±2.7 mm (from bregma), DV 4.2 mm (from pia); For BLAp: AP -2.18 mm (from bregma), ML ±3.4 mm (from bregma), DV 4.2 mm (from pia).

For non-cell-type-specific mono-synaptic inhibition (**Figure 1A**), CAV2-Cre and AAV2/5.flex.Arch.GFP (Penn Vector Core) were injected in the CeA and BLA, respectively. In the same surgery, optic fibers were implanted above the BLAp. Behavioral experiments were performed at earliest 3 weeks after to ensure viral expression of the opsin. For non-cell-type-specific di-synaptic inhibition (**Figure 1C**), CAV2-Cre and AAV2/7.DIO.TVA950.2A.CVS11G were injected in the vlPAG and CeA in the first surgery, respectively. 2-4 weeks later, EnvA-ΔG-ArchT-GFP or EnvA-ΔG-GFP was injected in the CeA and optic fibers were implanted above the BLAp. 2 days after the second surgery, mice were subjected to behavioral experiments. For non-cell-type-specific di-synaptic tracing (**Figure S1A**), CAV2-Cre and AAV2/7.DIO.TVA950.2A.CVS11G were injected in the vlPAG and CeA in the first surgery, respectively. 2-4 weeks later, EnvA-ΔG-mCherry was injected in the vlPAG. For mono-synaptic tracing from CeA to vlPAG (**Figure S1D**), CAV2-Cre was injected in vlPAG of hCAR::tdTomato mice. For vlPAG injections, blue beads were co-injected with CAV2-Cre to confirm the injection site.

For cell-type-specific di-synaptic manipulations (**Figure 2A, Figure S4**), AAV2/7.DIO.TVA950.2A.CVS11G was injected to the CeA of SST-ires-Cre mice. 2-4 weeks later, EnvA-ΔG-ArchT-GFP, or EnvA-ΔG-GFP was injected in the vlPAG to infect TVA-expressing axon terminals originating from SST+ neurons in CeA. Optic fibers were then implanted above the BLAp. Some EnvA-ΔG-GFP were fear conditioning with light, subjected to memory retrieval without light, and then to retrieval with light to serve as controls for both groups. For terminal inhibition of CeA (SST+) neurons (**Figure 2F**), AAV2/9.EF1a.DIO.NpHR3.3.EYFP (Penn Vector Core) or AAV2/5.flex.GFP (UNC Vector Core) was injected into the CeA and the optical fibers were placed into the vlPAG. AAV2/1.flex.Synaptophysin.GFP was used for anterograde tracing experiments (**Figure S2A**). For cell-type-specific di-synaptic tracing (**Figure S2D**), AAV2/7.DIO.TVA950.2A.CVS11G was injected to the CeA of SST-ires-Cre mice. 2-4 weeks later, EnvA-ΔG-GFP was injected in the vlPAG.

For photometry recordings (**Figure 3**), AAV2/7.DIO.TVA950.2A.CVS11G was injected to the CeA of SST-ires-Cre mice. 2-4 weeks later, EnvA-ΔG-GCaMP6s was injected in the CeA (mono-synaptic) or vlPAG (di-synaptic), and an optic fiber was unilaterally implanted above the BLAp. 7-9 days after the second surgery, recording experiments were executed.

Imaging with the miniature microscope **(Figure S5)** was attained by injecting AAV.2/5.CaMKII.GCaMP6f (Chen et al., 2013) (UPenn Vector Core) unilaterally into the BLAp. In the same surgery, a GRIN (graded index) lens with 0.6mm diameter (Inscopix) was implanted to the injection site. 3-4 weeks after surgery, when the implanted GRIN lens got stabilized in the tissue, imaging experiments were started. Since RV-based GCaMP expression could start causing toxicity and cell-death in synaptically infected neurons at around 1 week, we did not use EnvA-ΔG-GCaMP6s for miniature microscope imaging experiments.

Behavioral paradigm

Two different contexts were used; Context A (retrieval context) consisted of a clear cylindrical chamber (diameter: 23 cm) with a smooth floor, placed in a dark-walled sound attenuating chamber under dim light conditions. The chamber was scented and cleaned with 1% acetic acid. Context B (fear conditioning context) contained a clear square chamber (26.1 x 26.1 cm) with an electrical grid floor (Coulbourn Instruments) for foot shock delivery, placed in a light-coloured sound attenuating chamber with bright light conditions, and was scented and cleaned with 70% ethanol. A stimulus isolator (ISO-Flex, A.M.P.I.) was used for the delivery of direct current (DC) shock. Both chambers contained overhead speakers for delivery of auditory stimuli, which were generated using a System 3 RP2.1 real time processor and SA1 stereo amplifier with RPvdsEx Software (all Tucker-Davis Technologies). Cameras (Stingray, Allied Vision) for tracking animal behaviour were also equipped in both chambers. Radiant Software (Plexon) was used to generate precise TTL pulses to control behavioural protocols and all the TTL signals including miniscope frame timings were recorded by Plex Control Software (Plexon) to synchronize behavioural protocols and behavioural tracking. On day 0, mice were habituated for 10 min to the context A. On day 1 (fear conditioning session), mice were placed in context B, after 2 min baseline, subjected to 5 pairings of the conditioned stimulus (CS: pure tones of 7.5kHz, total duration 10 s, consisting of 200-ms pips repeated at 0.9 Hz; 75 dB sound pressure level) presented five times with the US (2 sec, DC: 0.65mA applied back-to-back after the last pip). Animals remained in the context for 1 min after the last CS presentation and were then returned to their home cage. On day 2 (memory retrieval session), after a 2-min baseline period in context A, the CS was presented eight times (ITI of 35–60 s). For reconditioning experiments, on day 3 the experimental procedure was similar to the fear conditioning session but 3kHz tone was used as CS (CS2); memory was evaluated 24h later with CS2 presentation. CS was generated with Timings of CS and US were Freezing behavior was quantified using Cineplex Editor (Plexon). The animals were considered freezing if no movement was detected for 2 s and the measure was expressed as a percentage of time spent freezing.

Optogenetic manipulations

All manipulations were performed with bilaterally implanted custom-made optic fiber connectors (FP200URT, 0.48 NA, Ø200 µm; Thorlabs). Implants were fixed to the skull using cyanoacrylate glue (Ultra Gel, Henkel) and miniature screws (P.A. Precision Screws). Dental acrylic (Paladur, Heraeus) mixed with black paint was used to seal the skull. Implanted connectors were linked to a custom-built laser bench via optic fibers during behavior sessions with optogenetic manipulations. An AOTF (AA Opto-Electronic) was used to control intensity

and timing of lasers (MBL-589, 589 nm wavelength for Arch/ArchT and NpHR; CNI Lasers, China), which was triggered by TTL generated by Radient Software (Plexon). The laser intensity was 11 – 15 mW at end of the optic fiber.

Fibre photometry recording

Recordings were performed with unilaterally implanted custom-made optic fiber connectors (FP400URT, 0.50 NA, Ø400 µm; Thorlabs). A modified Doric Fibre Photometry system (Doric) was used to perform the recordings as previously described (Hagihara et al., 2021). Briefly, two different excitation wavelengths were used (465 nm for Ca^{2+}-dependent GCaMP6s activity, and 405 nm to record an isosbestic, Ca^{2+}-independent, reference signal that serves to correct for photo-bleaching and movement-related artifacts. Data were pre-processed and analyzed using custom programs written in MATLAB (2017b, Mathworks). Data with obvious motion artifacts in the isosbestic channel were discarded. De-modulated raw Ca^{2+} traces were down-sampled to 1 kHz and then de-trended using a low-cut filter (Gaussian, cutoff, 2-4 min) to correct for slow drift of the baseline signal due to bleaching. Filtered traces were Z-scored by mean and standard error of the entire trace.

Behavioral paradigm was similar to what was described above but timing control of CS and US, video acquisition for animal behavior monitoring, and synchronization with photometry recording were achieved by custom written Python and Bonsai (Lopes et al., 2015) scripts (https://github.com/nikolaskaralis/data_suite/).

Deep-brain Ca^{2+} imaging

Mice for Ca^{2+} imaging using the miniature microscope (nVista HD, Inscopix) were prepared as previously described (Grewe et al., 2017; Hagihara et al., 2021). Imaging data were acquired using nVista HD software (Inscopix) at a frame rate of 20 Hz. Time stamps of imaging frames and behavioral coordinates were collected for alignment using the Omniplex data acquisition system (Plexon), and imaging and video recording was triggered by Radiant (Plexon).

Data analysis was performed using custom codes written in MATLAB (2017b, Mathworks). Translational motion correction was performed by manually selection of two regions of interest (ROI). To cope with the high background noise, imaging files were pre-processed by subtracting a Gaussian blurred image on a frame-by-frame basis. Motion correction was performed using FFT based Image registration (Guizar-Sicairos et al., 2008). A template was generated by registering the first 100 frames in the first ROI to the first frame and subsequently registering all images to the median image of the first 100 frames in the first ROI. This process was repeated until the applied motion fell under a specified value, typically less than 0.01 average pix shift on all frames. Motion correction was then repeated on the second defined ROI, to ensure that no (or only little) non-rigid motion was present in the recorded images. To avoid any interference with the subsequent extraction of calcium traces, the calculated shifts were applied to the raw data and performed subsequent analysis with the motion corrected raw data.

Each session was processed independently and CNMF-E (Zhou et al., 2018) was used for automatic neuron extraction. Parameters were set to avoid false negatives at the cost of false positives, which were excluded through automated selection and visual inspection. ROIs were excluded if were too small (<~0.6% of pixels), too big (>~1.4% of pixels) or too close to the edge of the field of view (FOV). In addition, neurons that exhibited low SN ratios and overlapped at least 60% with other neurons were excluded from the analysis. Only ROIs that had coherent shape, exhibiting round or slightly elongated contours and that show clearly

defined Ca^{2+} transients, consistent with the biophysical properties of GCaMP were included in the analysis.

To identify cells that showed CS evoked activity, we calculated intra-day plasticity during the fear conditioning session by checking whether the average activity during CS presentation of Trials 4 to 5 was higher than the average activity during Trials 1 to 3 after adding 2*standard deviation. For the retrieval Session, the same criterion was applied; here the comparison was between the baseline period and the average of Trials 1-5. For visualization purposes, calcium traces in **Figure S5** were baselined to the mean of the 10 s preceding the CS presentation.

Histology

After completion of the behavioral or tracing experiments, mice were transcardially perfused with 4% PFA in PBS. For experiments involving rabies, perfusion was performed 5-8 days after injections. Brains were post-fixed in PFA overnight at 4 °C, cut with a VT1000S vibratome (Leica) with 80-120µm thickness, and imaged with AxioScan, Axioimager Z1, or LSM700 microscopes (Zeiss). The fiber tip positions, virus injection sites, and GRIN lens implantation sites were mapped against the mouse brain atlas (Paxinos and Franklin, 2001). To identify starter neurons, sections were incubated with primary rabbit anti-2A peptide antibody (1:500; Merck Millipore, ABS31, lot no. 2746420) in 0.5% Triton X-100 in PBS for 48h at 4 °C. Samples were rinsed with 0.1% Triton X-100 in PBS three times and then incubated overnight at 4 °C with donkey anti-rabbit Alexa Fluor 568 (1:750; Termo Fisher Scientifc, A10042, lot no. 1757124) or donkey anti-rabbit Alexa Fluor 647 (1:750; Termo Fisher Scientifc, A31573, lot no. 1786284). Finally, sections were washed four times with PBS, mounted on glass slides and coverslipped. With a few exceptions, slices were stained with DAPI to facilitate area identification.

QUANTIFICATION AND STATISTICAL ANALYSIS

All data are expressed as the mean ± standard error of the mean (SEM), unless stated otherwise. Box plots represent the median and 25th and 75th percentiles, and their whiskers represent the data range. In some of the plots, outlier values are not shown for clarity of presentation, but all data points and animals were always included in the statistical analysis. Two-sided Wilcoxon rank-sum test was used to compare two independent groups. For paired comparison, we used paired-t test. Dunnett test was performed when more than two groups were compared against a control group. Throughout the study, $P < 0.05$ was considered statistically significant. No statistical methods were used to pre-determine sample sizes, but our sample sizes are similar to those generally employed in the field. Freezing scoring for optogenetic manipulation experiments was performed blindly to experimental conditions.

DATA AND SOFTWARE AVAILABILITY

Custom-written codes used to analyse data from this study are available upon reasonable request from the corresponding authors. The data that support the findings of this study will be available at: https://data.fmi.ch/PublicationSupplementRepo/

Supplemental Notes

In the experiments shown in **Figure 2** and **Figure 3**, where SST-Cre mice were used for di-synaptic tracing, our current virus combination design does not fully guarantee that only vlPAG-projecting SST+ CeA neurons serve as starter neurons for trans-synaptic rabies infection of BLAp neurons. Since there is local connectivity among SST+ neurons in the CeA (Hunt et al., 2017), rabies viruses infecting axon terminals of SST+ CeA neurons in the vlPAG could also infect connected SST+ CeA neurons that do not project to vlPAG. As those secondarily infected CeA neurons are also transduced with TVA and G, they could, in turn, act as unintentional starter neurons for multi-synaptic labeling of BLAp neurons. Nevertheless, we think this potential pseudo-mono-synaptic labeling does not confound our findings for the following reasons.

First, we find relatively sparse rabies positive neurons in the CeA and do not see dense overlap between 2A+ neurons and rabies positive neurons in the CeA, suggesting that starter neurons are largely restricted to primarily infected vlPAG projecting SST+ neurons. This is consistent with the previous finding that only a fraction (approx. 30%) of SST+ CeA neurons project to vlPAG (Penzo et al., 2014). Second, because synaptic connections between SST+ CeA neurons are inhibitory, a substantial contribution of tri- (or more) synaptic labeling would not be consistent with the effect of optogenetic manipulations of the SST+ di-synaptic pathway on behavior. Instead, we found that optogenetic manipulations of the SST+ disynaptic pathway had the same behavioral effect (**Figure 2)** as non-cell-type-specific di-synaptic manipulations (**Figure 1**), where starter neurons can not be pseudo, thus excluding the above-mentioned scenario. Lastly, if there were frequent local trans-synaptic infections among SST+ CeA neurons, virtually the same populations in the CeA and BLA would be infected regardless of rabies injection site – CeA-targeted or vlPAG-targeted. However, we see different spatial distributions between the two cohorts in labeled BLAp neurons. Finally, photometry experiments showed clear differences in activity patterns between the mono-synaptically labeled and the di-synaptically labeled BLAp populations (**Figure 3**). Thus, even though we cannot completely exclude the contribution of tri- (or more) synaptic labeling, our experimental strategy is sufficient to characterize the specificity of the BLAp-CeA(SST+)-vlPAG di-synaptic pathway.

Fig1. Di-synaptic specificy of BLP->CeA->vlPAG pathway for fear memory formation

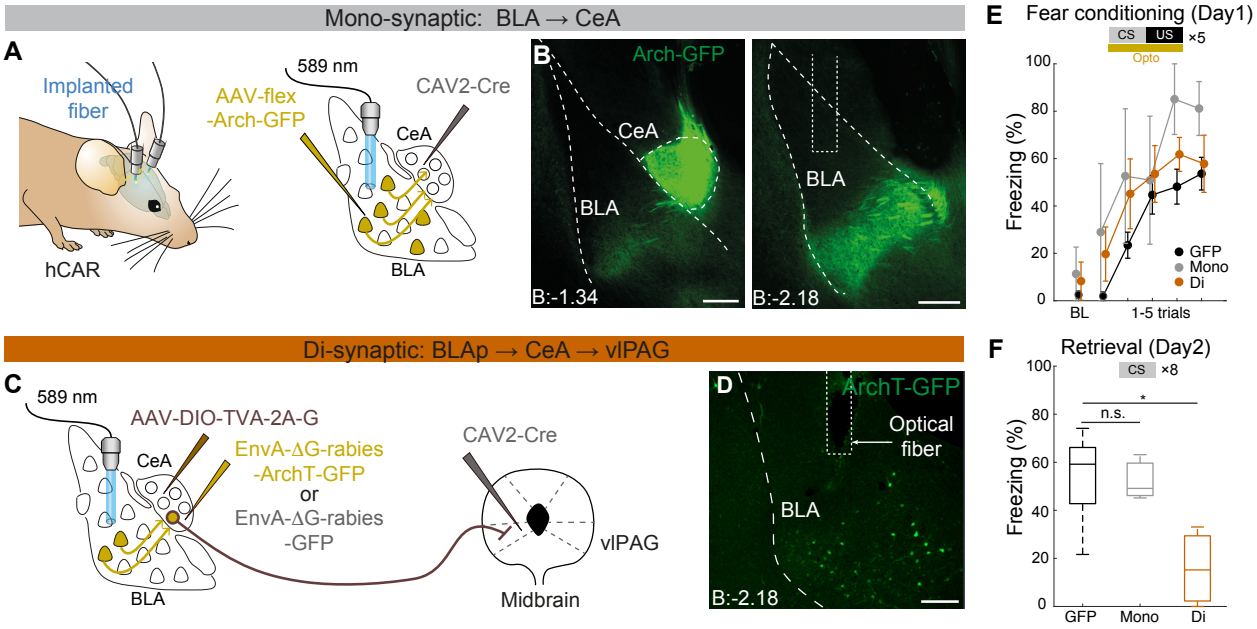

Figure 1 | Di-synaptic specificity of BLAp→CeA→vlPAG pathway for fear memory formation
A. Scheme illustrating viral injection strategy to express Arch in neurons projecting from BLA to CeA. CAV2-Cre was injected to CeA, and then AAV-flex-Arch-GFP was injected to BLA. Optic fibers were bilaterally implanted to target labelled BLA neurons. hCAR mice were used to facilitate transduction by CAV2 viruses.
B. Histology of injection sites; (Top) CeA; (Bottom) BLA; Scale bar:250μm
C. Scheme illustrating viral injection strategy to express ArchT in neurons projecting from BLAp to CeA-vlPAG-pathway. CAV2-Cre was injected to vlPAG and AAV-DIO-TVA-2A-G to CeA in hCAR mice. Three days before fear conditioning, rabies-ArchT-GFP or rabies-GFP was injected to CeA. Optic fibers were bilaterally implanted to target posterolateral BLA neurons.
D. Histology of injection sites; (Top) vlPAG; (Bottom) BLA; Scale bar:200μm
E. Average freezing levels (mean ± SEM) during auditory fear conditioning (Day1). Optical manipulation was applied to cover CS+US periods. The 2-min baseline (BL) before the first CS presentation followed by the freezing levels during each CS presentation (1-5 trial). N = 13, 3, 7 mice for GFP, Mono, and Di, respectively.
F. Average freezing levels (mean ± SEM) during 8 CS presentations in fear memory retrieval (Day2). *: P = 0.0001; n.s.: P = 0.99; Dunnett test. See **Figure S1,2.**

Fig2. SST+

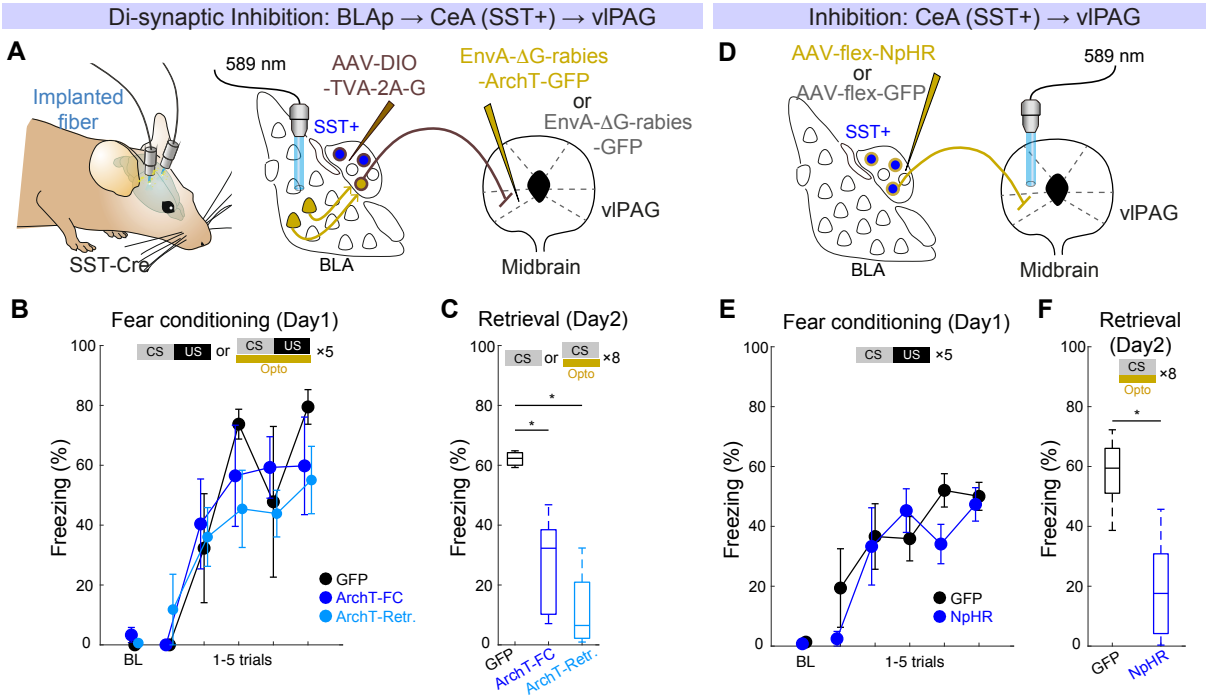
Di-synaptic Inhibition: BLAp → CeA (SST+) → vlPAG
Inhibition: CeA (SST+) → vlPAG
A
Implanted fiber
589 nm
AAV-DIO -TVA-2A-G
SST+
EnvA-ΔG-rabies -ArchT-GFP
or
EnvA-ΔG-rabies -GFP
vlPAG
SST-Cre
BLA
Midbrain
D
AAV-flex-NpHR
or
AAV-flex-GFP
SST+
589 nm
vlPAG
BLA
Midbrain
B
Fear conditioning (Day1)
CS US or CS US ×5
Opto
Freezing (%)
GFP
ArchT-FC
ArchT-Retr.
BL
1-5 trials
C
Retrieval (Day2)
CS or CS ×8
Opto
Freezing (%)
GFP
ArchT-FC
ArchT-Retr.
E
Fear conditioning (Day1)
CS US ×5
Freezing (%)
GFP
NpHR
BL
1-5 trials
F
Retrieval (Day2)
CS ×8
Opto
Freezing (%)
GFP
NpHR

Figure 2 | SST+ CeA neurons connect BLAp to vlPAG

A. Scheme illustrating viral injection strategy to express ArchT in neurons projecting from BLAp to CeA(SST+)-vlPAG-pathway. AAV-DIO-TVA-2A-G was injected to CeA in SST-Cre mice, then rabies-ArchT-GFP or rabies-GFP was injected to vlPAG. Optic fibers were bilaterally implanted to target BLAp. Experimental animals underwent optogenetic manipulations during either fear conditioning (ArchT-FC) or retrieval (Arch-Retrieval). GFP controls had the laser both during fear conditioning and retrieval. Optogenetic manipulations were performed to temporally cover CS+US or CS presentations.

B. Average freezing levels (mean ± SEM) during auditory fear conditioning (Day1). The 2 min baseline (BL) before the first CS presentation followed by the freezing levels during each CS presentation (1-5 trial). For the ArchT-FC group, optical manipulation was applied to cover CS+US periods during FC but not during CS presentation during retrieval. In contrast, for the ArchT-Retrieval group, optical manipulation was applied to cover CS periods during retrieval but not during CS+US presentation during FC. N = 3, 5, 4 for GFP, ArchT-FC, and ArchT-Retrieval, respectively.

C. Average freezing levels (mean ± SEM) during 8 CS presentations in fear memory retrieval (Day2). ArchT-FC vs GFP: P = 0.012; ArchT-Retrival vs GFP: P = 0.002; Dunnett test.

D. Scheme illustrating viral injection strategy to express ArchT in CeA(SST+) neurons. AAV-flex-NpHR was injected to CeA in SST-Cre mice. Optic fibers were bilaterally implanted to target vlPAG.

E. Average freezing levels (mean ± SEM) during auditory fear conditioning (Day1) without optogenetic manipulation. N = 5, 8 for GFP and SST-NpHR, respectively.

F. Average freezing levels (mean ± SEM) during 8 CS presentations in fear memory retrieval (Day2). Optogenetic manipulations were performed to temporally cover CS presentations. *: P = 0.0031; rank-sum test. See **Figure S3**.

Fig3. BLP->CeA->vlPAG pathway exibits fear-related activity

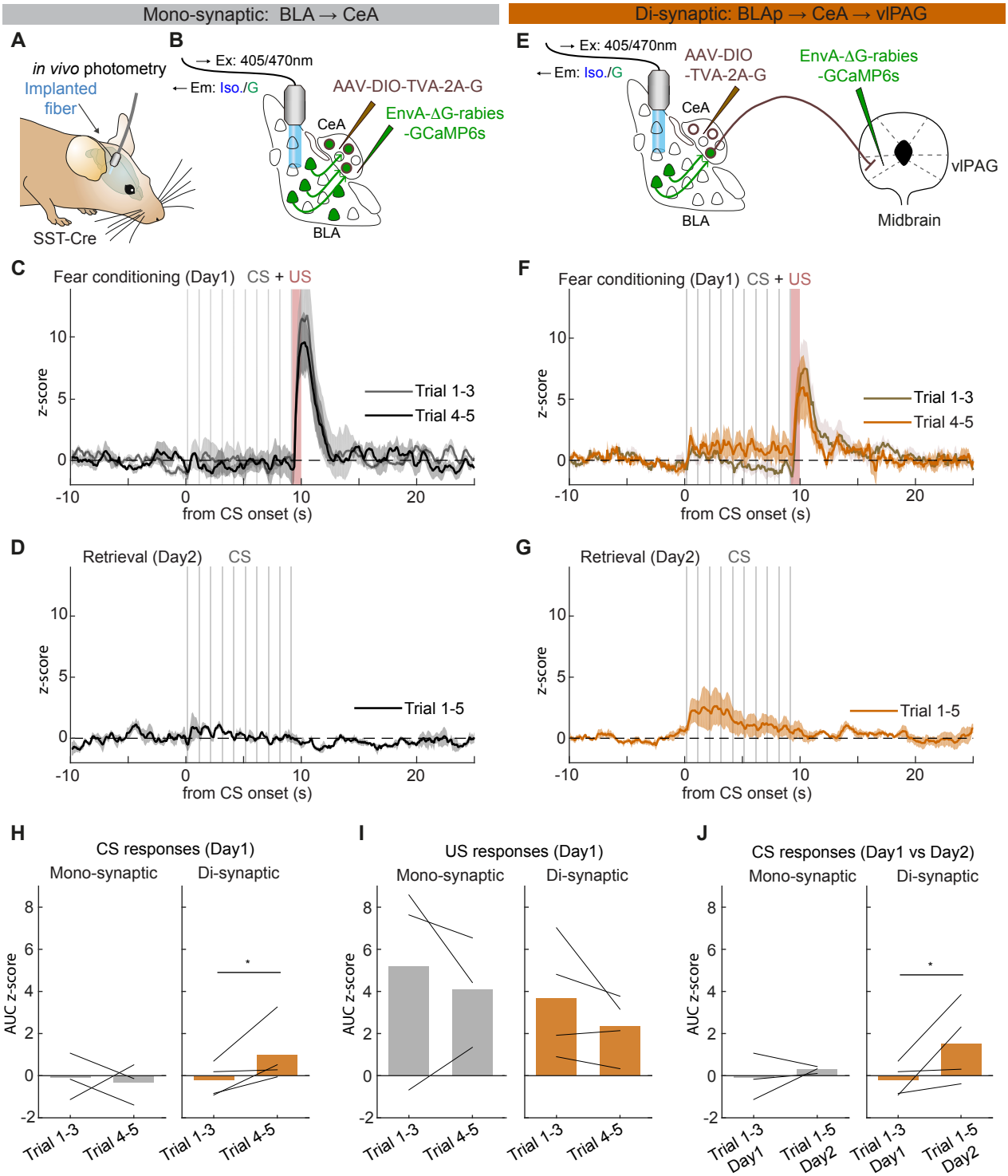

Figure 3 | BLAp neurons that di-synaptically connect vlPAG show learning-related change in CS responses

A, B. Scheme illustrating viral injection strategy to express GCaMP6s in neurons projecting from BLA to CeA. AAV-DIO-TVA-2A-G was injected to CeA in SST-Cre mice, then rabies-GCaMP6s was injected to CeA. Optic fibers were unilaterally implanted to target labelled posterior BLA neurons.

C,D. Averaged z-scored photometry traces on Day1 (**C**) or on Day2 (**D**) from mono-synaptically labeled mice. Mean ± SEM.

E. Scheme illustrating viral injection strategy to express GCaMP6s in neurons projecting from BLAp to CeA(SST+)-vlPAG-pathway. AAV-DIO-TVA-2A-G was injected to CeA in SST-Cre mice, then rabies-GCaMP6s was injected to vlPAG instead of CeA. Optic fibers were bilaterally implanted to target GCaMP6s expressing BLAp neurons.

F,G. Averaged z-scored photometry traces on Day1 (**F**) or on Day2 (**G**) from di-synaptically labeled mice. Mean ± SEM.

H-J. Summary of responses to CS and US. Early (1-3 trials) vs late (4-5 trials) responses on Day1 to CS (**H**) or US (**I**). CS responses Day1 vs Day2 (**J**). *: P = 0.038 (**H**); P = 0.048 (**J**); paired-t test. See **Figure S4,5.**

Ext Data Fig. 1 Histology

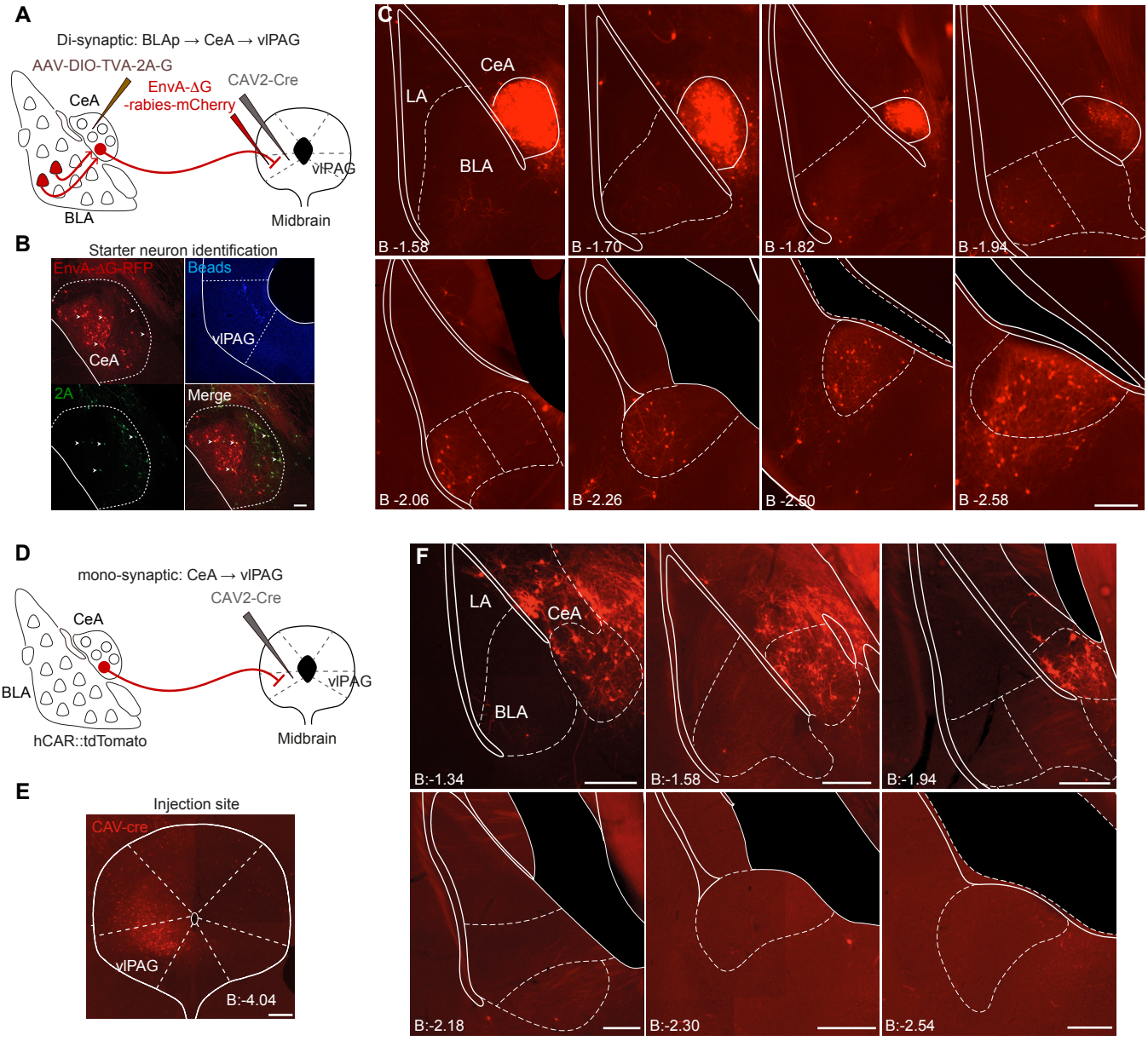

Figure S1 | Di-synaptic connectivity from BLA to vlPAG. Related to Figure 1.
A. Scheme illustrating viral injection strategy to express RFP in neurons projecting from BLA to CeA-vlPAG-pathway. CAV2-Cre was injected to vlPAG and AAV-DIO-TVA-2A-G in CeA in hCAR mice. Then, rabies-RFP was injected to vlPAG.
B. Injection sites, CeA and vlPAG. vlPAG injections were marked by co-injecting blue-beads. Starter neurons in the CeA was identified with immunohistochemistry for 2A. Scale bar: 50μm
C. Serial visualization of rabies labeled neurons in the amygdala. Scale bar: 250μm
D. Scheme illustrating viral injection strategy to label neurons directly projecting vlPAG. CAV2-Cre was injected to vlPAG in hCAR × tdTomato-reporter mice.
E. Injection site, vlPAG. Scale bar: 50μm
F. Serial visualization of labeled neurons in the amygdala. Unlike CeA, BLA neurons do not directly project to vlPAG.
Scale bar: 250μm

Ext Data Fig. 2 Reconditioning

A

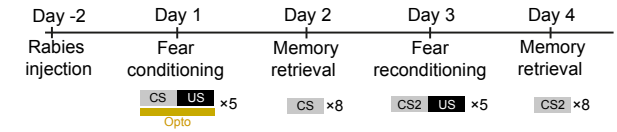

B

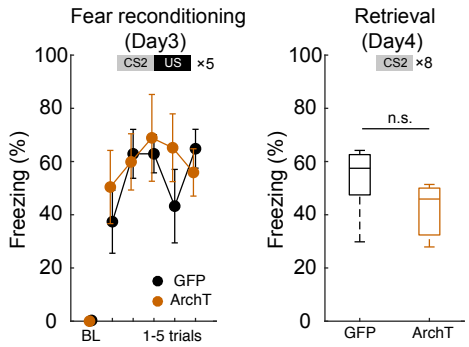

C

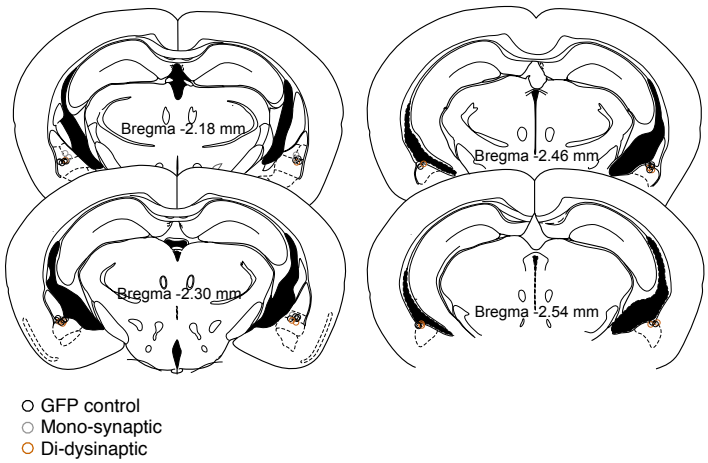

Figure S2 | Reconditioning. Related to Figure 1.
A. Experimental schedule of reconditioning experiments. After the initial fear conditioning and memory retrieval on Day1 and Day2, mice were again fear conditioned using a novel CS – CS2.
B. Left: Average freezing levels (mean ± SEM) during reconditioning (Day3). The 2 min baseline (BL) before the first CS presentation followed by the freezing levels during each CS presentation (1-5 trial). N = 7,3 for GFP and ArchT, respectively. n.s.: P = 0.18; rank-sum test.
Right: Average freezing levels (mean ± SEM) during 8 times of CS2 presentation in fear memory retrieval (Day4).
C. Optical fiber placements for experiments shown in **Figure 1**.

Ext Data Fig. 3 Histology for SST+

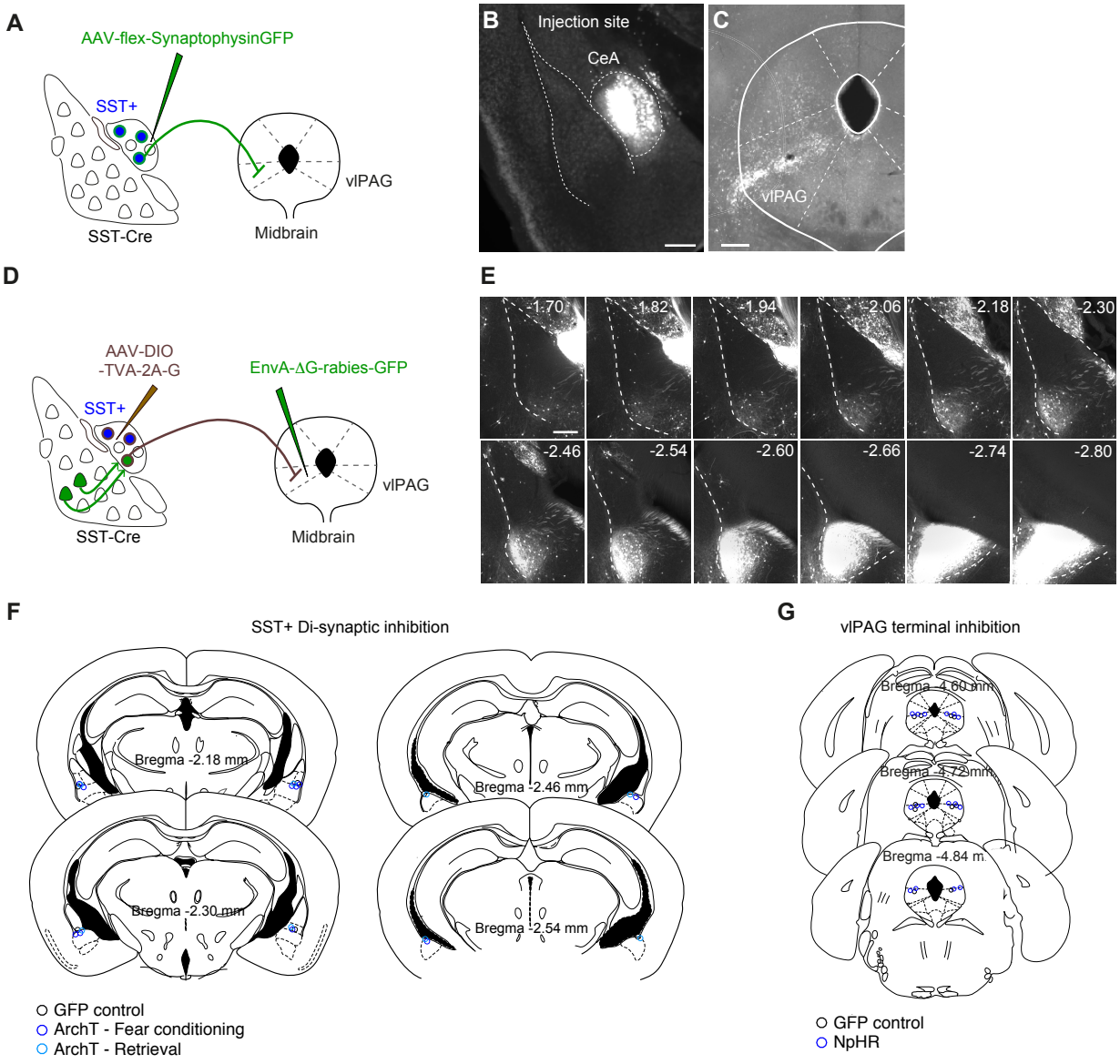

Figure S3 | SST+ CeA neurons connect BLA to vlPAG. Related to Figure 2.
A. Scheme illustrating viral injection strategy to express Synaptophysin-GFP in SST+ CeA neurons for axon terminal visualization.
B. Injection site, CeA.
C. SST+ CeA neurons project their axons to vlPAG. Scale bar: 250µm
D. Scheme illustrating viral injection strategy to express GFP in neurons projecting from BLA to CeA(SST+)-vlPAG-pathway. AAV-DIO-TVA-2A-G was injected to CeA in SST-Cre mice. Then, rabies-GFP was injected to vlPAG.
E. Serial visualization of labeled neurons in the amygdala. Similar to **Figure S1C**, labeled neurons were preferentially found in posterolateral BLA. Scale bar: 250µm
F,G. Optical fiber placements for experiments shown in **Figure 2**.

Ext Data Fig. 4 Additional data for fiber photometry

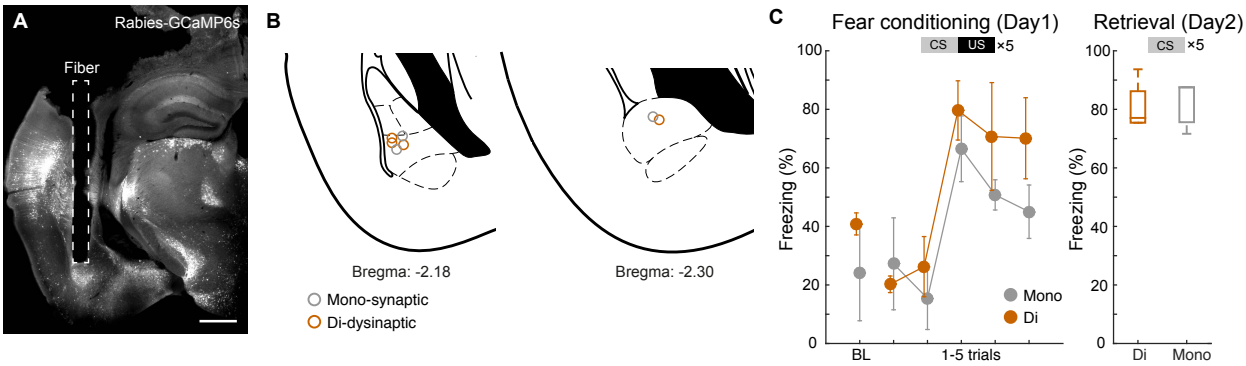

Figure S4 | Additional data for fiber photometry recordings. Related to Figure 3.
A. An example histological confirmation of the fiber implantation site.
B. Fiber placements.
C. Left: Average freezing levels (mean ± SEM) of implanted animals during conditioning (Day1). The 2 min baseline (BL) before the first CS presentation followed by the freezing levels during each CS presentation (1-5 trial). Right: Average freezing levels (mean ± SEM) during 5 CS presentations in fear memory retrieval (Day2). N = 4, 3 mice for Di and Mono, respectively.

Ext Data Fig. 5 Endoscopic imaging reveals heterogeneous activity in posterolateral BLA

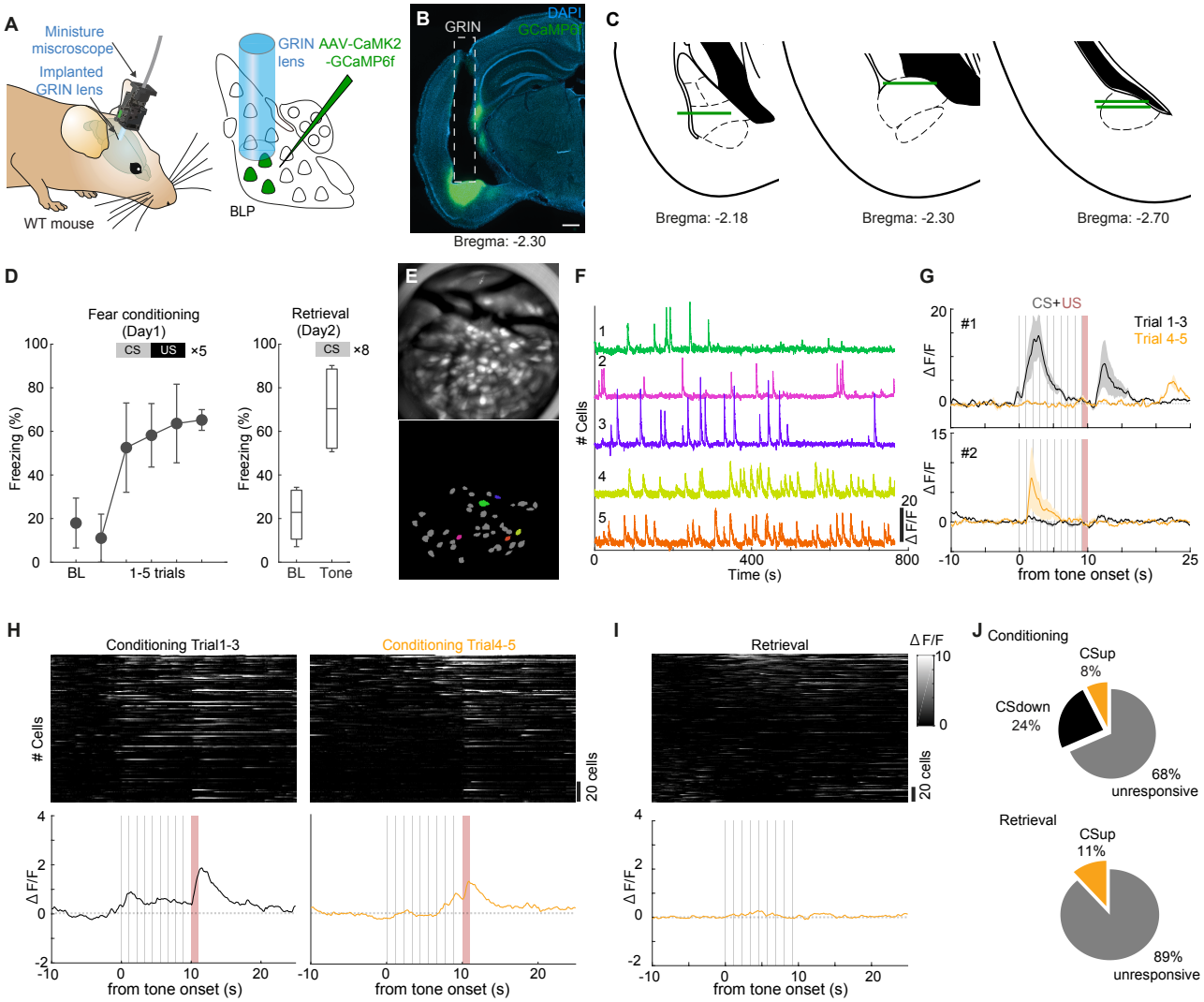

Figure S5 l Cellular resolution calcium imaging revealed heterogeneous CS responses in posterolateral BLA neurons. Related to Figure 3.

A. Scheme illustrating viral injection strategy to express GCaMP6f in neurons in posterolateral BLA. AAV-CaMK2-GCaMP6f was injected to BLA in BL6 WT mice, and then a GRIN lens was implanted targeting posterolateral BLA.

B. An example histological confirmation of the GRIN implantation site. **C.** GRIN lens placements.

D. Left: Average freezing levels (mean ± SEM) of implanted animals during conditioning (Day1). The 2 min baseline (BL) before the first CS presentation followed by the freezing levels during each CS presentation (1-5 trial). Right: Average freezing levels (mean ± SEM) during 8 CS presentations in fear memory retrieval (Day2). N = 4 mice.

E. Top: An example maximum intensity projection image of miniscope imaging. Bottom: Corresponding cell masks detected. **F**. Five example calcium traces of neurons in **E** (color matched) in the entire retrieval session (Day 2). **G.** #1 and #2 in **F**, showing intra session changes in CS responses – CSdown and CSup (see **STAR Methods**), respectively. **H.I.** Responses of all recorded neurons show highly heterogeneous CS representations both during conditioning (**H**) and retrieval (**I**). **J.** Fraction of CSup and CSdown neurons during conditioning (top) and retrieval (bottom) sessions.

4. Acknowledgements

I am grateful to all the particles existing in the universe, in particular, to ones currently and previously composing human being, in particular, my family, friends, and colleagues.

5. References

For Introduction

Adhikari, A., Lerner, T.N., Finkelstein, J., Pak, S., Jennings, J.H., Davidson, T.J., Ferenczi, E., Gunaydin, L.A., Mirzabekov, J.J., Ye, L., et al. (2015). Basomedial amygdala mediates top-down control of anxiety and fear. Nature *527*, 179–185.

Amano, T., Unal, C.T., and Paré, D. (2010). Synaptic correlates of fear extinction in the amygdala. Nat. Neurosci. *13*, 489–494.

Amano, T., Duvarci, S., Popa, D., and Paré, D. (2011). The fear circuit revisited: contributions of the basal amygdala nuclei to conditioned fear. J. Neurosci. *31*, 15481–15489.

Amir, A., Amano, T., and Pare, D. (2011). Physiological identification and infralimbic responsiveness of rat intercalated amygdala neurons. J. Neurophysiol. *105*, 3054–3066.

An, B., Kim, J., Park, K., Lee, S., Song, S., and Choi, S. (2017). Amount of fear extinction changes its underlying mechanisms. Elife *6*.

Asede, D., Bosch, D., Lüthi, A., Ferraguti, F., and Ehrlich, I. (2015). Sensory inputs to intercalated cells provide fear-learning modulated inhibition to the basolateral amygdala. Neuron *86*, 541–554.

Atasoy, D., Aponte, Y., Su, H.H., and Sternson, S.M. (2008). A FLEX switch targets Channelrhodopsin-2 to multiple cell types for imaging and long-range circuit mapping. J. Neurosci. *28*, 7025–7030.

Baek, J., Lee, S., Cho, T., Kim, S.-W., Kim, M., Yoon, Y., Kim, K.K., Byun, J., Kim, S.J., Jeong, J., et al. (2019). Neural circuits underlying a psychotherapeutic regimen for fear disorders. Nature *566*, 339–343.

Berretta, S., Pantazopoulos, H., Caldera, M., Pantazopoulos, P., and Paré, D. (2005). Infralimbic cortex activation increases c-Fos expression in intercalated neurons of the amygdala. Neuroscience *132*, 943–953.

Beyeler, A., Namburi, P., Glober, G.F., Simonnet, C., Calhoon, G.G., Conyers, G.F., Luck, R., Wildes, C.P., and Tye, K.M. (2016). Divergent Routing of Positive and Negative Information from the Amygdala during Memory Retrieval. Neuron *90*, 348–361.

Bi, G.Q., and Poo, M.M. (1998). Synaptic modifications in cultured hippocampal neurons: dependence on spike timing, synaptic strength, and postsynaptic cell type. J. Neurosci. *18*, 10464–10472.

Bienvenu, T.C.M., Busti, D., Micklem, B.R., Mansouri, M., Magill, P.J., Ferraguti, F., and Capogna, M. (2015). Large intercalated neurons of amygdala relay noxious sensory information. J. Neurosci. *35*, 2044–2057.

Blaesse, P., Goedecke, L., Bazelot, M., Capogna, M., Pape, H.-C., and Jüngling, K. (2015). μ-Opioid Receptor-Mediated Inhibition of Intercalated Neurons and Effect on Synaptic Transmission to the Central Amygdala. J. Neurosci. *35*, 7317–7325.

Blanchard, D.C., and Blanchard, R.J. (1972). Innate and conditioned reactions to threat in rats with amygdaloid lesions. J. Comp. Physiol. Psychol. *81*, 281–290.

Bocchio, M., Fisher, S.P., Unal, G., Ellender, T.J., Vyazovskiy, V.V., and Capogna, M. (2016). Sleep and Serotonin Modulate Paracapsular Nitric Oxide Synthase Expressing Neurons of the Amygdala. ENeuro *3*.

Bouton, M.E. (1993). Context, time, and memory retrieval in the interference paradigms of Pavlovian learning. Psychol. Bull. *114*, 80–99.

Brown, S., and Schafer, E.A. (1888). An Investigation into the Functions of the Occipital and Temporal Lobes of the Monkey's Brain. Philos. Trans. R. Soc. Lond. B Biol. Sci. *179*, 303.

Busti, D., Geracitano, R., Whittle, N., Dalezios, Y., Mańko, M., Kaufmann, W., Sätzler, K., Singewald, N., Capogna, M., and Ferraguti, F. (2011). Different fear states engage distinct networks within the intercalated cell clusters of the amygdala. J. Neurosci. *31*, 5131–5144.

Callaway, E.M. (2008). Transneuronal circuit tracing with neurotropic viruses. Curr. Opin. Neurobiol. *18*, 617–623.

Campeau, S., and Davis, M. (1995a). Involvement of the central nucleus and basolateral complex of the amygdala in fear conditioning measured with fear-potentiated startle in rats trained concurrently with auditory and visual conditioned stimuli. J. Neurosci. *15*, 2301–2311.

Campeau, S., and Davis, M. (1995b). Involvement of subcortical and cortical afferents to the lateral nucleus of the amygdala in fear conditioning measured with fear- potentiated startle in rats trained concurrently with auditory and visual conditioned stimuli. J. Neurosci. *15*, 2312–2327.

Chan, K.Y., Jang, M.J., Yoo, B.B., Greenbaum, A., Ravi, N., Wu, W.-L., Sánchez-Guardado, L., Lois, C., Mazmanian, S.K., Deverman, B.E., et al. (2017). Engineered AAVs for efficient noninvasive gene delivery to the central and peripheral nervous systems. Nat. Neurosci. *20*, 1172–1179.

Chen, F., Wassie, A.T., Cote, A.J., Sinha, A., Alon, S., Asano, S., Daugharthy, E.R., Chang, J.-B., Marblestone, A., Church, G.M., et al. (2016). Nanoscale imaging of RNA with expansion microscopy. Nat. Methods *13*, 679–684.

Chen, T.-W., Wardill, T.J., Sun, Y., Pulver, S.R., Renninger, S.L., Baohan, A., Schreiter, E.R., Kerr, R.A., Orger, M.B., Jayaraman, V., et al. (2013). Ultrasensitive fluorescent proteins for imaging neuronal activity. Nature *499*, 295–300.

Cho, J.-H., Deisseroth, K., and Bolshakov, V.Y. (2013). Synaptic encoding of fear extinction in mPFC-amygdala circuits. Neuron *80*, 1491–1507.

Chung, K., Wallace, J., Kim, S.-Y., Kalyanasundaram, S., Andalman, A.S., Davidson, T.J., Mirzabekov, J.J., Zalocusky, K.A., Mattis, J., Denisin, A.K., et al. (2013). Structural and molecular interrogation of intact biological systems. Nature *497*, 332–337.

Ciocchi, S., Herry, C., Grenier, F., Wolff, S.B.E., Letzkus, J.J., Vlachos, I., Ehrlich, I., Sprengel, R., Deisseroth, K., Stadler, M.B., et al. (2010). Encoding of conditioned fear in central amygdala inhibitory circuits. Nature *468*, 277–282.

Citri, A., and Malenka, R.C. (2008). Synaptic plasticity: multiple forms, functions, and mechanisms. Neuropsychopharmacology *33*, 18–41.

Clem, R.L., and Schiller, D. (2016). New Learning and Unlearning: Strangers or Accomplices in Threat Memory Attenuation? Trends Neurosci. *39*, 340–351.

Collins, D.R., and Paré, D. (1999). Spontaneous and evoked activity of intercalated amygdala neurons. Eur. J. Neurosci. *11*, 3441–3448.

Craske, M.G., Stein, M.B., Eley, T.C., Milad, M.R., Holmes, A., Rapee, R.M., and Wittchen, H.-U. (2017). Anxiety disorders. Nature Reviews Disease Primers *3*, 1–19.

Daigle, T.L., Madisen, L., Hage, T.A., Valley, M.T., Knoblich, U., Larsen, R.S., Takeno, M.M., Huang, L., Gu, H., Larsen, R., et al. (2018). A Suite of Transgenic Driver and Reporter Mouse Lines with Enhanced Brain-Cell-Type Targeting and Functionality. Cell *174*, 465-480.e22.

Dana, H., Mohar, B., Sun, Y., Narayan, S., Gordus, A., Hasseman, J.P., Tsegaye, G., Holt, G.T., Hu, A., Walpita, D., et al. (2016). Sensitive red protein calcium indicators for imaging neural activity. Elife *5*, e12727.

Dana, H., Sun, Y., Mohar, B., Hulse, B.K., Kerlin, A.M., Hasseman, J.P., Tsegaye, G., Tsang, A., Wong, A., Patel, R., et al. (2019). High-performance calcium sensors for imaging activity in neuronal populations and microcompartments. Nat. Methods *16*, 649–657.

Davis, M. (1992). The role of the amygdala in fear and anxiety. Annu. Rev. Neurosci. *15*, 353–375.

Davis, P., Zaki, Y., Maguire, J., and Reijmers, L.G. (2017). Cellular and oscillatory substrates of fear extinction learning. Nat. Neurosci. *20*, 1624–1633.

Denk, W., Strickler, J.H., and Webb, W.W. (1990). Two-photon laser scanning fluorescence microscopy. Science *248*, 73–76.

Deverman, B.E., Pravdo, P.L., Simpson, B.P., Kumar, S.R., Chan, K.Y., Banerjee, A., Wu, W.-L., Yang, B., Huber, N., Pasca, S.P., et al. (2016). Cre-dependent selection yields AAV variants for widespread gene transfer to the adult brain. Nat. Biotechnol. *34*, 204–209.

Dong, J.Y., Fan, P.D., and Frizzell, R.A. (1996). Quantitative analysis of the packaging capacity of recombinant adeno-associated virus. Hum. Gene Ther. *7*, 2101–2112.

Duvarci, S., and Pare, D. (2014). Amygdala microcircuits controlling learned fear. Neuron *82*, 966–980.

Flusberg, B.A., Nimmerjahn, A., Cocker, E.D., Mukamel, E.A., Barretto, R.P.J., Ko, T.H., Burns, L.D., Jung, J.C., and Schnitzer, M.J. (2008). High-speed, miniaturized fluorescence microscopy in freely moving mice. Nat. Methods *5*, 935–938.

Geracitano, R., Kaufmann, W.A., Szabo, G., Ferraguti, F., and Capogna, M. (2007). Synaptic heterogeneity between mouse paracapsular intercalated neurons of the amygdala. J. Physiol. *585*, 117–134.

Gerfen, C.R., Paletzki, R., and Heintz, N. (2013). GENSAT BAC cre-recombinase driver lines to study the functional organization of cerebral cortical and basal ganglia circuits. Neuron *80*, 1368–1383.

Ghosh, K.K., Burns, L.D., Cocker, E.D., Nimmerjahn, A., Ziv, Y., Gamal, A.E., and Schnitzer, M.J. (2011). Miniaturized integration of a fluorescence microscope. Nat. Methods *8*, 871–878.

Goddard, G.V. (1964). Functions of the amygdala. Psychol. Bull. *62*, 89–109.

Gregoriou, G.C., Kissiwaa, S.A., Patel, S.D., and Bagley, E.E. (2019). Dopamine and opioids inhibit synaptic outputs of the main island of the intercalated neurons of the amygdala. Eur. J. Neurosci. *50*, 2065–2074.

Grewe, B.F., Gründemann, J., Kitch, L.J., Lecoq, J.A., Parker, J.G., Marshall, J.D., Larkin, M.C., Jercog, P.E., Grenier, F., Li, J.Z., et al. (2017). Neural ensemble dynamics underlying a long-term associative memory. Nature *543*, 670–675.

Gu, H., Marth, J.D., Orban, P.C., Mossmann, H., and Rajewsky, K. (1994). Deletion of a DNA polymerase beta gene segment in T cells using cell type-specific gene targeting. Science *265*, 103–106.

Haggerty, D.L., Grecco, G.G., Reeves, K.C., and Atwood, B. (2020). Adeno-Associated Viral Vectors in Neuroscience Research. Mol Ther Methods Clin Dev *17*, 69–82.

Haubensak, W., Kunwar, P.S., Cai, H., Ciocchi, S., Wall, N.R., Ponnusamy, R., Biag, J., Dong, H.-W., Deisseroth, K., Callaway, E.M., et al. (2010). Genetic dissection of an amygdala microcircuit that gates conditioned fear. Nature *468*, 270–276.

Hebb, D.O. (1949). The organization of behavior; a neuropsychological theory. Https://Psycnet.Apa.Org › Recordhttps://Psycnet.Apa.Org › Record *335*.

Hefner, K., Whittle, N., Juhasz, J., Norcross, M., Karlsson, R.-M., Saksida, L.M., Bussey, T.J., Singewald, N., and Holmes, A. (2008). Impaired fear extinction learning and cortico-amygdala circuit abnormalities in a common genetic mouse strain. J. Neurosci. *28*, 8074–8085.

Helmchen, F., Fee, M.S., Tank, D.W., and Denk, W. (2001). A Miniature Head-Mounted Two-Photon Microscope: High-Resolution Brain Imaging in Freely Moving Animals. Neuron *31*, 903–912.

Herkenham, M., and Pert, C.B. (1982). Light microscopic localization of brain opiate receptors: a general autoradiographic method which preserves tissue quality. J. Neurosci. *2*, 1129–1149.

Herry, C., and Johansen, J.P. (2014). Encoding of fear learning and memory in distributed neuronal circuits. Nat. Neurosci. *17*, 1644–1654.

Herry, C., Ciocchi, S., Senn, V., Demmou, L., Müller, C., and Lüthi, A. (2008). Switching on and off fear by distinct neuronal circuits. Nature *454*, 600–606.

Holmes, A. (2019). Biological clues to an enigmatic treatment for traumatic stress. Nature *566*, 335–336.

Hopfield, J.J. (1982). Neural networks and physical systems with emergent collective computational abilities. Proc. Natl. Acad. Sci. U. S. A. *79*, 2554–2558.

Hsu, P.D., Lander, E.S., and Zhang, F. (2014). Development and Applications of CRISPR-Cas9 for Genome Engineering. Cell *157*, 1262–1278.

Ikegaya, Y., Aaron, G., Cossart, R., Aronov, D., Lampl, I., Ferster, D., and Yuste, R. (2004). Synfire chains and cortical songs: temporal modules of cortical activity. Science *304*, 559–564.

Inoue, M., Takeuchi, A., Horigane, S.-I., Ohkura, M., Gengyo-Ando, K., Fujii, H., Kamijo, S., Takemoto-Kimura, S., Kano, M., Nakai, J., et al. (2015). Rational design of a high-affinity, fast, red calcium indicator R-CaMP2. Nat. Methods *12*, 64–70.

Inoue, M., Takeuchi, A., Manita, S., Horigane, S.-I., Sakamoto, M., Kawakami, R., Yamaguchi, K., Otomo, K., Yokoyama, H., Kim, R., et al. (2019). Rational Engineering of XCaMPs, a Multicolor GECI Suite for In Vivo Imaging of Complex Brain Circuit Dynamics. Cell *177*, 1346-1360.e24.

Jacobsen, K.X., Höistad, M., Staines, W.A., and Fuxe, K. (2006). The distribution of dopamine D1 receptor and mu-opioid receptor 1 receptor immunoreactivities in the amygdala and interstitial nucleus of the posterior limb of the anterior commissure: relationships to tyrosine hydroxylase and opioid peptide terminal systems. Neuroscience *141*, 2007–2018.

Jun, J.J., Steinmetz, N.A., Siegle, J.H., Denman, D.J., Bauza, M., Barbarits, B., Lee, A.K., Anastassiou, C.A., Andrei, A., Aydın, Ç., et al. (2017). Fully integrated silicon probes for high-density recording of neural activity. Nature *551*, 232–236.

Jüngling, K., Seidenbecher, T., Sosulina, L., Lesting, J., Sangha, S., Clark, S.D., Okamura, N., Duangdao, D.M., Xu, Y.-L., Reinscheid, R.K., et al. (2008). Neuropeptide S-mediated control of fear expression and extinction: role of intercalated GABAergic neurons in the amygdala. Neuron *59*, 298–310.

Kandel, E.R. (2001). The molecular biology of memory storage: a dialogue between genes and synapses. Science *294*, 1030–1038.

Kaoru, T., Liu, F.-C., Ishida, M., Oishi, T., Hayashi, M., Kitagawa, M., Shimoda, K., and Takahashi, H. (2010). Molecular characterization of the intercalated cell masses of the amygdala: implications for the relationship with the striatum. Neuroscience *166*, 220–230.

Kellicutt, M.H., and Schwartzbaum, J.S. (1963). Formation of a Conditioned Emotional Response (CER) Following Lesions of the Amygdaloid Complex in Rats. Psychol. Rep. *12*, 351–358.

Kerlin, A.M., Andermann, M.L., Berezovskii, V.K., and Reid, R.C. (2010). Broadly tuned response properties of diverse inhibitory neuron subtypes in mouse visual cortex. Neuron *67*, 858–871.

Khan, A.G., Poort, J., Chadwick, A., Blot, A., Sahani, M., Mrsic-Flogel, T.D., and Hofer, S.B. (2018). Distinct learning-induced changes in stimulus selectivity and interactions of GABAergic interneuron classes in visual cortex. Nat. Neurosci. *21*, 851–859.

Kim, J.J., and Fanselow, M.S. (1992). Modality-specific retrograde amnesia of fear. Science *256*, 675–677.

Kim, J., Zhang, X., Muralidhar, S., LeBlanc, S.A., and Tonegawa, S. (2017). Basolateral to Central Amygdala Neural Circuits for Appetitive Behaviors. Neuron *93*, 1464-1479.e5.

Klein, R.L., Meyer, E.M., Peel, A.L., Zolotukhin, S., Meyers, C., Muzyczka, N., and King, M.A. (1998). Neuron-specific transduction in the rat septohippocampal or nigrostriatal pathway by recombinant adeno-associated virus vectors. Exp. Neurol. *150*, 183–194.

Klüver, H., and Bucy, P.C. (1937). "Psychic blindness" and other symptoms following bilateral temporal lobectomy in Rhesus monkeys. Am. J. Physiol. *119*, 352–353.

Kuerbitz, J., Arnett, M., Ehrman, S., Williams, M.T., Vorhees, C.V., Fisher, S.E., Garratt, A.N., Muglia, L.J., Waclaw, R.R., and Campbell, K. (2018). Loss of Intercalated Cells (ITCs) in the Mouse Amygdala of Tshz1 Mutants Correlates with Fear, Depression, and Social Interaction Phenotypes. J. Neurosci. *38*, 1160–1177.

Kuerbitz, J., Madhavan, M., Ehrman, L.A., Kohli, V., Waclaw, R.R., and Campbell, K. (2020). Temporally Distinct Roles for the Zinc Finger Transcription Factor Sp8 in the Generation and Migration of Dorsal Lateral Ganglionic Eminence (dLGE)-Derived Neuronal Subtypes in the Mouse. Cereb. Cortex *31*, 1744–1762.

Kuhlman, S.J., and Huang, Z.J. (2008). High-resolution labeling and functional manipulation of specific neuron types in mouse brain by Cre-activated viral gene expression. PLoS One *3*, e2005.

LeDoux, J.E. (1986). Sensory systems and emotion: A model of affective processing. Integr. Psychiatry *4*, 237–243.

LeDoux, J.E. (2000). Emotion circuits in the brain. Annu. Rev. Neurosci. *23*, 155–184.

LeDoux, J.E., Iwata, J., Cicchetti, P., and Reis, D.J. (1988). Different projections of the central amygdaloid nucleus mediate autonomic and behavioral correlates of conditioned fear. J. Neurosci. *8*, 2517–2529.

LeDoux, J.E., Cicchetti, P., Xagoraris, A., and Romanski, L.M. (1990). The lateral amygdaloid nucleus: sensory interface of the amygdala in fear conditioning. J. Neurosci. *10*, 1062–1069.

Li, H., Penzo, M.A., Taniguchi, H., Kopec, C.D., Huang, Z.J., and Li, B. (2013). Experience-dependent modification of a central amygdala fear circuit. Nat. Neurosci. *16*, 332–339.

Likhtik, E., Pelletier, J.G., Paz, R., and Paré, D. (2005). Prefrontal control of the amygdala. J. Neurosci. *25*, 7429–7437.

Likhtik, E., Popa, D., Apergis-Schoute, J., Fidacaro, G.A., and Paré, D. (2008). Amygdala intercalated neurons are required for expression of fear extinction. Nature *454*, 642–645.

Luo, L., Callaway, E.M., and Svoboda, K. (2008). Genetic dissection of neural circuits. Neuron *57*, 634–660.

Luo, L., Callaway, E.M., and Svoboda, K. (2018). Genetic Dissection of Neural Circuits: A Decade of Progress. Neuron *98*, 256–281.

Madisen, L., Zwingman, T.A., Sunkin, S.M., Oh, S.W., Zariwala, H.A., Gu, H., Ng, L.L., Palmiter, R.D., Hawrylycz, M.J., Jones, A.R., et al. (2010). A robust and high-throughput Cre reporting and characterization system for the whole mouse brain. Nat. Neurosci. *13*, 133–140.

Malinow, R., and Malenka, R.C. (2002). AMPA receptor trafficking and synaptic plasticity. Annu. Rev. Neurosci. *25*, 103–126.

Mańko, M., Geracitano, R., and Capogna, M. (2011). Functional connectivity of the main intercalated nucleus of the mouse amygdala. J. Physiol. *589*, 1911–1925.

Maren, S., and Holmes, A. (2016). Stress and Fear Extinction. Neuropsychopharmacology *41*, 58–79.

Maren, S., Aharonov, G., and Fanselow, M.S. (1996). Retrograde abolition of conditional fear after excitotoxic lesions in the basolateral amygdala of rats: absence of a temporal gradient. Behav. Neurosci. *110*, 718–726.

Marowsky, A., Yanagawa, Y., Obata, K., and Vogt, K.E. (2005). A specialized subclass of interneurons mediates dopaminergic facilitation of amygdala function. Neuron *48*, 1025–1037.

McDonald, A.J., Mascagni, F., and Zaric, V. (2012). Subpopulations of somatostatin-immunoreactive non-pyramidal neurons in the amygdala and adjacent external capsule project to the basal forebrain: evidence for the existence of GABAergic projection neurons in the cortical nuclei and basolateral nuclear complex. Front. Neural Circuits *6*, 46.

McKernan, M.G., and Shinnick-Gallagher, P. (1997). Fear conditioning induces a lasting potentiation of synaptic currents in vitro. Nature *390*, 607–611.

Milad, M.R., and Quirk, G.J. (2002). Neurons in medial prefrontal cortex signal memory for fear extinction. Nature *420*, 70–74.

Milad, M.R., and Quirk, G.J. (2012). Fear extinction as a model for translational neuroscience: ten years of progress. Annu. Rev. Psychol. *63*, 129–151.

Millhouse, O.E. (1986). The intercalated cells of the amygdala. J. Comp. Neurol. *247*, 246–271.

Miyawaki, A., Llopis, J., Heim, R., Michael McCaffery, J., Adams, J.A., Ikura, M., and Tsien, R.Y. (1997). Fluorescent indicators for Ca 2+ based on green fluorescent proteins and calmodulin. Nature *388*, 882–887.

Morris, R.G. (1999). D.O. Hebb: The Organization of Behavior, Wiley: New York; 1949. Brain Res. Bull. *50*, 437.

Myers, K.M., and Davis, M. (2007). Mechanisms of fear extinction. Mol. Psychiatry *12*, 120–150.

Nagai, T., Sawano, A., Park, E.S., and Miyawaki, A. (2001). Circularly permuted green fluorescent proteins engineered to sense Ca2+. Proc. Natl. Acad. Sci. U. S. A. *98*, 3197–3202.

Nakai, J., Ohkura, M., and Imoto, K. (2001). A high signal-to-noise Ca(2+) probe composed of a single green fluorescent protein. Nat. Biotechnol. *19*, 137–141.

Namburi, P., Beyeler, A., Yorozu, S., Calhoon, G.G., Halbert, S.A., Wichmann, R., Holden, S.S., Mertens, K.L., Anahtar, M., Felix-Ortiz, A.C., et al. (2015). A circuit mechanism for differentiating positive and negative associations. Nature *520*, 675–678.

Nectow, A.R., and Nestler, E.J. (2020). Viral tools for neuroscience. Nat. Rev. Neurosci. *21*, 669–681.

Nitecka, L., and Frotscher, M. (1989). Organization and synaptic interconnections of GABAergic and cholinergic elements in the rat amygdaloid nuclei: single- and double-immunolabeling studies. J. Comp. Neurol. *279*, 470–488.

Ogden, P.J., Kelsic, E.D., Sinai, S., and Church, G.M. (2019). Comprehensive AAV capsid fitness landscape reveals a viral gene and enables machine-guided design. Science *366*, 1139–1143.

Ohki, K., Chung, S., Ch'ng, Y.H., Kara, P., and Reid, R.C. (2005). Functional imaging with cellular resolution reveals precise micro-architecture in visual cortex. Nature *433*, 597–603.

Palomares-Castillo, E., Hernández-Pérez, O.R., Pérez-Carrera, D., Crespo-Ramírez, M., Fuxe, K., and Pérez de la Mora, M. (2012). The intercalated paracapsular islands as a module for integration of signals regulating anxiety in the amygdala. Brain Res. *1476*, 211–234.

Pape, H.-C. (2005). GABAergic neurons: gate masters of the amygdala, mastered by dopamine. Neuron *48*, 877–879.

Pape, H.-C., and Pare, D. (2010). Plastic synaptic networks of the amygdala for the acquisition, expression, and extinction of conditioned fear. Physiol. Rev. *90*, 419–463.

Paré, D., and Smith, Y. (1993). The intercalated cell masses project to the central and medial nuclei of the amygdala in cats. Neuroscience *57*, 1077–1090.

Paré, D., Quirk, G.J., and Ledoux, J.E. (2004). New vistas on amygdala networks in conditioned fear. J. Neurophysiol. *92*, 1–9.

Pavlov, P.I. (1927). Conditioned reflexes: An investigation of the physiological activity of the cerebral cortex. Ann Neurosci *17*, 136–141.

Penzo, M.A., Robert, V., and Li, B. (2014). Fear conditioning potentiates synaptic transmission onto long-range projection neurons in the lateral subdivision of central amygdala. J. Neurosci. *34*, 2432–2437.

Phillips, R.G., and LeDoux, J.E. (1992). Differential contribution of amygdala and hippocampus to cued and contextual fear conditioning. Behav. Neurosci. *106*, 274–285.

Pinard, C.R., Mascagni, F., and McDonald, A.J. (2012). Medial prefrontal cortical innervation of the intercalated nuclear region of the amygdala. Neuroscience *205*, 112–124.

Quirk, G.J., Repa, C., and LeDoux, J.E. (1995). Fear conditioning enhances short-latency auditory responses of lateral amygdala neurons: parallel recordings in the freely behaving rat. Neuron *15*, 1029–1039.

Quirk, G.J., Armony, J.L., and LeDoux, J.E. (1997). Fear conditioning enhances different temporal components of tone-evoked spike trains in auditory cortex and lateral amygdala. Neuron *19*, 613–624.

Renier, N., Wu, Z., Simon, D.J., Yang, J., Ariel, P., and Tessier-Lavigne, M. (2014). iDISCO: a simple, rapid method to immunolabel large tissue samples for volume imaging. Cell *159*, 896–910.

Rogan, M.T., Stäubli, U.V., and LeDoux, J.E. (1997). Fear conditioning induces associative long-term potentiation in the amygdala. Nature *390*, 604–607.

Roska, B., and Sahel, J.-A. (2018). Restoring vision. Nature *557*, 359–367.

Royer, S., and Paré, D. (2003). Conservation of total synaptic weight through balanced synaptic depression and potentiation. Nature *422*, 518–522.

Royer, S., Martina, M., and Paré, D. (1999). An inhibitory interface gates impulse traffic between the input and output stations of the amygdala. J. Neurosci. *19*, 10575–10583.

Royer, S., Martina, M., and Paré, D. (2000). Polarized synaptic interactions between intercalated neurons of the amygdala. J. Neurophysiol. *83*, 3509–3518.

Rumpel, S., LeDoux, J., Zador, A., and Malinow, R. (2005). Postsynaptic receptor trafficking underlying a form of associative learning. Science *308*, 83–88.

Sahel, J.-A., Boulanger-Scemama, E., Pagot, C., Arleo, A., Galluppi, F., Martel, J.N., Esposti, S.D., Delaux, A., de Saint Aubert, J.-B., de Montleau, C., et al. (2021). Partial recovery of visual function in a blind patient after optogenetic therapy. Nat. Med.

Samulski, R.J., Chang, L.S., and Shenk, T. (1989). Helper-free stocks of recombinant adeno-associated viruses: normal integration does not require viral gene expression. J. Virol. *63*, 3822–3828.

Sawinski, J., Wallace, D.J., Greenberg, D.S., Grossmann, S., Denk, W., and Kerr, J.N.D. (2009). Visually evoked activity in cortical cells imaged in freely moving animals. Proc. Natl. Acad. Sci. U. S. A. *106*, 19557–19562.

Senn, V., Wolff, S.B.E., Herry, C., Grenier, F., Ehrlich, I., Gründemann, J., Fadok, J.P., Müller, C., Letzkus, J.J., and Lüthi, A. (2014). Long-range connectivity defines behavioral specificity of amygdala neurons. Neuron *81*, 428–437.

Shalev, A., Liberzon, I., and Marmar, C. (2017). Post-Traumatic Stress Disorder. N. Engl. J. Med. *376*, 2459–2469.

Sierra-Mercado, D., Padilla-Coreano, N., and Quirk, G.J. (2011). Dissociable roles of prelimbic and infralimbic cortices, ventral hippocampus, and basolateral amygdala in the expression and extinction of conditioned fear. Neuropsychopharmacology *36*, 529–538.

Sofroniew, N.J., Flickinger, D., King, J., and Svoboda, K. (2016). A large field of view two-photon mesoscope with subcellular resolution for in vivo imaging. Elife *5*.

Sohal, V.S., Zhang, F., Yizhar, O., and Deisseroth, K. (2009). Parvalbumin neurons and gamma rhythms enhance cortical circuit performance. Nature *459*, 698–702.

Soriano, P. (1999). Generalized lacZ expression with the ROSA26 Cre reporter strain. Nat. Genet. *21*, 70–71.

Sotres-Bayon, F., Bush, D.E.A., and LeDoux, J.E. (2007). Acquisition of fear extinction requires activation of NR2B-containing NMDA receptors in the lateral amygdala. Neuropsychopharmacology *32*, 1929–1940.

Sotres-Bayon, F., Sierra-Mercado, D., Pardilla-Delgado, E., and Quirk, G.J. (2012). Gating of fear in prelimbic cortex by hippocampal and amygdala inputs. Neuron *76*, 804–812.

Steinmetz, N.A., Zatka-Haas, P., Carandini, M., and Harris, K.D. (2019). Distributed coding of choice, action and engagement across the mouse brain. Nature *576*, 266–273.

Steinmetz, N.A., Aydin, C., Lebedeva, A., Okun, M., Pachitariu, M., Bauza, M., Beau, M., Bhagat, J., Böhm, C., Broux, M., et al. (2021). Neuropixels 2.0: A miniaturized high-density probe for stable, long-term brain recordings. Science *372*.

Stosiek, C., Garaschuk, O., Holthoff, K., and Konnerth, A. (2003). In vivo two-photon calcium imaging of neuronal networks. Proc. Natl. Acad. Sci. U. S. A. *100*, 7319–7324.

Stringer, C., Michaelos, M., Tsyboulski, D., Lindo, S.E., and Pachitariu, M. (2021). High-precision coding in visual cortex. Cell *184*, 2767-2778.e15.

Strobel, C., Marek, R., Gooch, H.M., Sullivan, R.K.P., and Sah, P. (2015). Prefrontal and Auditory Input to Intercalated Neurons of the Amygdala. Cell Rep. *10*, 1435–1442.

Stuber, G.D., Sparta, D.R., Stamatakis, A.M., van Leeuwen, W.A., Hardjoprajitno, J.E., Cho, S., Tye, K.M., Kempadoo, K.A., Zhang, F., Deisseroth, K., et al. (2011). Excitatory transmission from the amygdala to nucleus accumbens facilitates reward seeking. Nature *475*, 377–380.

Susaki, E.A., and Ueda, H.R. (2016). Whole-body and Whole-Organ Clearing and Imaging Techniques with Single-Cell Resolution: Toward Organism-Level Systems Biology in Mammals. Cell Chem Biol *23*, 137–157.

Susaki, E.A., Tainaka, K., Perrin, D., Kishino, F., Tawara, T., Watanabe, T.M., Yokoyama, C., Onoe, H., Eguchi, M., Yamaguchi, S., et al. (2014). Whole-brain imaging with single-cell resolution using chemical cocktails and computational analysis. Cell *157*, 726–739.

Susaki, E.A., Shimizu, C., Kuno, A., Tainaka, K., Li, X., Nishi, K., Morishima, K., Ono, H., Ode, K.L., Saeki, Y., et al. (2020). Versatile whole-organ/body staining and imaging based on electrolyte-gel properties of biological tissues. Nat. Commun. *11*, 1982.

Svoboda, K., Denk, W., Kleinfeld, D., and Tank, D.W. (1997). In vivo dendritic calcium dynamics in neocortical pyramidal neurons. Nature *385*, 161–165.

Taniguchi, H., He, M., Wu, P., Kim, S., Paik, R., Sugino, K., Kvitsiani, D., Fu, Y., Lu, J., Lin, Y., et al. (2011). A resource of Cre driver lines for genetic targeting of GABAergic neurons in cerebral cortex. Neuron *71*, 995–1013.

Tian, L., Andrew Hires, S., Mao, T., Huber, D., Eugenia Chiappe, M., Chalasani, S.H., Petreanu, L., Akerboom, J., McKinney, S.A., Schreiter, E.R., et al. (2009). Imaging neural activity in worms, flies and mice with improved GCaMP calcium indicators. Nat. Methods *6*, 875–881.

Tillberg, P.W., Chen, F., Piatkevich, K.D., Zhao, Y., Yu, C.-C.J., English, B.P., Gao, L., Martorell, A., Suk, H.-J., Yoshida, F., et al. (2016). Protein-retention expansion microscopy

of cells and tissues labeled using standard fluorescent proteins and antibodies. Nat. Biotechnol. *34*, 987–992.

Tovote, P., Fadok, J.P., and Lüthi, A. (2015). Neuronal circuits for fear and anxiety. Nat. Rev. Neurosci. *16*, 317–331.

Tovote, P., Esposito, M.S., Botta, P., Chaudun, F., Fadok, J.P., Markovic, M., Wolff, S.B.E., Ramakrishnan, C., Fenno, L., Deisseroth, K., et al. (2016). Midbrain circuits for defensive behaviour. Nature *534*, 206–212.

Tsien, R.Y. (1980). New calcium indicators and buffers with high selectivity against magnesium and protons: design, synthesis, and properties of prototype structures. Biochemistry *19*, 2396–2404.

Tsien, J.Z., Chen, D.F., Gerber, D., Tom, C., Mercer, E.H., Anderson, D.J., Mayford, M., Kandel, E.R., and Tonegawa, S. (1996). Subregion- and Cell Type–Restricted Gene Knockout in Mouse Brain. Cell *87*, 1317–1326.

Tye, K.M., Mirzabekov, J.J., Warden, M.R., Ferenczi, E.A., Tsai, H.-C., Finkelstein, J., Kim, S.-Y., Adhikari, A., Thompson, K.R., Andalman, A.S., et al. (2013). Dopamine neurons modulate neural encoding and expression of depression-related behaviour. Nature *493*, 537–541.

Ugolini, G. (1995). Specificity of rabies virus as a transneuronal tracer of motor networks: transfer from hypoglossal motoneurons to connected second-order and higher order central nervous system cell groups. J. Comp. Neurol. *356*, 457–480.

Waclaw, R.R., Ehrman, L.A., Pierani, A., and Campbell, K. (2010). Developmental origin of the neuronal subtypes that comprise the amygdalar fear circuit in the mouse. J. Neurosci. *30*, 6944–6953.

Wardill, T.J., Chen, T.-W., Schreiter, E.R., Hasseman, J.P., Tsegaye, G., Fosque, B.F., Behnam, R., Shields, B.C., Ramirez, M., Kimmel, B.E., et al. (2013). A neuron-based screening platform for optimizing genetically-encoded calcium indicators. PLoS One *8*, e77728.

Whittle, N., Hauschild, M., Lubec, G., Holmes, A., and Singewald, N. (2010). Rescue of impaired fear extinction and normalization of cortico-amygdala circuit dysfunction in a genetic mouse model by dietary zinc restriction. J. Neurosci. *30*, 13586–13596.

Wickersham, I.R., Lyon, D.C., Barnard, R.J.O., Mori, T., Finke, S., Conzelmann, K.-K., Young, J.A.T., and Callaway, E.M. (2007a). Monosynaptic restriction of transsynaptic tracing from single, genetically targeted neurons. Neuron *53*, 639–647.

Wickersham, I.R., Finke, S., Conzelmann, K.-K., and Callaway, E.M. (2007b). Retrograde neuronal tracing with a deletion-mutant rabies virus. Nat. Methods *4*, 47–49.

Wilensky, A.E., Schafe, G.E., and LeDoux, J.E. (1999). Functional inactivation of the amygdala before but not after auditory fear conditioning prevents memory formation. J. Neurosci. *19*, RC48.

Wilensky, A.E., Schafe, G.E., Kristensen, M.P., and LeDoux, J.E. (2006). Rethinking the fear circuit: the central nucleus of the amygdala is required for the acquisition, consolidation, and expression of Pavlovian fear conditioning. J. Neurosci. *26*, 12387–12396.

Xu, C., Krabbe, S., Gründemann, J., Botta, P., Fadok, J.P., Osakada, F., Saur, D., Grewe, B.F., Schnitzer, M.J., Callaway, E.M., et al. (2016). Distinct Hippocampal Pathways Mediate Dissociable Roles of Context in Memory Retrieval. Cell *167*, 961-972.e16.

Xu, S., Yang, H., Menon, V., Lemire, A.L., Wang, L., Henry, F.E., Turaga, S.C., and Sternson, S.M. (2020). Behavioral state coding by molecularly defined paraventricular hypothalamic cell type ensembles. Science *370*.

Yuste, R., and Denk, W. (1995). Dendritic spines as basic functional units of neuronal integration. Nature *375*, 682–684.

Yuste, R., and Katz, L.C. (1991). Control of postsynaptic Ca2+ influx in developing neocortex by excitatory and inhibitory neurotransmitters. Neuron *6*, 333–344.

Zhang, F. (2019). Development of CRISPR-Cas systems for genome editing and beyond. Q. Rev. Biophys. *52*.

Zimmerman, J.M., and Maren, S. (2010). NMDA receptor antagonism in the basolateral but not central amygdala blocks the extinction of Pavlovian fear conditioning in rats. Eur. J. Neurosci. *31*, 1664–1670.

Ziv, Y., Burns, L.D., Cocker, E.D., Hamel, E.O., Ghosh, K.K., Kitch, L.J., El Gamal, A., and Schnitzer, M.J. (2013). Long-term dynamics of CA1 hippocampal place codes. Nat. Neurosci. *16*, 264–266.

Zong, W., Wu, R., Li, M., Hu, Y., Li, Y., Li, J., Rong, H., Wu, H., Xu, Y., Lu, Y., et al. (2017). Fast high-resolution miniature two-photon microscopy for brain imaging in freely behaving mice. Nat. Methods *14*, 713–719.

Zong, W., Wu, R., Chen, S., Wu, J., Wang, H., Zhao, Z., Chen, G., Tu, R., Wu, D., Hu, Y., et al. (2021). Miniature two-photon microscopy for enlarged field-of-view, multi-plane and long-term brain imaging. Nat. Methods *18*, 46–49.

For Project 1

1 Craske, M. G. *et al.* Anxiety disorders. *Nat Rev Dis Primers* **3**, 17024, doi:10.1038/nrdp.2017.24 (2017).

2 Shalev, A., Liberzon, I. & Marmar, C. Post-Traumatic Stress Disorder. *N Engl J Med* **376**, 2459-2469, doi:10.1056/NEJMra1612499 (2017).

3 Duvarci, S. & Pare, D. Amygdala microcircuits controlling learned fear. *Neuron* **82**, 966-980, doi:10.1016/j.neuron.2014.04.042 (2014).

4 Li, B. Central amygdala cells for learning and expressing aversive emotional memories. *Curr Opin Behav Sci* **26**, 40-45, doi:10.1016/j.cobeha.2018.09.012 (2019).

5 Marek, R., Sun, Y. & Sah, P. Neural circuits for a top-down control of fear and extinction. *Psychopharmacology (Berl)* **236**, 313-320, doi:10.1007/s00213-018-5033-2 (2019).

6 Milad, M. R. & Quirk, G. J. Fear extinction as a model for translational neuroscience: ten years of progress. *Annual review of psychology* **63**, 129-151, doi:10.1146/annurev.psych.121208.131631 (2012).

7 Orsini, C. A. & Maren, S. Neural and cellular mechanisms of fear and extinction memory formation. *Neurosci Biobehav Rev* **36**, 1773-1802, doi:10.1016/j.neubiorev.2011.12.014 (2012).

8 Tovote, P., Fadok, J. P. & Luthi, A. Neuronal circuits for fear and anxiety. *Nature reviews. Neuroscience* **16**, 317-331, doi:10.1038/nrn3945 (2015).

9 LeDoux, J. E. Emotion circuits in the brain. *Annual review of neuroscience* **23**, 155-184, doi:DOI 10.1146/annurev.neuro.23.1.155 (2000).

10 Pavlov, I. P. *Conditioned reflexes*. (Oxford University Press, 1927).

11 Bouton, M. E. Context, ambiguity, and unlearning: sources of relapse after behavioral extinction. *Biol Psychiatry* **52**, 976-986, doi:10.1016/s0006-3223(02)01546-9 (2002).

12 Clem, R. L. & Schiller, D. New Learning and Unlearning: Strangers or Accomplices in Threat Memory Attenuation? *Trends Neurosci* **39**, 340-351, doi:10.1016/j.tins.2016.03.003 (2016).

13 Herry, C. *et al.* Neuronal circuits of fear extinction. *Eur J Neurosci* **31**, 599-612, doi:10.1111/j.1460-9568.2010.07101.x (2010).

14 Sotres-Bayon, F., Cain, C. K. & LeDoux, J. E. Brain mechanisms of fear extinction: historical perspectives on the contribution of prefrontal cortex. *Biol Psychiatry* **60**, 329-336, doi:10.1016/j.biopsych.2005.10.012 (2006).

15 Busti, D. *et al.* Different fear states engage distinct networks within the intercalated cell clusters of the amygdala. *The Journal of neuroscience : the official journal of the Society for Neuroscience* **31**, 5131-5144, doi:10.1523/JNEUROSCI.6100-10.2011 (2011).

16 Collins, D. R. & Pare, D. Spontaneous and evoked activity of intercalated amygdala neurons. *Eur J Neurosci* **11**, 3441-3448, doi:10.1046/j.1460-9568.1999.00763.x (1999).

17 Millhouse, O. E. The intercalated cells of the amygdala. *J Comp Neurol* **247**, 246-271, doi:10.1002/cne.902470209 (1986).

18 Waclaw, R. R., Ehrman, L. A., Pierani, A. & Campbell, K. Developmental origin of the neuronal subtypes that comprise the amygdalar fear circuit in the mouse. *The Journal of neuroscience : the official journal of the Society for Neuroscience* **30**, 6944-6953, doi:10.1523/JNEUROSCI.5772-09.2010 (2010).

19 Royer, S., Martina, M. & Pare, D. An inhibitory interface gates impulse traffic between the input and output stations of the amygdala. *The Journal of neuroscience : the official journal of the Society for Neuroscience* **19**, 10575-10583 (1999).

20 Jungling, K. *et al.* Neuropeptide S-mediated control of fear expression and extinction: role of intercalated GABAergic neurons in the amygdala. *Neuron* **59**, 298-310, doi:10.1016/j.neuron.2008.07.002 (2008).

21 Amano, T., Unal, C. T. & Pare, D. Synaptic correlates of fear extinction in the amygdala. *Nat Neurosci* **13**, 489-494, doi:10.1038/nn.2499 (2010).

22 An, B. *et al.* Amount of fear extinction changes its underlying mechanisms. *Elife* **6**, doi:10.7554/eLife.25224 (2017).

23 Likhtik, E., Popa, D., Apergis-Schoute, J., Fidacaro, G. A. & Pare, D. Amygdala intercalated neurons are required for expression of fear extinction. *Nature* **454**, 642-645, doi:10.1038/nature07167 (2008).

24 Hefner, K. *et al.* Impaired fear extinction learning and cortico-amygdala circuit abnormalities in a common genetic mouse strain. *The Journal of neuroscience : the official journal of the Society for Neuroscience* **28**, 8074-8085, doi:10.1523/JNEUROSCI.4904-07.2008 (2008).

25 Adhikari, A. *et al.* Basomedial amygdala mediates top-down control of anxiety and fear. *Nature* **527**, 179-185, doi:10.1038/nature15698 (2015).

26 Asede, D., Bosch, D., Luthi, A., Ferraguti, F. & Ehrlich, I. Sensory inputs to intercalated cells provide fear-learning modulated inhibition to the basolateral amygdala. *Neuron* **86**, 541-554, doi:10.1016/j.neuron.2015.03.008 (2015).

27 Manko, M., Geracitano, R. & Capogna, M. Functional connectivity of the main intercalated nucleus of the mouse amygdala. *J Physiol* **589**, 1911-1925, doi:10.1113/jphysiol.2010.201475 (2011).

28 Grewe, B. F. *et al.* Neural ensemble dynamics underlying a long-term associative memory. *Nature* **543**, 670-675, doi:10.1038/nature21682 (2017).

29 Luo, R. *et al.* A dopaminergic switch for fear to safety transitions. *Nat Commun* **9**, 2483, doi:10.1038/s41467-018-04784-7 (2018).

30 Salinas-Hernandez, X. I. *et al.* Dopamine neurons drive fear extinction learning by signaling the omission of expected aversive outcomes. *Elife* **7**, doi:10.7554/eLife.38818 (2018).

31 Pare, D., Quirk, G. J. & Ledoux, J. E. New vistas on amygdala networks in conditioned fear. *J Neurophysiol* **92**, 1-9, doi:10.1152/jn.00153.2004 (2004).

32 Ehrlich, I. *et al.* Amygdala inhibitory circuits and the control of fear memory. *Neuron* **62**, 757-771, doi:10.1016/j.neuron.2009.05.026 (2009).

33 Bienvenu, T. C. *et al.* Large intercalated neurons of amygdala relay noxious sensory information. *The Journal of neuroscience : the official journal of the Society for Neuroscience* **35**, 2044-2057, doi:10.1523/JNEUROSCI.1323-14.2015 (2015).

34 Strobel, C., Marek, R., Gooch, H. M., Sullivan, R. K. P. & Sah, P. Prefrontal and Auditory Input to Intercalated Neurons of the Amygdala. *Cell Rep* **10**, 1435-1442, doi:10.1016/j.celrep.2015.02.008 (2015).

35 Herry, C. *et al.* Switching on and off fear by distinct neuronal circuits. *Nature* **454**, 600-606, doi:10.1038/nature07166 (2008).

36 Senn, V. *et al.* Long-range connectivity defines behavioral specificity of amygdala neurons. *Neuron* **81**, 428-437, doi:10.1016/j.neuron.2013.11.006 (2014).

37 Baek, J. *et al.* Neural circuits underlying a psychotherapeutic regimen for fear disorders. *Nature* **566**, 339-343, doi:10.1038/s41586-019-0931-y (2019).

38 Pare, D. & Smith, Y. The intercalated cell masses project to the central and medial nuclei of the amygdala in cats. *Neuroscience* **57**, 1077-1090, doi:10.1016/0306-4522(93)90050-p (1993).

39 Tovote, P. *et al.* Midbrain circuits for defensive behaviour. *Nature* **534**, 206-212, doi:10.1038/nature17996 (2016).

40 McGarry, L. M. & Carter, A. G. Inhibitory Gating of Basolateral Amygdala Inputs to the Prefrontal Cortex. *J Neurosci* **36**, 9391-9406, doi:10.1523/JNEUROSCI.0874-16.2016 (2016).

41 Arruda-Carvalho, M. & Clem, R. L. Prefrontal-amygdala fear networks come into focus. *Front Syst Neurosci* **9**, 145, doi:10.3389/fnsys.2015.00145 (2015).

42 Herry, C. & Johansen, J. P. Encoding of fear learning and memory in distributed neuronal circuits. *Nature neuroscience* **17**, 1644-1654, doi:10.1038/nn.3869 (2014).

43 Ungless, M. A., Magill, P. J. & Bolam, J. P. Uniform inhibition of dopamine neurons in the ventral tegmental area by aversive stimuli. *Science* **303**, 2040-2042, doi:10.1126/science.1093360 (2004).

44 Kim, J. *et al.* Rapid, biphasic CRF neuronal responses encode positive and negative valence. *Nat Neurosci* **22**, 576-585, doi:10.1038/s41593-019-0342-2 (2019).

45 Machens, C. K., Romo, R. & Brody, C. D. Flexible control of mutual inhibition: a neural model of two-interval discrimination. *Science* **307**, 1121-1124, doi:10.1126/science.1104171 (2005).

46 Koyama, M. & Pujala, A. Mutual inhibition of lateral inhibition: a network motif for an elementary computation in the brain. *Curr Opin Neurobiol* **49**, 69-74, doi:10.1016/j.conb.2017.12.019 (2018).

47 Grundemann, J. *et al.* Amygdala ensembles encode behavioral states. *Science* **364**, doi:10.1126/science.aav8736 (2019).

48 Felsenberg, J. *et al.* Integration of Parallel Opposing Memories Underlies Memory Extinction. *Cell* **175**, 709-722 e715, doi:10.1016/j.cell.2018.08.021 (2018).

49 Solomon, R. L. & Corbit, J. D. Opponent-Process Theory of Motivation .1. Temporal Dynamics of Affect. *Psychological Review* **81**, 119-145, doi:DOI 10.1037/h0036128 (1974).

50 Zhang, X., Kim, J. & Tonegawa, S. Amygdala Reward Neurons Form and Store Fear Extinction Memory. *Neuron* **105**, 1077-1093 e1077, doi:10.1016/j.neuron.2019.12.025 (2020).

51 Pare, D. & Smith, Y. GABAergic projection from the intercalated cell masses of the amygdala to the basal forebrain in cats. *J Comp Neurol* **344**, 33-49, doi:10.1002/cne.903440104 (1994).

52 Braak, H. & Braak, E. Neuronal types in the basolateral amygdaloid nuclei of man. *Brain Res Bull* **11**, 349-365, doi:10.1016/0361-9230(83)90171-5 (1983).

53 Stefanits, H. *et al.* GABAA receptor subunits in the human amygdala and hippocampus: Immunohistochemical distribution of 7 subunits. *J Comp Neurol* **526**, 324-348, doi:10.1002/cne.24337 (2018).

54 Rousso, D. L. *et al.* Two Pairs of ON and OFF Retinal Ganglion Cells Are Defined by Intersectional Patterns of Transcription Factor Expression. *Cell Rep* **15**, 1930-1944, doi:10.1016/j.celrep.2016.04.069 (2016).

55 Guenthner, C. J., Miyamichi, K., Yang, H. H., Heller, H. C. & Luo, L. Permanent genetic access to transiently active neurons via TRAP: targeted recombination in active populations. *Neuron* **78**, 773-784, doi:10.1016/j.neuron.2013.03.025 (2013).

56 Chen, T. W. *et al.* Ultrasensitive fluorescent proteins for imaging neuronal activity. *Nature* **499**, 295-300, doi:10.1038/nature12354 (2013).

57 Vardy, E. *et al.* A New DREADD Facilitates the Multiplexed Chemogenetic Interrogation of Behavior. *Neuron* **86**, 936-946, doi:10.1016/j.neuron.2015.03.065 (2015).

58 Armbruster, B. N., Li, X., Pausch, M. H., Herlitze, S. & Roth, B. L. Evolving the lock to fit the key to create a family of G protein-coupled receptors potently activated by an inert ligand. *Proceedings of the National Academy of Sciences of the United States of America* **104**, 5163-5168, doi:10.1073/pnas.0700293104 (2007).

59 Shemesh, O. A. *et al.* Temporally precise single-cell-resolution optogenetics. *Nature neuroscience* **20**, 1796-1806, doi:10.1038/s41593-017-0018-8 (2017).

60 Dana, H. *et al.* Sensitive red protein calcium indicators for imaging neural activity. *Elife* **5**, doi:10.7554/eLife.12727 (2016).

61 Dana, H. *et al.* High-performance calcium sensors for imaging activity in neuronal populations and microcompartments. *Nature methods* **16**, 649-657, doi:10.1038/s41592-019-0435-6 (2019).

62 Renier, N. *et al.* iDISCO: a simple, rapid method to immunolabel large tissue samples for volume imaging. *Cell* **159**, 896-910, doi:10.1016/j.cell.2014.10.010 (2014).

63 Susaki, E. A. *et al.* Whole-brain imaging with single-cell resolution using chemical cocktails and computational analysis. *Cell* **157**, 726-739, doi:10.1016/j.cell.2014.03.042 (2014).

64 Federico Claudi, A. L. T., Tiago Branco. Brainrender. A python based software for visualisation of neuroanatomical and morphological data. *bioRxiv*, doi:doi:10.1101/2020.02.23.961748 (2020).

65 Ghosh, K. K. *et al.* Miniaturized integration of a fluorescence microscope. *Nature methods* **8**, 871-878, doi:10.1038/nmeth.1694 (2011).

66 Franklin, K. B. J. & Paxinos, G. *The mouse brain in stereotaxic coordinates*. (Academic Press, 1997).

67 Bukalo, O. *et al.* Prefrontal inputs to the amygdala instruct fear extinction memory formation. *Sci Adv* **1**, doi:10.1126/sciadv.1500251 (2015).

68 Petreanu, L., Huber, D., Sobczyk, A. & Svoboda, K. Channelrhodopsin-2-assisted circuit mapping of long-range callosal projections. *Nature neuroscience* **10**, 663-668, doi:10.1038/nn1891 (2007).

69 Tanaka, Y., Tanaka, Y., Furuta, T., Yanagawa, Y. & Kaneko, T. The effects of cutting solutions on the viability of GABAergic interneurons in cerebral cortical slices of adult mice. *J Neurosci Methods* **171**, 118-125, doi:10.1016/j.jneumeth.2008.02.021 (2008).

70 Ting, J. T., Daigle, T. L., Chen, Q. & Feng, G. Acute brain slice methods for adult and aging animals: application of targeted patch clamp analysis and optogenetics. *Methods Mol Biol* **1183**, 221-242, doi:10.1007/978-1-4939-1096-0_14 (2014).

71 Lerner, T. N. *et al.* Intact-Brain Analyses Reveal Distinct Information Carried by SNc Dopamine Subcircuits. *Cell* **162**, 635-647, doi:10.1016/j.cell.2015.07.014 (2015).

72 Gunaydin, L. A. *et al.* Natural neural projection dynamics underlying social behavior. *Cell* **157**, 1535-1551, doi:10.1016/j.cell.2014.05.017 (2014).

73 Lopes, G. *et al.* Bonsai: an event-based framework for processing and controlling data streams. *Front Neuroinform* **9**, 7, doi:10.3389/fninf.2015.00007 (2015).

74 Pnevmatikakis, E. A. & Giovannucci, A. NoRMCorre: An online algorithm for piecewise rigid motion correction of calcium imaging data. *J Neurosci Methods* **291**, 83-94, doi:10.1016/j.jneumeth.2017.07.031 (2017).

75 Hagihara, K. M., Murakami, T., Yoshida, T., Tagawa, Y. & Ohki, K. Neuronal activity is not required for the initial formation and maturation of visual selectivity. *Nature neuroscience* **18**, 1780-1788, doi:10.1038/nn.4155 (2015).

76 Kerlin, A. M., Andermann, M. L., Berezovskii, V. K. & Reid, R. C. Broadly tuned response properties of diverse inhibitory neuron subtypes in mouse visual cortex. *Neuron* **67**, 858-871, doi:10.1016/j.neuron.2010.08.002 (2010).

For Project 2

Chen, T.-W., Wardill, T.J., Sun, Y., Pulver, S.R., Renninger, S.L., Baohan, A., Schreiter, E.R., Kerr, R.A., Orger, M.B., Jayaraman, V., et al. (2013). Ultrasensitive fluorescent proteins for imaging neuronal activity. Nature *499*, 295–300.

Fadok, J.P., Krabbe, S., Markovic, M., Courtin, J., Xu, C., Massi, L., Botta, P., Bylund, K., Müller, C., Kovacevic, A., et al. (2017). A competitive inhibitory circuit for selection of active and passive fear responses. Nature *542*, 96–100.

Fanselow, M.S. (1991). The Midbrain Periaqueductal Gray as a Coordinator of Action in Response to Fear and Anxiety. In The Midbrain Periaqueductal Gray Matter: Functional,

Anatomical, and Neurochemical Organization, A. Depaulis, and R. Bandler, eds. (Boston, MA: Springer US), pp. 151–173.

Grewe, B.F., Gründemann, J., Kitch, L.J., Lecoq, J.A., Parker, J.G., Marshall, J.D., Larkin, M.C., Jercog, P.E., Grenier, F., Li, J.Z., et al. (2017). Neural ensemble dynamics underlying a long-term associative memory. Nature *543*, 670–675.

Guizar-Sicairos, M., Thurman, S.T., and Fienup, J.R. (2008). Efficient subpixel image registration algorithms. Opt. Lett., OL *33*, 156–158.

Hagihara, K.M., Bukalo, O., Zeller, M., Aksoy-Aksel, A., Karalis, N., Limoges, A., Rigg, T., Campbell, T., Mendez, A., Weinholtz, C., et al. (2021). Intercalated amygdala clusters orchestrate a switch in fear state. Nature.

Haubensak, W., Kunwar, P.S., Cai, H., Ciocchi, S., Wall, N.R., Ponnusamy, R., Biag, J., Dong, H.-W., Deisseroth, K., Callaway, E.M., et al. (2010). Genetic dissection of an amygdala microcircuit that gates conditioned fear. Nature *468*, 270–276.

Hunt, S., Sun, Y., Kucukdereli, H., Klein, R., and Sah, P. (2017). Intrinsic Circuits in the Lateral Central Amygdala. ENeuro *4*.

Jimenez, S.A., and Maren, S. (2009). Nuclear disconnection within the amygdala reveals a direct pathway to fear. Learn. Mem. *16*, 766–768.

Kim, J., Pignatelli, M., Xu, S., Itohara, S., and Tonegawa, S. (2016). Antagonistic negative and positive neurons of the basolateral amygdala. Nat. Neurosci. *19*, 1636–1646.

Kim, J., Zhang, X., Muralidhar, S., LeBlanc, S.A., and Tonegawa, S. (2017). Basolateral to Central Amygdala Neural Circuits for Appetitive Behaviors. Neuron *93*, 1464-1479.e5.

Krabbe, S., Paradiso, E., d'Aquin, S., Bitterman, Y., Courtin, J., Xu, C., Yonehara, K., Markovic, M., Müller, C., Eichlisberger, T., et al. (2019). Adaptive disinhibitory gating by VIP interneurons permits associative learning. Nat. Neurosci. *22*, 1834–1843.

LeDoux, J.E., Iwata, J., Cicchetti, P., and Reis, D.J. (1988). Different projections of the central amygdaloid nucleus mediate autonomic and behavioral correlates of conditioned fear. J. Neurosci. *8*, 2517–2529.

Li, B. (2019). Central amygdala cells for learning and expressing aversive emotional memories. Curr Opin Behav Sci *26*, 40–45.

Li, H., Penzo, M.A., Taniguchi, H., Kopec, C.D., Huang, Z.J., and Li, B. (2013). Experience-dependent modification of a central amygdala fear circuit. Nat. Neurosci. *16*, 332–339.

Lopes, G., Bonacchi, N., Frazão, J., Neto, J.P., Atallah, B.V., Soares, S., Moreira, L., Matias, S., Itskov, P.M., Correia, P.A., et al. (2015). Bonsai: an event-based framework for processing and controlling data streams. Front. Neuroinform. *9*, 7.

Nagase, M., Mikami, K., and Watabe, A.M. (2019). Parabrachial-to-amygdala control of aversive learning. Current Opinion in Behavioral Sciences *26*, 18–24.

Namburi, P., Beyeler, A., Yorozu, S., Calhoon, G.G., Halbert, S.A., Wichmann, R., Holden, S.S., Mertens, K.L., Anahtar, M., Felix-Ortiz, A.C., et al. (2015). A circuit mechanism for differentiating positive and negative associations. Nature *520*, 675–678.

Osakada, F., and Callaway, E.M. (2013). Design and generation of recombinant rabies virus vectors. Nat. Protoc. *8*, 1583–1601.

Osakada, F., Mori, T., Cetin, A.H., Marshel, J.H., Virgen, B., and Callaway, E.M. (2011). New rabies virus variants for monitoring and manipulating activity and gene expression in defined neural circuits. Neuron *71*, 617–631.

Palmiter, R.D. (2018). The Parabrachial Nucleus: CGRP Neurons Function as a General Alarm. Trends Neurosci. *41*, 280–293.

Paxinos, G., and Franklin, K.B.J. (2001). The Mouse Brain in Stereotaxic Coordinates (Academic).

Pecho-Vrieseling, E., Sigrist, M., Yoshida, Y., and Jessell, T.M. (2009). Specificity of sensory–motor connections encoded by Sema3e–Plxnd1 recognition. Nature.

Penzo, M.A., Robert, V., and Li, B. (2014). Fear conditioning potentiates synaptic transmission onto long-range projection neurons in the lateral subdivision of central amygdala. J. Neurosci. *34*, 2432–2437.

Pitkänen, A., Savander, V., and LeDoux, J.E. (1997). Organization of intra-amygdaloid circuitries in the rat: an emerging framework for understanding functions of the amygdala. Trends Neurosci. *20*, 517–523.

Schwarz, L.A., Miyamichi, K., Gao, X.J., Beier, K.T., Weissbourd, B., DeLoach, K.E., Ren, J., Ibanes, S., Malenka, R.C., Kremer, E.J., et al. (2015). Viral-genetic tracing of the input-output organization of a central noradrenaline circuit. Nature *524*, 88–92.

Soudais, C., Laplace-Builhe, C., Kissa, K., and Kremer, E.J. (2001). Preferential transduction of neurons by canine adenovirus vectors and their efficient retrograde transport in vivo. FASEB J. *15*, 2283–2285.

Tallone, T., Malin, S., Samuelsson, A., Wilbertz, J., Miyahara, M., Okamoto, K., Poellinger, L., Philipson, L., and Pettersson, S. (2001). A mouse model for adenovirus gene delivery. Proc. Natl. Acad. Sci. U. S. A. *98*, 7910–7915.

Taniguchi, H., He, M., Wu, P., Kim, S., Paik, R., Sugino, K., Kvitsiani, D., Fu, Y., Lu, J., Lin, Y., et al. (2011). A resource of Cre driver lines for genetic targeting of GABAergic neurons in cerebral cortex. Neuron *71*, 995–1013.

Tovote, P., Fadok, J.P., and Lüthi, A. (2015). Neuronal circuits for fear and anxiety. Nat. Rev. Neurosci. *16*, 317–331.

Tovote, P., Esposito, M.S., Botta, P., Chaudun, F., Fadok, J.P., Markovic, M., Wolff, S.B.E., Ramakrishnan, C., Fenno, L., Deisseroth, K., et al. (2016). Midbrain circuits for defensive behaviour. Nature *534*, 206–212.

Tye, K.M., Prakash, R., Kim, S.-Y., Fenno, L.E., Grosenick, L., Zarabi, H., Thompson, K.R., Gradinaru, V., Ramakrishnan, C., and Deisseroth, K. (2011). Amygdala circuitry mediating reversible and bidirectional control of anxiety. Nature *471*, 358–362.

Wertz, A., Trenholm, S., Yonehara, K., Hillier, D., Raics, Z., Leinweber, M., Szalay, G., Ghanem, A., Keller, G., Rózsa, B., et al. (2015). PRESYNAPTIC NETWORKS. Single-cell-

initiated monosynaptic tracing reveals layer-specific cortical network modules. Science *349*, 70–74.

Wickersham, I.R., Lyon, D.C., Barnard, R.J.O., Mori, T., Finke, S., Conzelmann, K.-K., Young, J.A.T., and Callaway, E.M. (2007). Monosynaptic restriction of transsynaptic tracing from single, genetically targeted neurons. Neuron *53*, 639–647.

Xu, C., Krabbe, S., Gründemann, J., Botta, P., Fadok, J.P., Osakada, F., Saur, D., Grewe, B.F., Schnitzer, M.J., Callaway, E.M., et al. (2016). Distinct Hippocampal Pathways Mediate Dissociable Roles of Context in Memory Retrieval. Cell *167*, 961-972.e16.

Zhou, P., Resendez, S.L., Rodriguez-Romaguera, J., Jimenez, J.C., Neufeld, S.Q., Giovannucci, A., Friedrich, J., Pnevmatikakis, E.A., Stuber, G.D., Hen, R., et al. (2018). Efficient and accurate extraction of in vivo calcium signals from microendoscopic video data. Elife *7*, e28728.